



## 저작자표시-비영리-변경금지 2.0 대한민국

이용자는 아래의 조건을 따르는 경우에 한하여 자유롭게

- 이 저작물을 복제, 배포, 전송, 전시, 공연 및 방송할 수 있습니다.

다음과 같은 조건을 따라야 합니다:



저작자표시. 귀하는 원저작자를 표시하여야 합니다.



비영리. 귀하는 이 저작물을 영리 목적으로 이용할 수 없습니다.



변경금지. 귀하는 이 저작물을 개작, 변형 또는 가공할 수 없습니다.

- 귀하는, 이 저작물의 재이용이나 배포의 경우, 이 저작물에 적용된 이용허락조건을 명확하게 나타내어야 합니다.
- 저작권자로부터 별도의 허가를 받으면 이러한 조건들은 적용되지 않습니다.

저작권법에 따른 이용자의 권리는 위의 내용에 의하여 영향을 받지 않습니다.

이것은 [이용허락규약\(Legal Code\)](#)을 이해하기 쉽게 요약한 것입니다.

[Disclaimer](#)

Ph. D. DISSERTATION

# IMPROVEMENT OF EFFICIENCY AND PHOTO-STABILITY IN INVERTED ORGANIC SOLAR CELLS

역구조 유기태양전지의 효율 및 광안정성 향상 연구

BY

JIYUN SONG

FEBRUARY 2017

DEPARTMENT OF  
ELECTRICAL AND COMPUTER ENGINEERING  
COLLEGE OF ENGINEERING  
SEOUL NATIONAL UNIVERSITY



# IMPROVEMENT OF EFFICIENCY AND PHOTO-STABILITY IN INVERTED ORGANIC SOLAR CELLS

역구조 유기태양전지의 효율 및 광안정성 향상 연구

지도교수 이 창 희

이 논문을 공학박사 학위논문으로 제출함

2017 년 2 월

서울대학교 대학원

전기·컴퓨터 공학부

송 지 연

송지연의 공학박사 학위논문을 인준함

2017 년 2 월

위 원 장 : \_\_\_\_\_ (인)

부위원장 : \_\_\_\_\_ (인)

위 원 : \_\_\_\_\_ (인)

위 원 : \_\_\_\_\_ (인)

위 원 : \_\_\_\_\_ (인)



# **Abstract**

## **IMPROVEMENT OF EFFICIENCY AND PHOTO-STABILITY IN INVERTED ORGANIC SOLAR CELLS**

**JIYUN SONG**

**DEPARTMENT OF  
ELECTRICAL AND COMPUTER ENGINEERING  
COLLEGE OF ENGINEERING  
SEOUL NATIONAL UNIVERSITY**

Organic solar cells are one of the most promising candidates for third generation solar cells, due to their potential of simple and low cost process to be commercialized in flexible, light-weight, and semi-transparent devices. With these advantages, organic solar cells can target new and niche applications, such as portable solar battery chargers, clothing, car windows, and so on, which are differentiated from inorganic counterparts.

There are prerequisite conditions for organic solar cells to be commercialized, which are high performance, low cost, and high stability. Low cost is known as one

of the main advantages in organic solar cells both in terms of material itself and fabrication methods, on the other hand, performance and stability issues are still remained to be considered for commercial viability.

In this thesis, two topics including the efficiency improvement and understanding of degradation mechanism are discussed. In terms of device configuration in organic solar cells used herein, an inverted structure, the electrons are collected by the bottom electrode – indium tin oxide (ITO), and holes are collected by the top electrode, is employed for better long-term device stability and manufacturing compatibility.

For efficiency improvement, along with the development of organic materials, optical engineering, and new processing techniques, the improvement of charge extraction properties has become a key topic for high performance organic solar cells. In order to enhance charge extraction characteristics, interlayer (or buffer layer) between electrode and light-absorbing layer is the most important to extract generated electrons and holes as efficiently as possible toward the electrodes. Here, a unique nanostructured electron-selective interlayer comprising of In-doped ZnO (ZnO:In) and vertically-aligned CdSe tetrapods (TPs) was introduced. With dimension-controlled CdSe TPs, the direct inorganic electron transport pathway is provided, resulting in the improvement of the short circuit current and fill factor of devices. This enhancement is attributed to the roles of CdSe TPs that reduce the recombination losses between the active layer and buffer layer, improve the hole-blocking as well as electron-transporting properties, and simultaneously improve charge collection characteristics. As a result, the power conversion efficiency of PTB7:PC<sub>71</sub>BM based solar cell with nanostructured CdSe TPs increases to 7.55%. Moreover, this approach introduced herein, which uses the length-controlled

inorganic nanocrystals as an interlayer, is expected to be a versatile platform for improving charge extraction in thin film solar cells.

Besides, systematic study for understanding the degradation mechanisms of organic solar cells was performed. Among the main factors known to degrade organic devices, which are oxygen, moisture, heat, and light, light is chosen since the sunlight can accelerate other degradation processes, and operating condition of solar cells is under the illumination with high photon flux system as well. Several light-induced mechanisms have been proposed with the well-known P3HT-based solar cells; however, considering the aging mechanisms also greatly depend on the organic materials of active layer, it is required to explore the mechanisms for high performance polymer-based solar devices. Therefore, in this thesis, the light-induced degradation of high performance PTB7-based organic solar cells in the first 24 hours was demonstrated. After the photo-induced aging, the device revealed 30 % of initial performance drop mostly through a decrease in  $J_{SC}$  and FF. In order to figure out the origin of this photo-induced degradation, the morphological and electrical characteristics of active layer and devices were investigated by atomic force microscopy, impedance spectroscopy, and temperature dependent current density-voltage characteristics. As a result, the light-induced traps inside the bulkheterojunction and two adjacent interfaces were found to be a primary cause of loss. Furthermore, this trap formation was observed with energy of 78 meV and with substantially high density of  $(8.3 \pm 2.0) \times 10^{17} \text{ cm}^{-3}$ , leading to highly trap-charge-limited conduction properties and electrical degradation of solar cells.

This thesis demonstrates the practical approaches to enhance power conversion efficiency and to understand light-induced degradation mechanism of inverted organic solar cells. These approaches and various measurement techniques including optical and electrical characterization methods introduced here are expected to be



applied not only to solar cells but also to other kinds of organic optoelectronic devices, such as OLEDs and organic thin-film transistors.

**Keywords:** Organic Solar Cells, Inverted Structure, Electron Extraction Layer, Tetrapod Nanocrystals, Photo-stability, Light-induced Degradation

**Student Number:** 2013-30243

# Contents

<b>Abstract</b>	<b>i</b>
<b>Contents</b>	<b>v</b>
<b>List of Figures</b>	<b>ix</b>
<b>List of Tables</b>	<b>xvi</b>
<b>Chapter 1 Introduction</b>	<b>1</b>
<b>1.1 Organic Solar Cells .....</b>	<b>3</b>
<b>1.2 Current State of the Art and Challenges in Organic Solar Cells .....</b>	<b>6</b>
<b>1.2.1 Progress in Efficiency Improvement of Organic Solar Cells .....</b>	<b>8</b>
<b>1.2.2 Stability/Degradation of Organic Solar Cells .....</b>	<b>11</b>
<b>1.3 Outline of Thesis.....</b>	<b>15</b>

## **Chapter 2    Theory and Experimental Methods            16**

### **2.1    Basic Device Physics of Organic Solar Cells ..... 16**

#### **2.1.1 Working Principle of Organic Solar Cells .....16**

#### **2.1.2 Solar Cell Performance Parameters .....17**

#### **2.1.3 Equivalent Circuit Model .....20**

### **2.2    Materials ..... 22**

#### **2.2.1 Materials .....22**

#### **2.2.2 Preparation of ZnO Nanoparticles .....23**

#### **2.2.3 Synthesis    of    CdSe    Tetrapods    and    Their    Surface Modification .....23**

### **2.3    Device Fabrication Methods ..... 25**

### **2.4    Thin Film Characterization Methods ..... 27**

#### **2.4.1 Optical Measurements .....27**

#### **2.4.2 Atomic Force Microscopy Technique.....29**

#### **2.4.3 Other Thin Film Characterization Methods .....30**

### **2.5    Device Characterization Methods ..... 31**

#### **2.5.1 Current Density–Voltage Characteristics Measurement31**

#### **2.5.2 Incident    Photon-to-electron    Conversion    Efficiency Measurement .....31**

2.5.3 Light Intensity Dependence Characteristics .....	32
2.5.4 Impedance Spectroscopy .....	35
2.5.5 Transient Photocurrent Measurement.....	37
2.5.6 Space Charge Limited Current Measurement .....	37
2.5.7 Light-induced Aging Conditions.....	38
<b>Chapter 3 Efficiency Improvement of Inverted Organic Solar Cells by Using CdSe Tetrapod as an Electron-selective Interlayer</b>	<b>40</b>
3.1 Introduction .....	40
3.2 Device Configuration of PTB7:PC <sub>71</sub> BM Solar Cells with CdSe Tetrapods .....	42
3.2.1 Tailored CdSe Tetrapods for Organic Solar Cells.....	44
3.2.2 Energy Level of CdSe Tetrapods – UPS Analysis .....	48
3.3 Performance of PTB7:PC <sub>71</sub> BM Solar Cells with CdSe Tetrapods .....	51
3.3.1 Solar Cell Device Characteristics.....	51
3.3.2 Recombination and Charge Collection Characteristics .	60
3.4 Summary .....	66

<b>Chapter 4</b>	<b>Understanding of Light-induced Degradation Mechanisms of Inverted Organic Solar Cells</b>	<b>67</b>
4.1	Introduction .....	67
4.2	Degradation Trend of Inverted PTB7:PC <sub>71</sub> BM Solar Cells .....	69
4.2.1	Degradation in Optical Properties .....	72
4.2.2	Degradation in Electrical Properties .....	77
4.3	Investigation into the Light-induced Degradation Mechanisms .....	79
4.3.1	Light Intensity Dependent <i>J-V</i> Characteristics .....	79
4.3.2	Impedance Analysis .....	83
4.3.3	Charge Carrier Conduction Properties .....	89
4.4	Summary .....	94
<b>Chapter 5</b>	<b>Conclusion</b>	<b>95</b>
	<b>Bibliography</b>	<b>98</b>
	<b>Publication</b>	<b>110</b>
	<b>Abstract in Korean (한글 초록)</b>	<b>115</b>

# List of Figures

Figure 1.1 Average annual growth rates of renewable energy capacity and biofuels production from the end of 2010 to the end of 2015. (Source : Renewables global status report 2016) .....	2
Figure 1.2 Solar photovoltaic global capacity, by country and region, 2005–2015. (Source : Renewables global status report 2016) .....	2
Figure 1.3 Relationship between power conversion efficiency, module areal costs, and cost per peak watt (in \$/Wp).[1] © 2014 Nature Publishing Group. For next-generation (or third generation) technologies the goal is to reach 0.3-0.5 \$/Wp, denoted by the blue shaded region.....	4
Figure 1.4 Best research solar cell efficiencies chart. Enlarged graph shows the reported timeline of efficiencies for organic solar cells (Source : National Renewable Energy Laboratory, Aug. 2016) .....	5
Figure 1.5 Requirements for commercialization of organic solar cells.....	7
Figure 1.6 Transmission electron microscopy (TEM) images and schematic illustration of CdSe TPs with controlled arm lengths ( <i>l</i> ). All scale bars are 50 nm. ....	10
Figure 2.1 The working principle of organic solar cells. ....	17

Figure 2.2 Current density-voltage ( $J$ - $V$ ) curve of solar cell.....	18
Figure 2.3 AM 1.5G spectral distribution of solar irradiation.....	19
Figure 2.4 The equivalent circuit diagram of solar cell under illumination. ....	21
Figure 2.5. (a and b) Chemical structures and (c) an energy level diagram of PTB7 and PC <sub>71</sub> BM, which are used as photoactive materials in this thesis. ....	23
Figure 2.6 Schematic of fabrication process and the structure of PTB7:PC <sub>71</sub> BM organic solar cells with electron-selective interlayer comprising of In- doped ZnO (ZnO:In) and vertically-aligned CdSe tetrapods (TPs).....	26
Figure 2.7 Schematic of an UV-Vis spectrophotometer. ....	27
Figure 2.8 (a) Schematic diagram of XPS. (b) XPS machine in Research Institute of Advanced Materials (RIAM) at Seoul National University. ....	28
Figure 2.9 Schematic of a conductive AFM measurement. ....	29
Figure 2.10 Schematic diagram of IPCE measurement.....	32
Figure 2.11 The equivalent circuit diagram of solar cell with additional recombination loss term ( $J_{\text{rec}}$ ). ....	33
Figure 2.12 Schematic diagram of the theoretical behavior of incident light intensity dependent $J$ - $V$ characteristics for (a) crystalline materials-based solar cells and (b) solar cells with disordered materials. Figure modified from [68]. ....	34
Figure 2.13 (a) Nyquist plot and (b) equivalent circuit of organic solar cells. The open circles in (a) are experimental data and the dotted line is the fitted line of impedance spectrum using an equivalent circuit of (b). ....	36
Figure 2.14 Schematic diagram of transient photoconductivity measurement. Nd:YAG pulsed laser (pulse duration $\sim 5$ ns, $\lambda = 590$ nm) was used as an excitation source, and load resistance $R_L$ was 1 M $\Omega$ . ....	37

Figure 2.15 (a) Device structure of inverted organic solar cells prepared for light-induced degradation experiments. (b) Solar cell reliability test system in Center for Multiscale Energy System at Seoul National University. ....	39
Figure 3.1 (a) Schematic illustration of a PTB7:PC <sub>71</sub> BM solar cell with the CdSe TP charge extraction nanostructure. The detailed role of CdSe TPs is illustrated below; CdSe TPs can extract photogenerated electrons in PC <sub>71</sub> BM domain by providing vertical transport pathway through their arms. (b) An energy level diagram of PTB7:PC <sub>71</sub> BM solar cells with CdSe TPs. ....	43
Figure 3.2 (a) A transmission electron microscopy (TEM) image of CdSe TPs tailored for a PTB7:PC <sub>71</sub> BM BHJ layer. Detailed dimensions of vertically-standing CdSe TPs are illustrated on the right. A top scanning electron microscopy (SEM) image of the charge extraction nanostructure fabricated with (b) 0.5 mg mL <sup>-1</sup> and (c) 4 mg mL <sup>-1</sup> of CdSe TP solution on top of ZnO:In layer. All scale bars are 100 nm. ..	45
Figure 3.3 <i>J-V</i> characteristics of PTB7:PC <sub>71</sub> BM solar cell having different arm lengths of CdSe TPs (52 nm and 98 nm) under the dark (filled symbol) and illuminated (open symbol) conditions. ....	46
Figure 3.4 Top SEM images of (a) CdSe TP film before coating a PTB7:PC <sub>71</sub> BM layer, (b) spin-coated active layer film on top of CdSe TPs, and (c) recovered CdSe TP film by eliminating active layer with chloroform washing.....	47
Figure 3.5 (a) A cross-sectional TEM image of the PTB7:PC <sub>71</sub> BM solar cell with CdSe TPs. (b) A dark field cross-sectional TEM image of the solar cell device with CdSe TPs and energy dispersive X-ray spectroscopy (EDS)	



mapping: (c) Zinc (from a ZnO:In layer), Sulfur (from PTB7), Cadmium, and Selenium (from CdSe TPs). .....	49
Figure 3.6 (a) High binding energy cutoff and valence band region in UPS spectra of a bare ZnO:In film and films with CdSe TPs. (b) UV-Vis absorption spectrum of PTB7:PC <sub>71</sub> BM and spectra of CdSe TPs with different concentration on top of ZnO:In film. Enlarged graph for absorption edge of CdSe TPs is shown in the right side of panel b. ....	50
Figure 3.7 (a) A top SEM images of CdSe TPs with different concentration (0, 0.5, 1, and 2 mg mL <sup>-1</sup> ). At higher concentration, CdSe TPs are getting aggregated, forming TP clusters. All image sizes are 400 nm × 300 nm. (b) Relationship between the areal number density (#/μm <sup>2</sup> ) and the concentration of CdSe TPs. The number of TPs within the area of 0.12 μm <sup>2</sup> was counted through the SEM images to estimate the areal number density. ....	52
Figure 3.8 Current density ( <i>J</i> ) - voltage ( <i>V</i> ) characteristics of the PTB7:PC <sub>71</sub> BM solar cells without and with the 250 μm <sup>-2</sup> of CdSe TPs, measured under the (a) AM1.5G 1 sun illumination and (b) dark condition. (c) Short circuit current density ( <i>J</i> <sub>SC</sub> ), fill factor (FF), and (d) power conversion efficiency (PCE) as a function of the areal number density of CdSe TPs. The inset of (b) shows the equivalent circuit diagram for solar cells. Dark current fitting is done using this solar cell equivalent circuit model. ....	53
Figure 3.9 (a) IPCE spectra of PTB7:PC <sub>71</sub> BM solar cells without and with CdSe TPs. (b) UV-Vis absorption spectra of PTB7:PC <sub>71</sub> BM films without and with the CdSe TP layer. ....	56

Figure 3.10 (a) Light intensity dependence of short circuit current density ( $J_{SC}$ ) for cells without and with CdSe TPs. Dotted lines show fitting curves using a power law. (b) Open circuit voltage ( $V_{OC}$ ) of cells without and with CdSe TPs as a function of light intensity, together with linear fits. ....	61
Figure 3.11 $J$ - $V$ characteristics of cells without and with CdSe TPs measured at various incident light intensity (5-100 mW cm <sup>-2</sup> ). Collection voltages ( $V_C$ ) are defined by the intersection of all linear fits at short circuit condition. The insets of (a) and (b) show $R_{SC}$ extracted around $V = 0$ , and calculated $V_C$ from the relation of $V_C = R_{SC}J_{SC}$ . ....	64
Figure 4.1 (a) Current density–voltage ( $J$ – $V$ ) characteristics of PTB7:PC <sub>71</sub> BM solar cell before and after light-induced aging for 24 h of continuous illumination, and detailed variation of normalized performance parameters of (b) $J_{SC}$ , (c) $V_{OC}$ , (d) FF, and (e) PCE with respect to the illumination time. ....	70
Figure 4.2 Optical microscope images of PTB7:PC <sub>71</sub> BM films (a and c) before and (b and d) after light-induced aging process with magnifications of (a and b) 50X and (c and d) 100X. ....	73
Figure 4.3 UV-Vis absorption spectra of PTB7:PC <sub>71</sub> BM films, deposited on top of ZnO nanoparticles, before and after light-induced aging for 24 h of continuous illumination. ....	74
Figure 4.4 (a and b) Topographic and (c and d) conductive AFM images of PTB7:PC <sub>71</sub> BM films before and after 24 h of continuous illumination. The height and current images were taken at the same time within the same area, and all images are $3 \times 3 \mu\text{m}^2$ . ....	75
Figure 4.5 The wide XPS spectra and high resolution spectra of F 1s, O 1s, C 1s, and S 2p for PTB7:PC <sub>71</sub> BM active layer before and after 24 h of light-	

induced aging. The quantified results of surface atomic concentrations are shown in the inset table. ....	76
Figure 4.6 (a) Dark $J$ - $V$ characteristics on a semi-logarithmic scale and (b) IPCE spectra for PTB7:PC <sub>71</sub> BM solar cells before and after light-induced aging. The equivalent circuit diagram used for data fitting is shown in the inset of (a).....	78
Figure 4.7 Light intensity dependence of (a) short circuit current density ( $J_{SC}$ ) and (b) open circuit voltage ( $V_{OC}$ ) for the devices before and after aging process for 24 h. Dotted lines in (a) and (b) define power-law and linear fitting curves, respectively, and their fitting parameters are shown in the figures.....	80
Figure 4.8 Collection voltages ( $V_C$ ) of (a and b) fresh and (c and d) 24 h of light-induced aged devices. (b) and (d) show extracted short circuit resistance ( $R_{SC}$ ) at $V = 0$ , and each point relates to the different incident light intensity (5-100 mW cm <sup>-2</sup> ). ....	82
Figure 4.9 Nyquist plots measured under various illumination intensities (1, 3, 10, 50, and 100 mW cm <sup>-2</sup> ) at open circuit conditions for PTB7:PC <sub>71</sub> BM solar cell devices (b) before and (c) after 24 h of light-induced aging. The marked voltages in figures represent to open circuit voltages, which were applied to devices, and (a) shows an equivalent circuit model used for data fitting.....	85
Figure 4.10 Fitting parameters of (a) contact ( $R_C$ ), bottom ZnO/bulk interface ( $R_{I1}$ ), (b) bulk ( $R_B$ ), and top bulk/MoO <sub>x</sub> /Ag interface ( $R_{I2}$ ) resistance values for the devices before and after light aging as a function of light intensity. ....	87

Figure 4.11 (a)  $J$ - $V$  characteristics and (b) Nyquist plots for PTB7:PC<sub>71</sub>BM solar cells with various thicknesses of MoO<sub>x</sub> layer (10, 50, and 100 nm). Two different fitting curves are shown in (c and d) for the same experimental data of the device with (c) 50 nm-MoO<sub>x</sub> and (d) 100 nm-MoO<sub>x</sub>: “ $R_{I1}$  &  $R_B$  fixed” and “ $R_B$  &  $R_{I2}$  fixed”. Fixed parameters here are from the values of fitting results for the device with 10 nm of MoO<sub>x</sub>. (e) Summarized fitting parameter values ( $R$  and  $C$ ) when  $R_{I1}$  and  $R_B$  are maintained with the same values of 10 nm-MoO<sub>x</sub> device.....88

Figure 4.12  $J$ - $V$  characteristics of hole-only-devices (a) before and (b) after light-induced aging with a structure of ITO/PEDOT:PSS/PTB7:PC<sub>71</sub>BM/MoO<sub>x</sub>/Au, measured at various temperatures. (c) Calculated electrical conductivity of active layer as a function of temperature for fresh and aged devices. (d) Temperature dependence of  $I$  from Equation (2.18) and its linear fitting curve in order to extract the trap energy in 24 h-aged device. Dotted lines in (a) and (b) show fitting curves using space-charge-limited current conduction (SCLC) and trap-charge-limited current conduction (TCLC) model for fresh device and aged device, respectively.....90

Figure 4.13 Normalized photocurrent decay dynamics on a (a) linear scale and (b) log-log scale for devices before and after light-induced aging. Nd:YAG pulsed laser (pulse duration  $\sim 5$  ns,  $\lambda = 590$  nm) was used as an excitation source.....93

# List of Tables

Table 1.1 Performance parameters of organic solar cells using various types of metal oxides as charge extraction interlayer. ....	9
Table 3.1 Performance parameters of inverted PTB7:PC <sub>71</sub> BM solar cells without and with different concentration of nanostructured CdSe TPs under AM 1.5G 1sun illumination. <sup>a</sup> .....	54
Table 3.2 Fitted parameters calculated from the dark curve of PTB7:PC <sub>71</sub> BM solar cells without and with nanostructured CdSe TPs.....	58
Table 3.3 Calculated parameters of collection voltage ( $V_C$ ), collection length ( $l_{C0}$ ) and collection efficiency ( $\eta_{C0}$ ) at short circuit condition, and effective $\mu\tau$ product ( $\mu\tau_{eff}$ ) for solar cell devices without and with CdSe TPs. ....	65
Table 4.1 Characteristics of PTB7:PC <sub>71</sub> BM solar cell devices before and after 24 h of the light-induced aging. $J_{SC}$ , $V_{OC}$ , FF, and PCE were measured under the 1 sun illumination condition, and fitted parameters of $J_0$ , $n$ , $R_S$ , and $R_{SH}$ were calculated from the dark $J$ - $V$ curve in Figure 4.6a. ....	71
Table 4.2 Fitting parameter values (R and C) extracted from the impedance spectroscopy using solar cell equivalent circuit model shown in the Figure 4.9a. $R_C$ represents contact resistance, and three RC components are	

assigned as bottom ZnO/bulk interface ( $R_{11}$ & $C_{11}$ ), bulk ( $R_B$ & $C_B$ ), and	
top bulk/MoO <sub>x</sub> /Ag interface ( $R_{12}$ & $C_{12}$ ). .....	86

# Chapter 1

## Introduction

Renewable energy is an essential part of reducing worldwide carbon emissions by responding to the global climate change. Fossil fuels have been the world's primary energy source until now; however, they give lots of negative effects on our environment. When they are burnt, gases including carbon dioxide (CO<sub>2</sub>) are released. Since carbon dioxide is known to one of the primary reasons for formation of global warming, developing and using renewable energy sources including solar, wind, hydropower, biomass, and geothermal is necessary.

Among the possible renewable energy sources, solar cells, which convert sunlight into electricity, are expected to be the most promising one as sustainable and infinite source (approximately 86,000 TW) of clean energy. Figure 1.1 shows that solar photovoltaic (PV) power system demonstrates the highest average annual growth rates during the last five years among the renewable energies. By virtue of

this rapid development of solar energy industry, cumulative PV solar cell capacity reached more than 200 GWs in 2015 as shown in Figure 1.2.

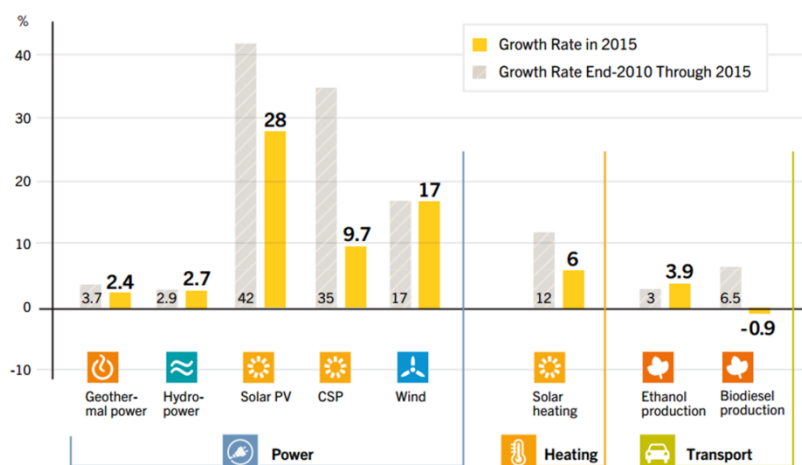


**Figure 1.1** Average annual growth rates of renewable energy capacity and biofuels production from the end of 2010 to the end of 2015. (Source : Renewables global status report 2016)

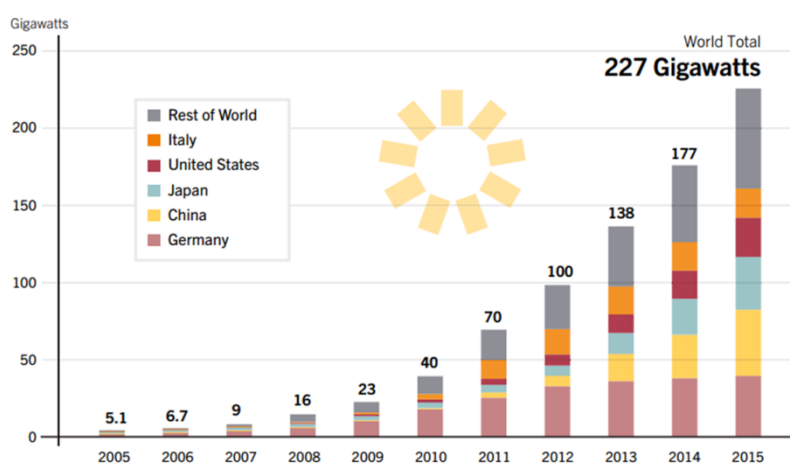


**Figure 1.2** Solar photovoltaic global capacity, by country and region, 2005–2015. (Source : Renewables global status report 2016)



## 1.1 Organic Solar Cells

Solar cells are typically categorized into three generations, according to cost and efficiency of the cells. The first generation solar cells are mainly based on silicon wafers, which demonstrate a performance about 15-20 %. These types of solar cells have dominated the market until now; however, they required a lot of energy to be produced at the early stage of Si solar cell technologies, so the cost was quite expensive (module cost per watt in 2007 :  $> 3.0$  \$ /W).

The second generation contains amorphous silicon, Copper Indium Gallium Selenide (CIGS), and Cadmium Telluride (CdTe) types of solar cells based on thin film technology that have a lower efficiency (10-15 %), but are much cheaper to produce than cells in first generation. Since the second generation solar cells have a lower material consumption due to thin active layer, it has been possible to reduce costs compared to the first generation.

To meet both low cost and high performance, which is the goal for third generation (or next-generation) solar cells, technical breakthroughs are required in the view of materials as well as fabrication process. Most technologies in this generation are not yet commercialized, but a lot of researches are going on in this area, including dye-sensitized solar cells, organic solar cells, perovskite solar cells, and quantum dot solar cells. They all have advantages of cost, since they can be fabricated with cost-effective roll-to-roll (R2R) technologies through the solution process.

Figure 1.3 shows the relationship between efficiency, module areal costs, and cost per peak watt (in \$/Wp). For third generation (or next-generation) technologies, the goal is to achieve 0.3-0.5 \$/Wp (blue shaded region in Figure 1.3), which can be realized by solar cells with high performance and low cost. Not only the emerging

photovoltaics but Si solar cells are also coming to this region by continuous efforts for cost reduction. (module cost per watt in 2015 : 0.57 \$ /W, Source : GTM Research PV Pulse, Mar. 2016).

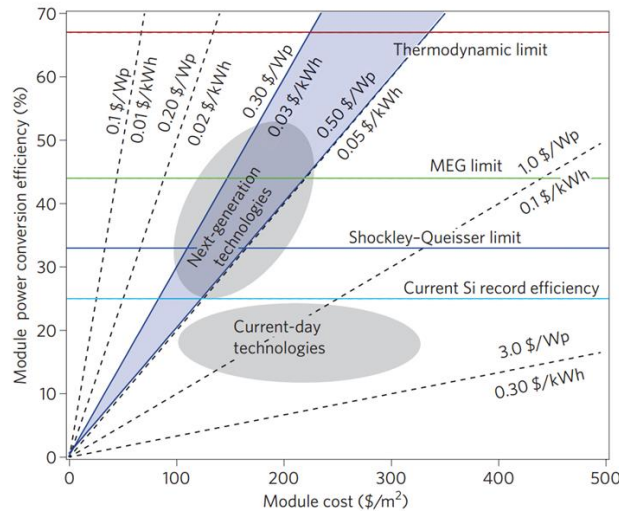


**Figure 1.3** Relationship between power conversion efficiency, module areal costs, and cost per peak watt (in \$/Wp).[1] © 2014 Nature Publishing Group. For next-generation (or third generation) technologies the goal is to reach 0.3-0.5 \$/Wp, denoted by the blue shaded region.

Organic solar cells are one of the most promising candidates for third generation solar cells, due to their potential of simple and low cost process to be commercialized in flexible, light-weight, and large-area devices.[2, 3] With these advantages, organic solar cells can target new and niche applications, such as portable solar battery chargers, clothing, car windows, and so on. Although efficiency of organic solar cells is still low compared to the inorganic counterparts, the record efficiency has been gradually increased since C. W. Tang reported first

bilayer organic solar cell in 1986.[4] The power conversion efficiency (PCE) of polymer:fullerene bulkheterojunction (BHJ) solar cells have already gone beyond 10 % in single junction by the benefit of multidirectional efforts containing the development of new materials, device architectures, and processes.[5-8] As shown in Figure 1.4, recently 11.5 % of PCE was achieved in single cell structure,[9] and 10.6 % was reported in tandem structure.[10] The state of the art and remaining challenges of organic solar cells will be discussed in a subsequent chapter.

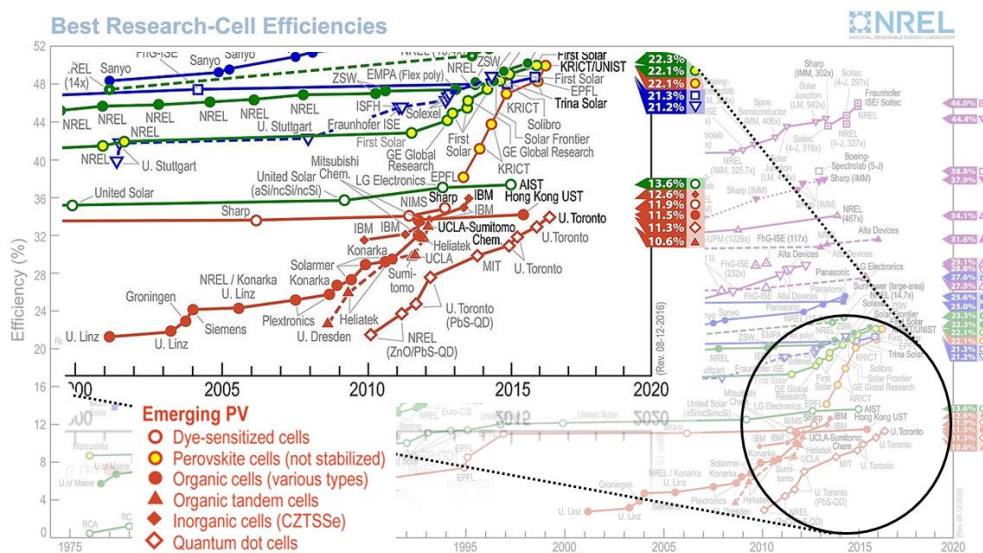


**Figure 1.4** Best research solar cell efficiencies chart. Enlarged graph shows the reported timeline of efficiencies for organic solar cells (Source : National Renewable Energy Laboratory, Aug. 2016)

## 1.2 Current State of the Art and Challenges in Organic Solar Cells

Organic solar cells have drawn great attention due to their potential to be fabricated on low cost and large area by solution process. In addition, organic materials have an advantage over the inorganic counterparts in material flexibility. By designing and synthesizing the organic materials (usually *p*-type conjugated polymers), it is possible to control their physical properties, such as band gap, energy position of highest occupied molecular orbital (HOMO) or lowest unoccupied molecular orbital (LUMO), absorption ability, and carrier mobility.[11]

One of the classic polymers as a donor material is poly(3-hexylthiophene) (P3HT), and it has reached 4-5 % of PCE.[12, 13] However, it showed low current density because of its relatively large band gap (1.9 eV). Recently, low band gap polymers including poly[N-9'-hepta-decanyl-2,7-carbazole-alt-5,5-(4',7'-di-2-thienyl-2',1',3'-benzothiadiazole)] (PCDTBT), poly[[4,8-bis[(2-ethylhexyl)oxy]benzo[1,2-b:4,5-b']dithiophene-2,6-diyl][3-fluoro-2-[(2-ethylhexyl)carbonyl]thieno[3,4-b]thiophenediyl]] (PTB7), and PTB7 derivatives have been extensively reported for better light harvesting of solar spectrum.[14-16]

There are prerequisite conditions for organic solar cells to be commercialized, which are high performance, low cost, and high stability as shown in Figure 1.5. For performance, with gradual efforts to improve PCEs containing the development of new low band gap polymer materials and device architectures, the highest efficiency above 10 % was reported in single-cell structure, approaching the efficiency threshold for commercial viability.[5-7] In order to further increase in efficiency of organic solar cells, continuous progress from the points of view of materials, optical enhancement, fabrication methods, and charge extraction techniques is important.

Low cost is known as one of the main advantages in organic solar cells both in terms of material itself and fabrication methods. Due to their solution-processable properties, manufacturing costs will be low ( $< 0.5\$/\text{Wp}$ ) by using spin-coating, ink-jet printing, and roll-to-roll (R2R) technologies.

Stability also has to be guaranteed for organic solar cells to be in market; however, it remains a great challenge so far to reach a goal of more than 5 year lifetime. There are factors limiting the stability in organic solar cells, such as oxygen and moisture, heat, and light irradiation.[17-21] Therefore, systematic investigation to understand degradation mechanism is important for overcoming the challenges to achieve highly stable organic solar cells.

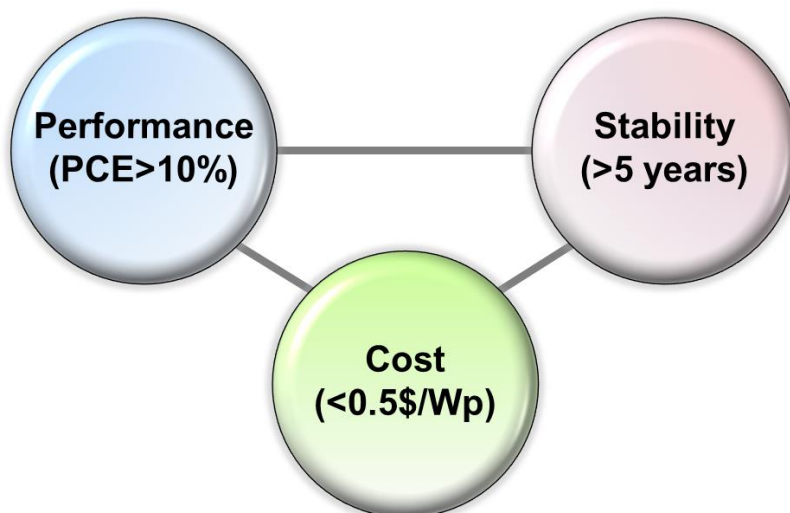


**Figure 1.5** Requirements for commercialization of organic solar cells.

### 1.2.1 Progress in Efficiency Improvement of Organic Solar Cells

Efficiency of organic solar cells has been steadily improved as shown in Figure 1.4 through a lot of efforts. Along with the development of organic materials,[5, 22, 23] optical engineering,[7, 24] and new processing techniques,[9] the improvement of charge extraction properties has become a key topic for high performance organic solar cells. In order to enhance charge extraction characteristics, *interlayer* (or buffer layer) between electrode and light-absorbing layer is the most important to extract generated electrons and holes as efficiently as possible toward the electrodes. This interlayer should meet good optical transparency, charge transport and extraction properties with suitable energy band positions.

Metal oxides thin films are one of the most promising candidates for efficient charge extraction layers by virtue of their good carrier transport characteristics with appropriate energy level as well as optical transparency in the visible region. As hole extraction layer, metal oxides including MoO<sub>x</sub>,[25, 26] V<sub>2</sub>O<sub>5</sub>,[25, 27] WO<sub>3</sub>,[28] and NiO[29] are usually employed in organic devices, while SnO<sub>2</sub>,[30] TiO<sub>2</sub>,[31] and ZnO[32, 33] are widely used for electron extraction layer.

To collect photogenerated charge carriers more efficiently from the active layer to electrode, there also have been efforts applying conjugated polyelectrolytes (CPEs),[34, 35] metal doping,[36-39] and nanostructures[40, 41] to the metal oxides. Choi *et al.*[34] reported that the incorporation of thin CPE interfacial layer between titanium oxide and active layer can enhance the device performance by reducing the electron extraction barrier through the vacuum level shift. On the other hand, doped metal oxides also have been used as interlayer for efficient charge extraction, since the doping of semiconductors is known to greatly affect their properties, especially electrical characteristics such as electron mobility and conductivity toward increased

direction.[36-39, 42] Furthermore, nanostructured metal oxides, such as nanowires-, rods-, or wrinkles-shaped, were applied to enhance the power conversion efficiency of solar cells. Liu *et. al.*[40] demonstrated that through the nanowires structure of metal oxides, increased interfacial area and more continuous path for charge transport could be given, enhancing the short circuit current and overall performance of solar cells. Selected performance parameters of organic solar cells which employ metal oxides interlayer as charge extraction layer are summarized in Table 1.1.

**Table 1.1** Performance parameters of organic solar cells using various types of metal oxides as charge extraction interlayer.

Type	Interlayer	Active layer	$J_{sc}$ (mA cm <sup>-2</sup> )	$V_{oc}$ (V)	FF (%)	PCE (%)	Ref.
Thin films	MoO <sub>x</sub>	P3HT:PC <sub>60</sub> BM	8.94	0.60	61.9	3.33	[25]
	V <sub>2</sub> O <sub>5</sub>	P3HT:PC <sub>60</sub> BM	8.83	0.59	59.1	3.10	[25]
	WO <sub>3</sub>	Si-PCPDTBT: PC <sub>71</sub> BM	12.8	0.62	60.4	4.8	[28]
	NiO	P3HT:PC <sub>60</sub> BM	11.3	0.64	69.3	5.16	[29]
	SnO <sub>2</sub>	P3HT:PC <sub>60</sub> BM	9.89	0.58	56	3.23	[30]
	TiO <sub>2</sub>	P3HT:PC <sub>60</sub> BM	11.1	0.61	66	5.0 <sup>a</sup>	[31]
	ZnO	PCDTBT: PC <sub>71</sub> BM	10.41	0.88	68.8	6.33	[33]
Incorporation of CPEs	TiO <sub>x</sub> / FPQ-Br	P3HT:PC <sub>60</sub> BM	8.85	0.58	70	3.55	[34]
	ZnO/ PFN-Br	PBDT-DTNT: PC <sub>71</sub> BM	17.4	0.75	61	8.4	[35]
Metal doping	Ga-doped ZnO	PTB7:PC <sub>71</sub> BM	14.96	0.75	65.0	7.34	[37]
	Al-doped ZnO	PTB7-Th: PC <sub>71</sub> BM	17.91	0.80	72.3	10.4	[38]
	In-doped ZnO	PCDTBT: PC <sub>71</sub> BM	12.28	0.88	51.7	5.58	[39]
Nanostructured	ZnO nanowires	CuPC:C <sub>60</sub>	3.86	0.46	30	0.53	[40]
	ZnO nano- patterned	PBDTTT-C-T: PC <sub>71</sub> BM	12.95	0.73	57	5.43	[41]

<sup>a</sup>Device was measured under a solar simulator with irradiation intensity of 90 mW cm<sup>-2</sup>.

Inorganic nanocrystals (NCs), which have strengths in superior electrical characteristics, easily tunable band gap, and solution processability[43, 44] are introduced as an interlayer in **Chapter 3** of this thesis. Organic-inorganic NCs hybrid system based solar cells have already been widely reported; however, most of the results employed NCs as electron acceptor in combination with electron donor of conjugated polymer.[45-47]

In order to realize charge extraction interlayer of inorganic NCs, the colloidal tetrapod (TP)-shaped NCs were chosen due to their structural uniqueness and controllability as shown in Figure 1.6. The tetrapod morphology is the simplest architecture which can stably stand on a substrate owing to its low center of mass, so that vertically-oriented inorganic channels can be easily produced on the substrate by simple spin-coating process. In a case of carrier transport, TPs are intended to give more effective pathway through their branches based on the conduction mechanism rather than hopping mechanism of quantum dot-shaped NCs.

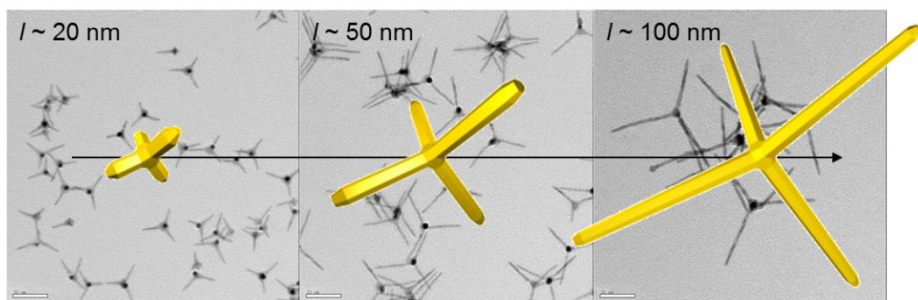


**Figure 1.6** Transmission electron microscopy (TEM) images and schematic illustration of CdSe TPs with controlled arm lengths ( $l$ ). All scale bars are 50 nm.



### 1.2.2 Stability/Degradation of Organic Solar Cells

As efficiency growths are making progress toward the commercial practicality of organic solar cells, the importance of stability issues has been highlighted simultaneously. However, stability and degradation of organic solar cells are yet to be proven, therefore, systematic study about degradation mechanisms which happens inside the device is important.

There are four main factors, which are known to degrade organic devices: oxygen, moisture, heat, and light.[19-21, 48] Oxygen and moisture molecules are considered as important degradation factors because they can vertically penetrate into active layer through microscopic pinholes of top electrode.[17, 19] By diffusing from the organic/metal electrode interface, oxygen and moisture can lead to the degradation of organic underlayers.

In addition, Bertho *et al.* reported in 2007[20] that thermal energy above glass transition temperature ( $T_g$ ) of polymer can make macroscopic phase separation in bulkheterojunction geometry, hence high  $T_g$  PPV-based solar cells showed better thermal stability due to their firmer matrix of polymers. That is, maintaining a stable morphology of active layer can efficiently suppress the deterioration in solar cell performances.

Among the degradation factors, light is the most crucial issue to be solved because not only is it an intrinsic reaction, but the sunlight is also known to accelerate the reaction with oxygen.[49, 50] Furthermore, solar cells are inevitably operated under the light illumination condition. Recent studies have shown that there is fast initial performance drop, which is called burn-in loss, in organic solar cells during the continuous light exposure.[49] Reese *et al.*[51] revealed that conventional P3HT:PCBM devices, which were continuously illuminated under the

light source of tungsten halogen bulbs in an inert atmosphere, exhibited a 60 % loss in power conversion efficiency after 200 h of illumination. Recently, Tamai *et al.*[52] reported that decrease of power conversion efficiency for P3HT:ICBA blend cells resulted in an 60 % reduction during the 45 h of light exposure under the AM1.5G simulated solar illumination. This burn-in loss is a major drawback for commercialization, therefore, it is highly required to systematically study about photo-induced degradation mechanism. Several light-induced mechanisms have already been proposed with the well-known P3HT-based solar cells:[17, 53-58] chemical structure modification of P3HT and P3HT:PCBM film,[53] large phase segregation in morphology,[54] photo-induced oxidation of PC<sub>60</sub>BM,[55] electrical deterioration,[56, 57] and interface degradation.[58]

Manceau *et al.* investigated the effects of long-term light irradiation on P3HT and P3HT:PCBM active layer in the absence of oxygen through UV-visible and infrared (IR) spectroscopies.[53] The authors found that the 10,000 h light irradiation of P3HT provoked the modification of its chemical structure, such as a reduction of the conjugation length in the macromolecular backbone and a decrease of the IR absorption bands of the various polymer functional groups (thiophene rings, aromatic C-H, and alkyl groups), all leading to the UV-Vis absorbance decrease. The degradation rate was strongly attenuated, on the other hand, when P3HT is blended with PCBM due to the radical scavenging properties of the fullerene and its ability to quench the P3HT singlet state, remaining in chemically stable state during the 10,000 h of artificial accelerated light aging.

The same authors extended this study to P3HT:PCBM deposited on PEDOT:PSS system in order to make more connection with solar cell devices.[54] It concludes that P3HT:PCBM blend deposited on a PEDOT:PSS layer has undergone the formation of large PCBM aggregates after the long-term (~ 6,000 h)

photochemical aging, which can possibly hinder the exciton dissociation and charge transport properties, resulting in degradation of device performances at last.

Reese *et al.* also conducted the investigations on the changes in absorbance and photoconductance of P3HT and P3HT:PCBM blended films under the illumination both in inert and ambient conditions.[55] They concluded that under inert atmosphere, both the polymer and the blend are stable for at least 1,000 h of one sun illumination, which is consistent with the above results.[53, 54] Under exposure to air and light, however, the photoconductance of the blend decreased during degradation due to the oxidation series of PCBM. They argued that these oxidized molecules serve as deep traps through decreased electron mobility, having an impact on the device lifetime.

Studies from Yang's group demonstrated about electrical degradation of P3HT:PCBM solar cells exposed under X-rays irradiation.[56] They found that whereas no structural changes take place in polymer solar cells when subjected to high radiation doses, electrical deterioration, especially charge carrier accumulation, is thought to be a severe problem resulting in temporary degradation in solar cell performance. Another work by Khelifi *et al.* observed that the effect of photodegradation on electrical transport and charge extraction for P3HT:PCBM solar cells under continuous illumination in nitrogen atmosphere.[57] With various measurements including admittance spectroscopy and numerical device modeling tool, the authors determined that initial degradation of electrical properties during 250 h is mainly caused by the increased density of deep traps in the blend.

Williams *et al.* reported about photo-stability behavior of P3HT:PCBM solar cells by applying different hole and electron extraction layers in between organic and electrode interfaces.[58] They concluded that exposure to light results in degradation in all parameters of devices, and inserting the charge extraction layer

between the organic layer and aluminum electrode can suppress contact photo-degradation and enhance photo-stability.

For high performance solar cells with recently developed materials, on the other hand, studies of degradation mechanism have been limited. Considering the aging mechanisms also greatly depend on the organic materials of active layer, it is required to explore the mechanisms for high performance polymer-based solar devices. In *Chapter 4*, investigation of light-induced degradation mechanisms of PTB7:PC<sub>71</sub>BM based organic solar cells are discussed.

## 1.3 Outline of Thesis

This thesis is divided into five chapters.

In the introduction of *Chapter 1*, brief overview of organic solar cells and their current state of the art and challenges were explained, especially in terms of efficiency improvement and understanding of degradation mechanism.

*Chapter 2* surveys the basic device physics of organic solar cells, materials used in this thesis, and device fabrication methods. In addition, characterization methods including optical and electrical techniques are described.

In *Chapter 3*, to enhance the charge extraction properties for high performance solar cells, the electron-selective interlayer of inorganic CdSe TP-shaped nanocrystals are introduced, and their device performances are investigated including the analysis of recombination and charge collection characteristics.

In *Chapter 4*, to understand the degradation mechanisms especially for high performance polymer-based solar devices, the light-induced degradation of PTB7-based organic solar cells in the first 24 hours are demonstrated. The morphological and electrical characteristics of active layer and devices are investigated by various measurement techniques to figure out the origin of photo-induced degradation.

In *Chapter 5*, the results obtained are summarized and concluding remarks of this thesis are given.

## **Chapter 2**

# **Theory and Experimental Methods**

## **2.1 Basic Device Physics of Organic Solar Cells**

### **2.1.1 Working Principle of Organic Solar Cells**

Like all photovoltaic cells, organic solar cell converts solar energy (light) into electricity, and its working principle is shown in Figure 2.1. While free carriers are directly generated through the photon absorption in inorganic solar cells, excitons, i.e. electron-hole pair bound together by electrostatic force, are produced (Figure 2.1 (1)) in organic solar cells. Then, these generated excitons diffuse until they either recombine or reach at the donor and acceptor interfaces, where they are broken up into electrons (black) and holes (white) by effective built-in potential. (Figure 2.1 (2 and 3)) The separated electrons and holes are then collected to cathode and anode, respectively, generating electricity. (Figure 2.1 (4))

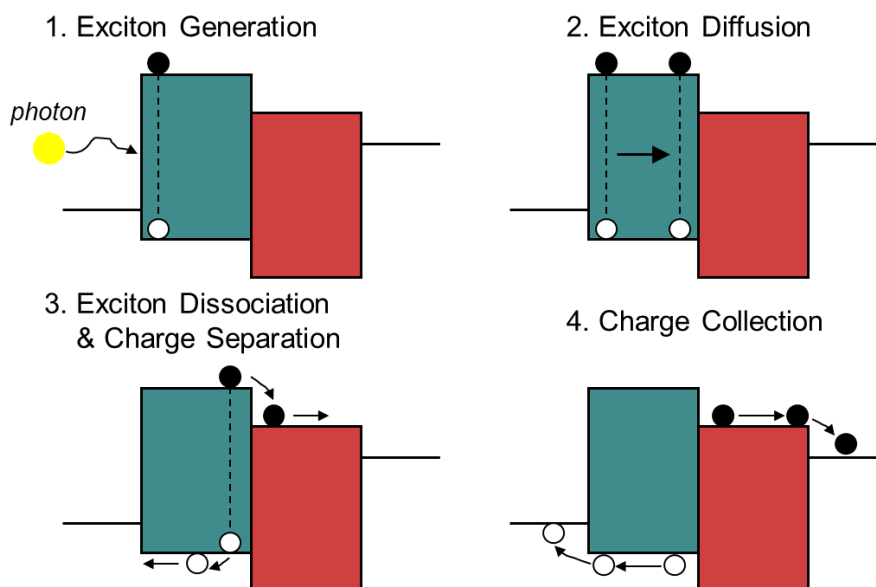


**Figure 2.1** The working principle of organic solar cells.

### 2.1.2 Solar Cell Performance Parameters

In order to determine the performance and electrical characteristics of the photovoltaic devices, current density-voltage ( $J$ - $V$ ) measurements are performed under the illumination of solar simulator which can provide approximating natural sunlight. A typical  $J$ - $V$  characteristic of a solar cell is shown in Figure 2.2.

The current under illumination when the voltage across the solar cell is zero is called short-circuit current density,  $J_{SC}$ . This is the maximum current delivered by a solar cell, and it depends on the optical properties (absorption and reflection) as well as electrical properties (exciton dissociation, carrier transport, and charge collection) of active layer.

The open-circuit voltage,  $V_{OC}$ , is the maximum voltage that solar cell is able to supply, and occurs when the net current through the device is zero. In organic solar cells,  $V_{OC}$  is known to be mainly determined by the energy offset between the

highest occupied molecular orbital (HOMO) of donor and the lowest unoccupied molecular orbital (LUMO) of acceptor materials.[59, 60] Reverse saturation current, recombination, or defect states are factors that influence the open-circuit voltage in organic solar cells.

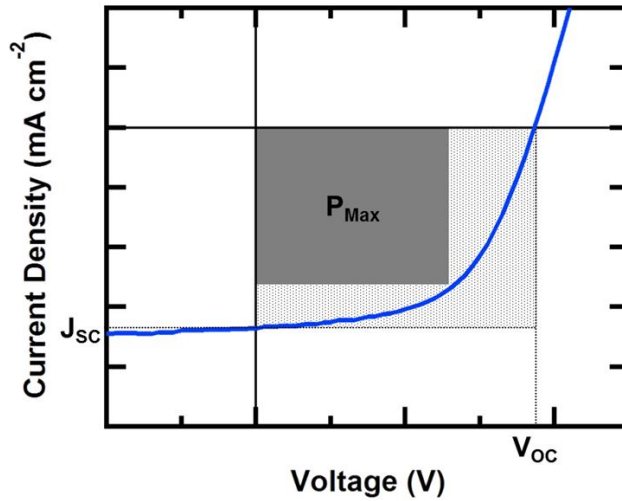


**Figure 2.2** Current density-voltage ( $J$ - $V$ ) curve of solar cell.

While the power from the solar cell is zero at the operating points of both  $J_{SC}$  and  $V_{OC}$ , there is a point where the solar cell can deliver its maximum power ( $P_{Max}$ ) to an external load. The fill factor, FF is defined as the ratio of the maximum power generated from the solar cell to the product of  $V_{OC}$  and  $J_{SC}$ , which is shown in equation (2.1).

$$FF = \frac{P_{Max}}{J_{SC} \times V_{OC}} \quad (2.1)$$

The FF can also be graphically defined as the ratio of the area of the maximum possible largest rectangle (dark grey region in Figure 2.2), which fits in the  $J$ - $V$



curve, to the rectangle formed with  $V_{OC}$  and  $J_{SC}$ . The ideal value for FF is unity (100%), if all the generated charge carriers are extracted out of a device without any losses. In typical organic solar cells, however, FF is usually in the range of 50-80 %, since there are factors which influence FF in organic solar cells including parasitic resistive losses and current leakages.

The efficiency of a solar cell, which is defined as the fraction of incident power converted to electricity, is the most commonly used parameter to show the performance of solar cells. The power conversion efficiency,  $PCE$ , is given by

$$PCE (\%) = \frac{\text{Electric Power}}{\text{Light Power}} = \frac{V_{OC} \times J_{SC} \times FF}{P_{\text{light}}} \times 100 (\%) \quad (2.2)$$

where  $P_{\text{light}}$  is the incident power of light. The efficiency is needed to be measured under the standard test conditions for comparing performances from one to another, because it has a dependence on spectrum and intensity of incident sunlight. The standard condition includes an irradiance of 1 sun ( $100 \text{ mW cm}^{-2}$ ) with an air mass 1.5 global (AM 1.5G) solar spectrum as shown in Figure 2.3.

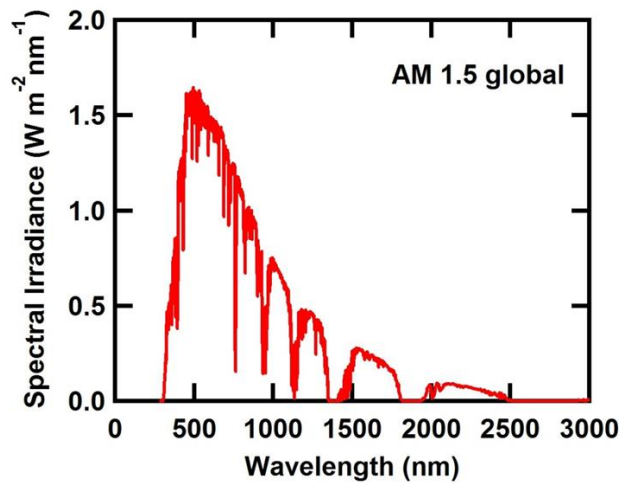


**Figure 2.3** AM 1.5G spectral distribution of solar irradiation.

The quantum efficiency ( $QE$ ) is the ratio of the number of charge carriers collected by the solar cell to the number of photons of a given wavelength incident on the solar cell. In solar cells, two types of  $QE$  are often considered: external quantum efficiency ( $EQE$ ) and internal quantum efficiency ( $IQE$ ).  $EQE$ , also known as  $IPCE$  (incident photon-to-current conversion efficiency), is the ratio of the number of charge carriers collected by the solar cell to the number of photons of a given energy shining on the solar cell from outside (incident photons). On the other hand,  $IQE$  is the ratio of the number of charge carriers collected by the solar cell to the number of photons of a given energy that shine on the solar cell from outside and are absorbed by the cell.

$$EQE (\%) = \frac{\text{number of collected electrons in external load}}{\text{number of incident photons}} \quad (2.3)$$

$$\begin{aligned} IQE (\%) &= \frac{\text{number of collected electrons in external load}}{\text{number of absorbed photons}} \\ &= \frac{EQE}{1 - \text{Reflection} - \text{Transmission}} \end{aligned} \quad (2.4)$$

### 2.1.3 Equivalent Circuit Model

To understand the electronic properties of a solar cell, equivalent circuit model is useful, which consists of ideal electrical components whose behavior is well defined.

As shown in Figure 2.4, a solar cell can be modeled by a current source in parallel with a diode, a series resistance ( $R_s$ ), and a shunt resistance ( $R_{sh}$ ). In an ideal solar cell, the series resistance is zero and the shunt resistance is infinite. From the equivalent circuit, the current density of solar cell ( $J$ ) under illumination is given by the sum of the dark diode current density ( $J_{diode}$ ), leakage current density ( $J_{leak}$ ), and the photogenerated current density ( $J_{ph}$ ).

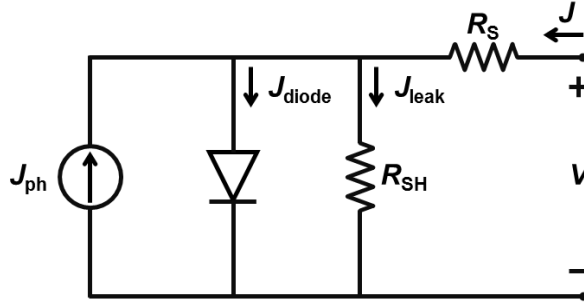


**Figure 2.4** The equivalent circuit diagram of solar cell under illumination.

$$J = J_{\text{diode}} + J_{\text{leak}} - J_{\text{ph}} \quad (2.5)$$

Here, voltage of solar cell ( $V$ ) can be expressed considering the voltage drop across the  $R_s$  as follows:

$$V = J_{\text{leak}} R_{\text{SH}} + J R_s \quad (2.6)$$

When combining two equations, Equation (2.5) and Equation (2.6), then current density of solar cell is given by

$$J = J_{\text{diode}} + \frac{V - J R_s}{R_{\text{SH}}} - J_{\text{ph}} = J_0 \left[ e^{\frac{q}{n k T} (V - J R_s)} - 1 \right] + \frac{V - J R_s}{R_{\text{SH}}} - J_{\text{ph}} \quad (2.7)$$

where,  $J_0$  is the reverse saturation current density,  $n$  is the diode ideality factor,  $q$  is the elementary charge,  $k$  is the Boltzmann constant, and  $T$  is the absolute temperature.

## 2.2 Materials

### 2.2.1 Materials

The followings are the details of materials used for solar cell fabrication in this thesis, and preparation methods using these materials are described in the following subchapters. Cadmium oxide powder (CdO, 99.95%) was obtained from Alfa Aesar. Selenium powder (99.99%), oleic acid (OA, 90%), n-trioctylphosphine (TOP, 90%), 1-octadecene (1-ODE, 90%), hexadecyltrimethylammonium bromide (HTAB, 99+%), chlorobenzene (99.8%), zinc acetate dihydrate ( $\text{Zn}(\text{ac})_2 \cdot 2\text{H}_2\text{O}$ ,  $\geq 98\%$ ), indium (III) nitrate hydrate ( $\text{In}(\text{NO}_3)_3 \cdot x\text{H}_2\text{O}$ , 99.99%), potassium hydroxide (KOH, 90%), ethanolamine ( $\geq 99.0\%$ ) and 1-hexylamine (99%) were purchased from Sigma-Aldrich. Methanol (99.8%) and 1,8-diiodooctane were obtained from Samchun Pure Chemical Co. and Tokyo Chemical Industry Co., respectively. Poly[[4,8-bis[(2-ethylhexyl)oxy]benzo[1,2-b:4,5-b']dithiophene-2,6-diyl][3-fluoro-2-[(2-ethylhexyl)carbonyl]thieno[3,4-b]thiophenediyl]] (PTB7) and [6,6]-phenyl-C71-butyric acid methyl ester ( $\text{PC}_{71}\text{BM}$ ) for photoactive materials were purchased from 1-Material, and these chemical structures and energy diagram are shown in Figure 2.5. All materials mentioned above were used as received without any further purification.

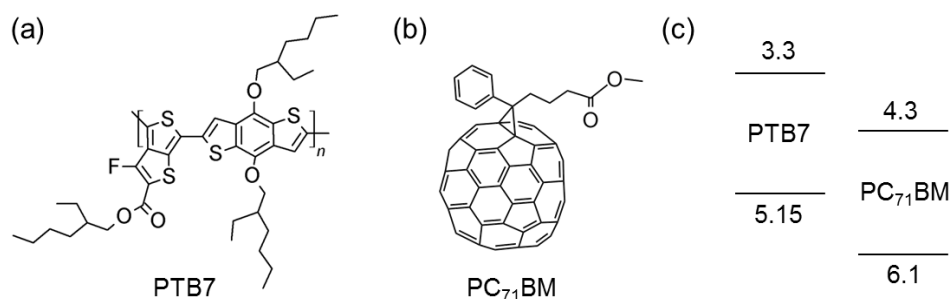


**Figure 2.5.** (a and b) Chemical structures and (c) an energy level diagram of PTB7 and PC<sub>71</sub>BM, which are used as photoactive materials in this thesis.

### 2.2.2 Preparation of ZnO Nanoparticles

ZnO nanoparticles (NPs) are used as electron extraction layer for inverted-type of organic solar cells in **Chapter 4**. For synthesizing ZnO NPs, method from Pacholski *et al.*[61] was a bit modified. First, the mixture of zinc acetate dihydrate (2.00 g) and methanol (80 ml) was in the 3-neck round bottom flask under the continuous stirring, and heated to 60 °C. At the stabilized temperature of 60 °C, 40 ml of KOH solution (mixture of 1.51 g of KOH flakes and 65 ml of methanol) was added dropwise into the zinc acetate dihydrate solution. Then, the reaction mixture was stirred for 2 h and 30 min keeping the temperature at 60 °C to yield milky solution containing ZnO NPs. The ZnO NPs were then isolated by centrifugation at 4000 rpm and re-dispersed in 1-butanol, resulting in a final concentration of about 50 mg mL<sup>-1</sup>.

### 2.2.3 Synthesis of CdSe Tetrapods and Their Surface Modification

In **Chapter 3**, CdSe tetrapod (TP)-shaped colloidal nanocrystals are used as electron-selective interlayer. To prepare the arm length-controlled CdSe TPs, synthetic process by Lim *et al.*[62] was partially modified. As arm growth precursors, cadmium oleate (Cd(OA)<sub>2</sub>) solution (reacting 10 mmol of CdO with 9 mL of OA in

5 mL of ODE and 1 mL of TOP at 280 °C) containing 0.14 mmol of HTAB and SeTOP solution (reacting 12 mmol Se with 6 mL TOP at 150 °C) were mixed under the inert atmosphere for 5 min. Then, 28 mL of the arm growth precursors was continuously injected into the seed solution (0.3  $\mu$ mol of CdSe seeds (diameter  $\sim$  5 nm) dissolved in 26.25 mL of ODE, 1.5 mL of TOP, 2.25 mL of OA and 0.21 mmol of HTAB) at 260 °C. Injection rate was fixed to 30 mL/hr. After the precursor injection was finished, the crude solution was immediately cooled down to ambient temperature and purified three times using acetone (for precipitation) and hexane (for re-dispersion). The final product was dispersed in hexane for surface modification.

Oleate ligands of CdSe TPs were replaced with oleylamine via two-phase ligand exchange procedure.[47] Briefly, oleate-capped CdSe TPs dispersed in non-polar organic phase (e.g., hexane) and polar DMF phase containing HBF<sub>4</sub> were put in a round-bottom flask and vigorously stirred to transfer the CdSe TPs to the DMF phase, which indicates the elimination of oleate ligands. Next, the bare CdSe TPs dispersed in the DMF phase were precipitated using acetone and re-dispersed in a mixture of chloroform and oleylamine (for example, 4 mL of chloroform and 1 mL of oleylamine). Then, the oleylamine-capped CdSe TPs were precipitated using acetone to remove excess oleylamine. Finally, chloroform was added to the precipitates to disperse CdSe TPs. Small amount of oleylamine was helpful to sustain colloidal stability of CdSe TPs over several weeks.

## 2.3 Device Fabrication Methods

To fabricate an inverted structure of organic solar cells having CdSe TPs as an electron-selective interlayer, which are discussed in *Chapter 3*, In-doped ZnO thin films (ZnO:In) have been firstly prepared by spin-coating of sol-gel precursor.  $\text{Zn}(\text{ac})_2 \cdot 2\text{H}_2\text{O}$  and  $\text{In}(\text{NO}_3)_3 \cdot x\text{H}_2\text{O}$  (5 at.% of the precursor) were dissolved in a mixture of ethanol and ethanolamine (ethanol:ethanolamine = 10:0.15 (v/v)) and stirred for 2 hours at room temperature to yield a homogeneous and clear solution. Then, as-prepared precursor solution was spin-coated on a ultraviolet-ozone treated ITO-coated glass at 3500 rpm for 40 sec and sequentially annealed in atmosphere from 120 to 450 °C for 2 hours, resulting in 30 nm-thick ZnO:In thin films.

To assembly CdSe TPs, the ZnO:In substrates were transferred to a glove box filled with Ar. Different concentration (0.5, 1, and 2 mg mL<sup>-1</sup>) of CdSe TP solutions was spun at 2000 rpm for 30 sec on top of the ZnO:In substrate, followed by annealing at 150 °C for 20 min. Following, the film was washed twice using ethanol at room temperature and annealed at 120 °C for 10 min to remove residual solvent and fix CdSe TPs on the ZnO:In substrate. Then, the CdSe TPs was modified with 1-hexylamine (acetone:1-hexylamine = 8:2 (v/v)) by spin-coating at 2000 rpm and dried at 100 °C for 10 min. Note that the series of thermal annealing and use of solvents showed no significant differences in electrical property of ZnO:In thin films. 25 mg mL<sup>-1</sup> of PTB7:PC<sub>71</sub>BM blend with a weight ratio of 2:3 dissolved in mixed solvent (chlorobenzene:1,8-diiodooctane (97:3 (v/v))) was spin-coated onto the CdSe TP electron extraction interlayer at 1000 rpm for 60 sec; the thickness of active layer is about 90 nm. Subsequently, 10 nm of MoO<sub>x</sub> and 100 nm of Al layers were thermally evaporated under a 10<sup>-6</sup> Torr vacuum. All the fabrication steps described above are briefly shown in Figure 2.6.

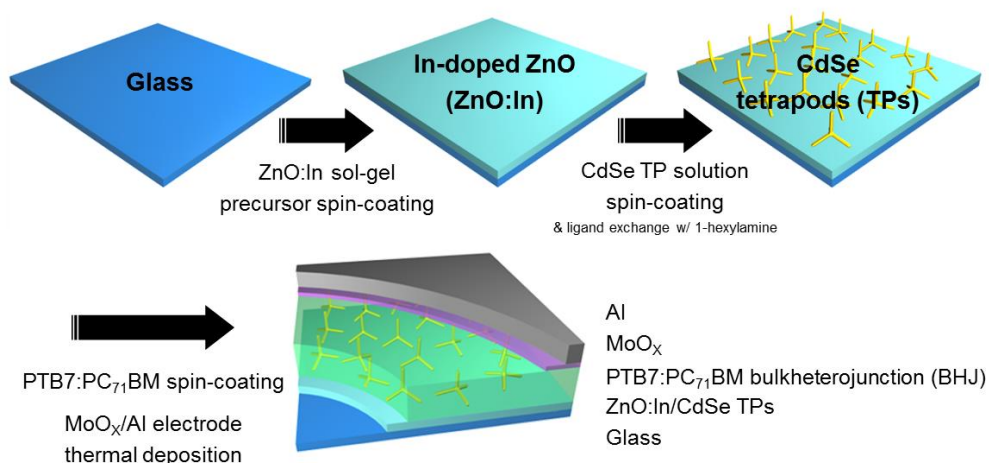


**Figure 2.6** Schematic of fabrication process and the structure of PTB7:PC<sub>71</sub>BM organic solar cells with electron-selective interlayer comprising of In-doped ZnO (ZnO:In) and vertically-aligned CdSe tetrapods (TPs).

Solar cells for understanding light-induced degradation mechanisms, which are discussed in *Chapter 4*, were fabricated on patterned ITO-coated glass substrates. In this time, ZnO nanoparticles (NPs) were used as electron extraction layer. 10 mg mL<sup>-1</sup> of ZnO NPs solution was spun on a patterned ITO at 2000 rpm for 60 sec and annealed at 100 °C for 30 min in N<sub>2</sub> atmosphere. Next, 25 mg mL<sup>-1</sup> of PTB7:PC<sub>71</sub>BM blend was prepared using the same recipe as above, and was spin-coated on top of ZnO NPs in an Ar-filled glovebox; the thickness of PTB7:PC<sub>71</sub>BM is 80 nm. The thickness was slightly different from above, and it is probably due to batch-to-batch variation of materials or different underlayer morphologies. Subsequently, 10 nm of MoO<sub>x</sub>, and 100 nm of Ag layers were thermally evaporated. The active areas of solar cells (overlapped electrodes) were 1.96 mm<sup>2</sup>. Then, the devices were encapsulated under inert atmosphere to minimize extrinsic factors, such as oxygen and moisture, during the light-induced aging process.



## 2.4 Thin Film Characterization Methods

### 2.4.1 Optical Measurements

**Absorption spectroscopy:** The absorption of sunlight is required for photoactive layer in organic solar cells to generate excitons so as to extract charge carriers into an external circuit. To know about the amount of light absorbed by the thin film at a given wavelength, the absorption spectroscopy was conducted, and the basic schematic of it is shown in Figure 2.7. In this thesis, the Cary 5000 UV-Vis-NIR spectrophotometer (Agilent technologies) was used.

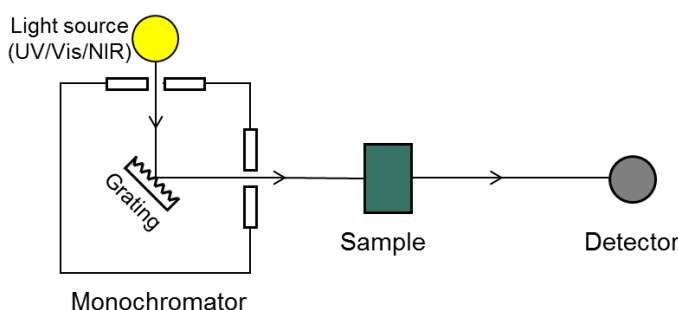


**Figure 2.7** Schematic of an UV-Vis spectrophotometer.

**X-ray photoelectron spectroscopy (XPS):** XPS is the most widely used surface analysis technique for measuring quantitative elemental composition or chemical states. As shown in Figure 2.8, XPS typically consists of monochromatic aluminum K-alpha X-rays, which excite a surface of samples, causing photoelectrons to be emitted from the surface. An analyzer to measure the kinetic energy of electron is used, quantifying the energy of the ejected photoelectrons. Then, the experimental quantity and chemical states can be determined from the results of binding energy

and intensity of a photoelectron peak. In this thesis, XPS measurements were performed using an Axis-HSi (Kratos Analytical), shown in Figure 2.8b, with a monochromated Al anode in order to investigate surface elements before and after light-induced degradation in *Chapter 4*.

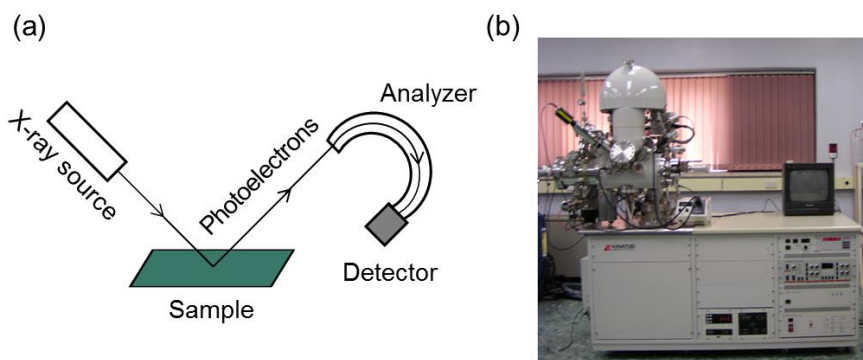


**Figure 2.8** (a) Schematic diagram of XPS. (b) XPS machine in Research Institute of Advanced Materials (RIAM) at Seoul National University.

**Ultraviolet photoelectron spectroscopy (UPS):** UPS is also a part of photoelectron spectroscopy like XPS, which measures kinetic energy of photoelectrons emitted by molecules. The difference from XPS is its exciting source of vacuum UV radiation rather than X-rays. As a source of radiation, He is frequently used, which emits energy of 21.2 eV. The HOMO (highest occupied molecular orbital) or VBM (valence band maximum) of the sample can be experimentally obtained using the following equation through the UPS measurement.

$$HOMO \text{ (or VBM)} = h\nu - |E_{\text{cutoff}} - E_{\text{onset}}| \quad (2.8)$$

In this thesis, UPS measurements were conducted using an Axis Ultra DLD (Kratos Analytical) with He I (21.2 eV) photon source and a hemispherical analyzer to measure the VBM of CdSe tetrapod nanocrystals in *Chapter 3*.

## 2.4.2 Atomic Force Microscopy Technique

Atomic force microscopy (AFM) is a powerful technique to obtain local surface information from samples at nanometer-scale resolution. Conductive AFM (c-AFM), in particular, is a type of AFM in which a bias voltage is applied between conductive cantilever and surface of sample, measuring the flowing current between the two as shown in Figure 2.9. Using c-AFM, topography and current conductivity data over the sample surface can be acquired at the same time. In this thesis, topographic and c-AFM images of active layer were obtained using Park XE-100 AFM with platinum-coated cantilevers PPP-ContPt (Nanosensors) in contact mode, when  $-4$  V was applied from ITO substrate to the conductive tip through both ZnO NPs and active layer. The resulting values were inverted so that the higher current represents toward plus direction.

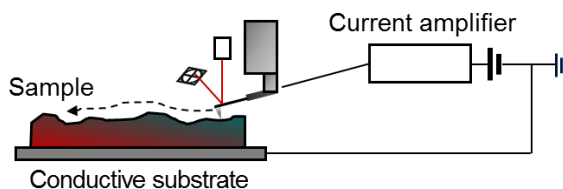


**Figure 2.9** Schematic of a conductive AFM measurement.

### 2.4.3 Other Thin Film Characterization Methods

**Scanning electron microscopy (SEM):** SEM is a technique to gain information about topography and composition of samples' surface with a resolution of a few tens of nanometers. It scans a focused electron beam over the sample to produce images. In *Chapter 3* of this thesis, surface morphology of ZnO:In/CdSe TP film was obtained using SEM (JEOL JSM-6701F).

**Transmission electron microscopy (TEM):** TEM also uses high energy of focused electron beam like SEM technique, but the difference from it is that images are produced from the interaction of the electrons which transmitted directly through the sample; therefore, TEM offers higher resolution than SEM. In *Chapter 3* of this thesis, cross-sectional image of solar cells were taken using focused-ion beam equipment (FEI Nova 600 Nanolab) for sample preparation and TEM (JEOL JEM-2100F) measurement.

## **2.5 Device Characterization Methods**

### **2.5.1 Current Density–Voltage Characteristics Measurement**

The characterization of current density-voltage ( $J$ - $V$ ) curve is basic method to experimentally evaluate the performance of solar cells (as mentioned in Chapter 2.1.2). In this thesis,  $J$ - $V$  characteristics were measured with a source measurement unit (Keithley SMU237), and the performances of the devices were characterized under AM1.5G solar spectrum at 1 sun ( $100 \text{ mW cm}^{-2}$ ) illumination, simulated by Newport 91160A. To study the light intensity dependence of solar cell devices, the incident light intensity was adjusted using neutral density filters from  $1 \text{ mW cm}^{-2}$  to  $100 \text{ mW cm}^{-2}$ . For temperature dependent  $J$ - $V$  measurements, closed-cycle cryostat with a temperature controller (Lake Shore Cryotronics, model 331) was used.

### **2.5.2 Incident Photon-to-electron Conversion Efficiency Measurement**

IPCE (incident photon-to-current conversion efficiency) measurement is used to know how efficiently the solar cell devices convert incident light into electricity at a given photon energy. The measurement is based on illuminating the sample by a monochromatic light which came through the xenon lamp and monochromator as shown in Figure 2.10. By extracting electrical signal (number of generated carriers) from the sample varying the wavelength of the light, IPCE curve as a function of wavelength can be obtained. Therefore, the integrated value of IPCE data is same as the current density generated from the solar cell. In this thesis, IPCE spectra of devices were acquired using an Oriel IQE 200 model, which composed of xenon lamp, lock-in amplifier, order-sorting filter wheel, chopper, and monochromator.

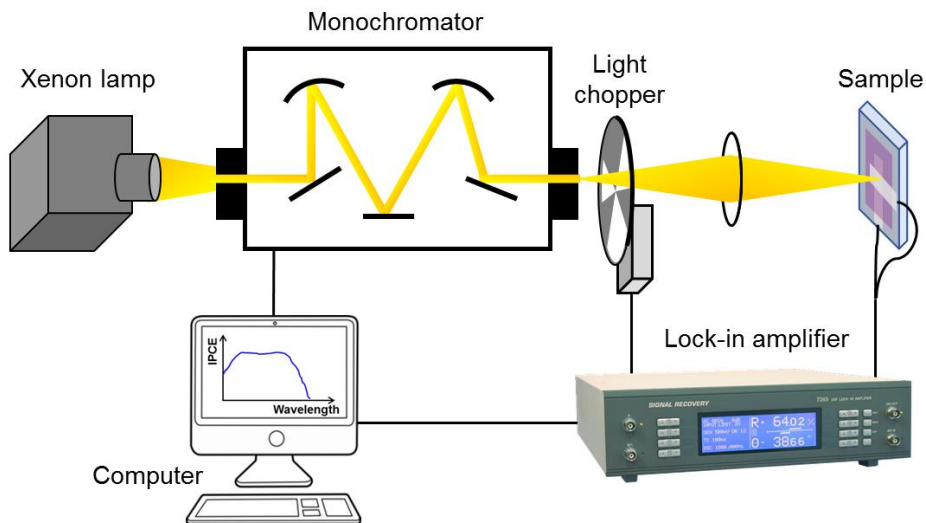


**Figure 2.10** Schematic diagram of IPCE measurement.

### 2.5.3 Light Intensity Dependence Characteristics

Light intensity dependence of  $J$ - $V$  characteristics can provide carrier recombination and collection properties of solar cells.[63-67] First of all, the incident light dependence of  $J_{SC}$  follows a power law relationship, which is given by

$$J_{SC} \propto P_{light}^{\alpha} \quad (2.9)$$

where,  $\alpha$  is the exponent. When the exponent value  $\alpha$  closes to 1, then extraction of charge carriers is faster than recombination, so that recombination mechanism is dominated by monomolecular recombination, while it closes to 0.5 if bimolecular recombination is dominant due to comparable processes between charge extraction and recombination.

In addition, the values of  $V_{OC}$  as a function of light intensity are able to be considered to determine the additional recombination mechanism of trap-assisted recombination, which is a Shockley-Read-Hall (SRH) recombination. In this case, a

slope of thermal voltage ( $kT/q$ ) features the strength of the recombination: the higher slope correlates with the more charge recombination losses.

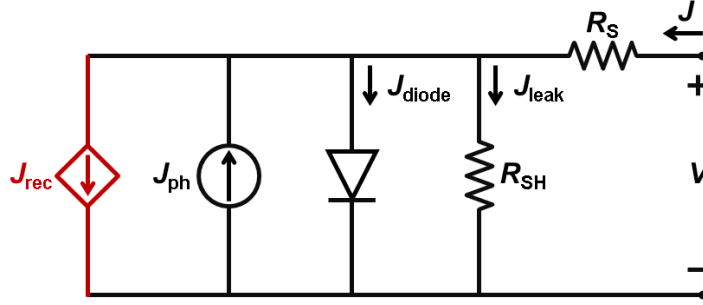


**Figure 2.11** The equivalent circuit diagram of solar cell with additional recombination loss term ( $J_{rec}$ ).

To obtain further investigation into the collection properties of solar cells, collection voltage ( $V_C$ ) can also be analyzed. For an equivalent circuit of solar cells, the additional recombination loss term of  $J_{rec}$  has been introduced as shown in Figure 2.11, since a significant recombination occurs within the active layer of the solar cells consisting of disordered materials, such as amorphous silicon or organic materials. Hence, Equation (2.7) is now modified by considering the  $J_{rec}$  term as follows:

$$J = J_0 \left[ \exp \left[ \frac{q}{nkT} (V - JR_S) \right] - 1 \right] + \frac{V - JR_S}{R_{SH}} - J_{ph} + J_{rec} \quad (2.10)$$

As shown in Figure 2.12, collection voltages ( $V_C$ ) can be defined by a crossing point of all linear fits for the  $J$ - $V$  curves at short circuit condition, which are measured at various light intensities.

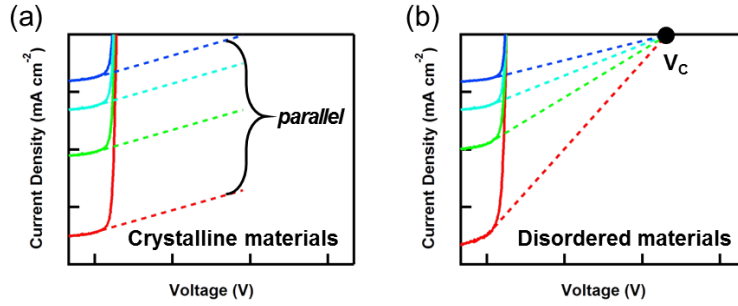


**Figure 2.12** Schematic diagram of the theoretical behavior of incident light intensity dependent  $J$ - $V$  characteristics for (a) crystalline materials-based solar cells and (b) solar cells with disordered materials. Figure modified from [68].

Voz *et al.*[67] recently derived expressions for calculating carrier collection efficiency in polymer solar cells under the three assumptions, which are constant electric field, drift-driven collection, and monomolecular recombination. Under these assumptions, the collection efficiency of photogenerated charge carriers at short circuit condition ( $\eta_{c0}$ ), short circuit resistance ( $R_{SC}$ , reciprocal slopes of the  $J$ - $V$  curve at  $V=0$ , i.e.,  $V_c = R_{SC} J_{SC}$ ), which reflects the recombination term ( $J_{rec}$ ) under the various light intensities, and  $V_c$  can be expressed as follows:

$$\eta_{c0} = 1 - \frac{L/2}{l_{c0}} \quad (2.11)$$

$$R_{SC} = \left( \frac{l_{c0}}{L/2} - 1 \right) \frac{V_{bi}}{J_{SC}} \quad (2.12)$$

$$V_c = \left( \frac{l_{c0}}{L/2} - 1 \right) V_{bi} \quad (2.13)$$

with

$$l_{c0} = \mu \tau_{eff} \frac{V_{bi}}{L} \quad (2.14)$$



where  $l_{CO}$  is the collection length at short circuit condition,  $L$  is a thickness of the active layer,  $\mu\tau_{eff}$  is the effective  $\mu\tau$  product, i.e.,  $\mu\tau_{eff} = \mu_n\tau_n + \mu_p\tau_p$ , and  $V_{bi}$  is the built-in potential, which refers to the voltage at which  $J_{ph}$  is zero, where  $J_{ph}$  is determined as subtracting measured current density in the dark from the measured current density under illumination.[65] The collection length denotes the maximum distance of dissociated electrons and holes driven by the electric field before recombination.

#### 2.5.4 Impedance Spectroscopy

Impedance spectroscopy is an analytical tool to obtain more information about electrodynamic processes in solar cells.[69, 70] It measures both resistive and reactive components simultaneously as a function of frequency, therefore the frequency response of the system can be revealed. Nyquist (or Cole-Cole) plot, which is called when real part of impedance spectra is plotted on the X-axis and the imaginary part on the Y-axis, is the most popular format for evaluating the interface and bulk characteristics of the devices. An example of Nyquist plot of organic solar cell, which structure is ITO/ZnO NPs/PTB7:PC<sub>71</sub>BM/MoO<sub>x</sub>/Ag, is shown in Figure 2.13a.

For an equivalent circuit model of organic solar cells, circuit with a series of one resistance and three parallel RC elements (Figure 2.13b) was applied in this thesis, where  $R_C$  is contact resistance and three RC circuits represent bottom interface, bulk heterojunction, and top interface. By fitting the impedance spectra with proper equivalent circuit model and by assigning RC components to appropriate films (layers), then further analysis using extracted resistance and capacitance values can be carried out.

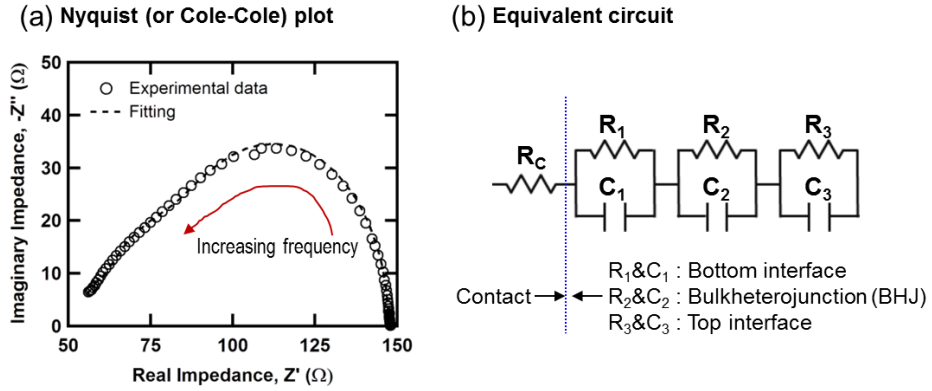


**Figure 2.13** (a) Nyquist plot and (b) equivalent circuit of organic solar cells. The open circles in (a) are experimental data and the dotted line is the fitted line of impedance spectrum using an equivalent circuit of (b).

The impedance and its real ( $Z'$ ) and imaginary ( $-Z''$ ) part of the equivalent circuit in Figure 2.13b is given as follows:

$$\begin{aligned}
 Z &= R_c + \frac{R_1}{1 + j\omega R_1 C_1} + \frac{R_2}{1 + j\omega R_2 C_2} + \frac{R_3}{1 + j\omega R_3 C_3} \\
 &= R_c + \frac{R_1 - j\omega R_1^2 C_1}{1 + \omega^2 R_1^2 C_1^2} + \frac{R_2 - j\omega R_2^2 C_2}{1 + \omega^2 R_2^2 C_2^2} + \frac{R_3 - j\omega R_3^2 C_3}{1 + \omega^2 R_3^2 C_3^2}
 \end{aligned} \tag{2.15}$$

$$\begin{aligned}
 \therefore Z' &= R_c + \frac{R_1}{1 + \omega^2 R_1^2 C_1^2} + \frac{R_2}{1 + \omega^2 R_2^2 C_2^2} + \frac{R_3}{1 + \omega^2 R_3^2 C_3^2} \\
 -Z'' &= \frac{\omega R_1^2 C_1}{1 + \omega^2 R_1^2 C_1^2} + \frac{\omega R_2^2 C_2}{1 + \omega^2 R_2^2 C_2^2} + \frac{\omega R_3^2 C_3}{1 + \omega^2 R_3^2 C_3^2}
 \end{aligned} \tag{2.16}$$

In this thesis, the AC impedance measurements for solar cell devices were performed by an impedance analyzer (Wayne Kerr Electronics, 6550B) for a frequency range from 1 kHz to 50 MHz with an AC drive bias of 15 mV. The impedance spectroscopy data were fitted using MEISP and ZView software with an equivalent circuit of solar cells.

### 2.5.5 Transient Photocurrent Measurement

Transient photocurrent is a measurement technique to study about time-dependent extraction of charge carriers generated by light (usually laser). Therefore, it can be conducted in solar cells to get information about photocurrent decay dynamics including charge recombination or density of states.[71, 72] In this thesis, transient photoconductivity measurements were performed by excitation of PTB7:PC<sub>71</sub>BM solar cells with a Nd:YAG pulsed laser (pulse duration  $\sim 5$  ns,  $\lambda = 590$  nm), then the resulting photocurrent decay signals were recorded on a digital oscilloscope (Tektronix, TDS5054B), which are all shown in Figure 2.14.

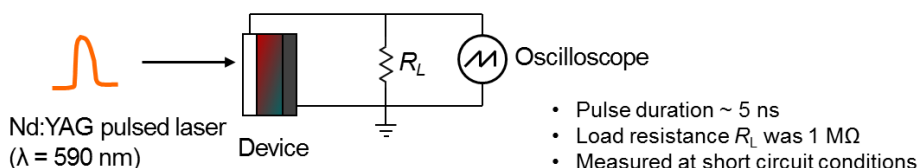


**Figure 2.14** Schematic diagram of transient photoconductivity measurement. Nd:YAG pulsed laser (pulse duration  $\sim 5$  ns,  $\lambda = 590$  nm) was used as an excitation source, and load resistance  $R_L$  was  $1\text{ M}\Omega$ .

### 2.5.6 Space Charge Limited Current Measurement

Space-charge-limited current (SCLC) measurement is one of the most widely used techniques for determining charge carrier mobility in organic devices. To measure the SCLC, the typical device structure is sandwiched organic semiconductor layer between two metal electrodes that make ohmic contact on one side, so that, only single carrier (hole-only or electron-only) can transport.

In the low voltage region, current varies linearly with the voltage, which shows free carrier conduction following Ohm's law. However, at higher voltage above  $V_{\text{SCLC}}$ , current presents a quadratic dependence on the voltage ( $J \propto V^2$ ), indicating space charge formation in photoactive layer.[73] Considering the field-dependent mobility,[74] the  $J$ - $V$  characteristics thus can be modeled as follows:[74, 75]

$$J = \frac{9}{8} \varepsilon_0 \varepsilon_r \mu_0 \exp(\beta \sqrt{F}) \frac{V^2}{d^3} \quad (2.17)$$

where  $\varepsilon_0$  and  $\varepsilon_r$  represent the permittivity of free space and relative dielectric constant, respectively,  $\mu_0$  is the zero-field mobility,  $\beta$  is the Pool-Frenkel (PF) coefficient,  $F$  is the applied electric field, and  $d$  is the thickness of active layer. Using the Equation (2.17), charge carrier mobility can be extracted from this space-charge-limited region.

On the other hand, when traps are involved, current can follow a power law behavior on the voltage ( $J \propto V^{l+1}$ ), where the exponent  $l$  is given by trap energy  $E_t = kT$  depending on the temperature. The  $J$ - $V$  characteristics of trap-charge-limited current (TCLC) conduction model are given as: [76, 77]

$$J = q^{1-l} \mu N_v \left( \frac{2l+1}{l+1} \right)^{l+1} \left( \frac{\varepsilon_0 \varepsilon_r}{N_t} \frac{l}{l+1} \right)^l \frac{V^{l+1}}{d^{2l+1}} \quad (2.18)$$

where  $N_t$  is the trap density and  $N_v$  is the effective density of states.

### 2.5.7 Light-induced Aging Conditions

For light-induced aging process of solar cells in **Chapter 4**, the samples were continuously illuminated under AM1.5G 1 sun condition for 24 h using solar cell reliability test system (K3600, McScience). A Xenon lamp was used as a light source and its light intensity was adjusted to  $100 \text{ mW cm}^{-2}$  using a calibrated Si

reference cell. Temperature had been maintained at 25 °C with cooling system during the light-induced process, and the current-voltage curves were measured at every 15 min. The device structure prepared for this experiment and image of solar cell reliability test system are shown in Figure 2.15.

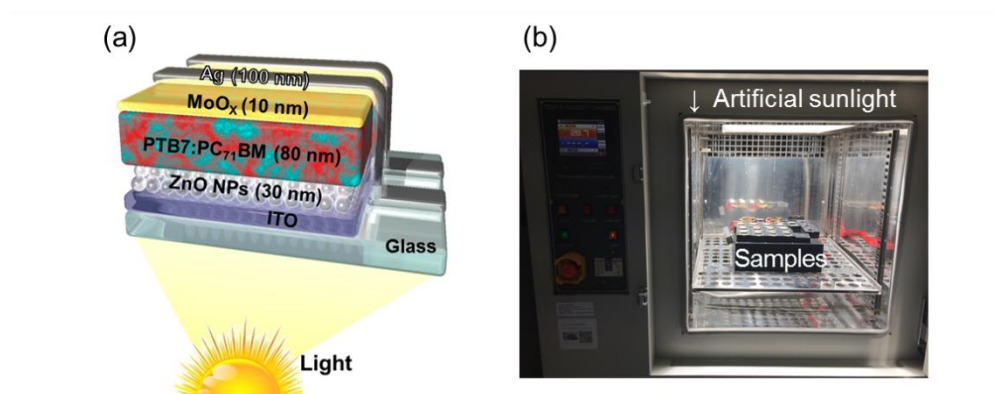


**Figure 2.15** (a) Device structure of inverted organic solar cells prepared for light-induced degradation experiments. (b) Solar cell reliability test system in Center for Multiscale Energy System at Seoul National University.

## **Chapter 3**

# **Efficiency Improvement of Inverted Organic Solar Cells by Using CdSe Tetrapod as an Electron-selective Interlayer**

### **3.1 Introduction**

In terms of device configuration in organic solar cells, an inverted structure, the electrons are collected by the bottom electrode – indium tin oxide (ITO), and holes are collected by the top electrode, has been steadily investigated.[78-81] Compared to conventional structure, inverted-type devices have potential for better long-term ambient stability by preventing the use of hygroscopic and acidic poly(3,4-ethylenedioxythiophene): poly(styrenesulfonate) (PEDOT:PSS) as hole transport

layer, and by employing high work function metal for top electrode. One of the key factors in performance of inverted-type devices is the *n*-type buffer layer. This electron buffer layer should meet good optical transparency, electron transport and extraction characteristics with suitable energy band positions.

To collect photogenerated electrons efficiently from the active layer to cathode, the metal oxides thin films (e.g. SnO<sub>2</sub>, TiO<sub>2</sub>, and ZnO)[30-32] have been the most widely used as *n*-type buffer layers due to its properties of easy process, optical transparency, and good electrical performance. Furthermore, there have been efforts to make these metal oxides nanostructured, such as nanowires-, rods-, or wrinkles-shaped, to enhance the power conversion efficiency (PCE) of solar cells.[40, 41, 82, 83] Due to their increased interfacial area and more continuous path for carrier transport,[40] short circuit current and overall performance of solar cells increased. However, in order to control the growth of these aligned metal oxides nanostructures, photolithography[84, 85] or nanoimprint-soft lithography[41] was employed; both techniques are complicated fabrication methods using photoresist and exposure process. Therefore, it will be beneficial to find an easy-processable nanostructured interlayer regarding time and cost savings.

Here a unique electron-selective interlayer comprising of In-doped ZnO (ZnO:In) and vertically-aligned CdSe tetrapods (TPs) for polymer:fullerene bulkheterojunction (BHJ) solar cells is introduced. Using highly monodisperse CdSe TPs with tailored dimension for BHJ layer thickness, vertically electron transport channels are easily assembled on the ZnO:In buffer layer by simple spin-coating process. In addition to good exciton dissociation properties of typical BHJ network with extensive interfaces, this CdSe TP nanostructures are able to offer direct and efficient pathways for photogenerated electrons from the active layer to ZnO:In buffer layer by penetrating the disordered BHJ domains.

### 3.2 Device Configuration of PTB7:PC<sub>71</sub>BM Solar Cells with CdSe Tetrapods

The organization of the solar cells with organic active layer and inorganic charge extraction nanostructure is illustrated in Figure 3.1a. The vertically-standing CdSe TPs were deposited on plane ZnO:In buffer layer/ITO cathode substrates. This nanostructure is assembled with poly[[4,8-bis[(2-ethylhexyl)oxy]benzo[1,2-b:4,5-b']dithiophene-2,6-diyl][3-fluoro-2-[(2-ethylhexyl)carbonyl]thieno[3,4-b]thiophenediyl]] (PTB7):[6,6]-phenyl-C71-butyric acid methyl ester (PC<sub>71</sub>BM) BHJ, and a molybdenum oxide (MoO<sub>x</sub>) and an aluminum (Al) were evaporated as an anode.

In this study, the colloidal CdSe TP nanocrystals were chosen because of their excellent electron mobility (bulk Hall electron mobility  $\sim 900 \text{ cm}^2 \text{ V}^{-1} \text{ s}^{-1}$ ), [86] appropriate energy levels (conduction band  $\sim 4 \text{ eV}$ , Figure 3.1b), and structural uniqueness. A detailed explanation for energy level of CdSe TP nanocrystals will be given in the Chapter 3.2.2. These excellent electrical properties allow the electrons to be rapidly transferred from PC<sub>71</sub>BM (lowest unoccupied molecular orbital  $\sim 4 \text{ eV}$ ) to CdSe TPs and moved to the ZnO:In buffer layer. Therefore, the CdSe TPs are intended to amplify electron transport from PC<sub>71</sub>BM domains to the ITO cathode.

At the same time, the tetrapod morphology is the simplest architecture which can stably stand on a substrate owing to its low center of mass, so that vertically-oriented inorganic channels can be easily produced by simple deposition of CdSe TPs on the substrate.



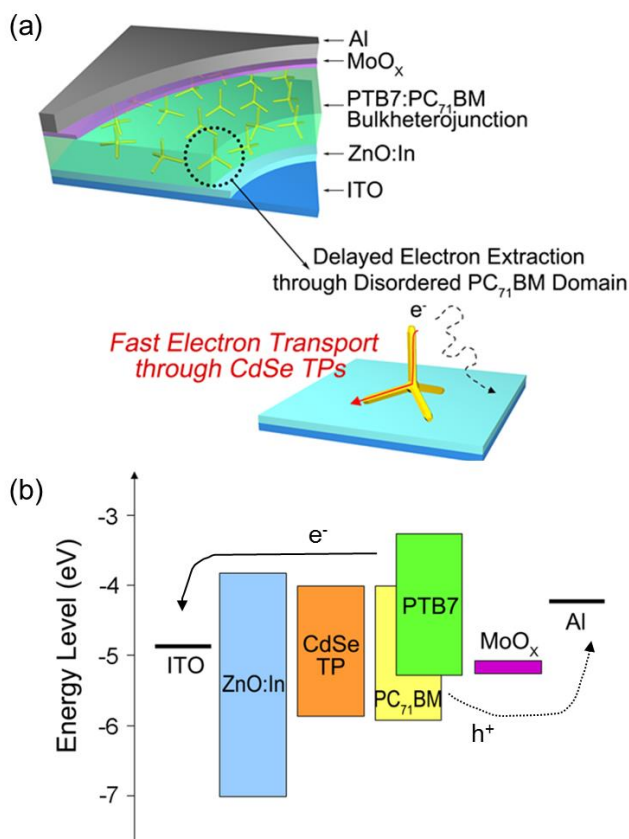


**Figure 3.1** (a) Schematic illustration of a PTB7:PC<sub>71</sub>BM solar cell with the CdSe TP charge extraction nanostructure. The detailed role of CdSe TPs is illustrated below; CdSe TPs can extract photogenerated electrons in PC<sub>71</sub>BM domain by providing vertical transport pathway through their arms. (b) An energy level diagram of PTB7:PC<sub>71</sub>BM solar cells with CdSe TPs.

### 3.2.1 Tailored CdSe Tetrapods for Organic Solar Cells

In this study, morphologically-uniform CdSe TPs (shape selectivity > 90% and a deviation in arm length ~ 3 nm) were synthesized with ~ 57 nm of theoretical height via the continuous precursor injection (CPI) method (Figure 3.2a).[62] The dimension of CdSe TPs was precisely decided by the thickness of PTB7:PC<sub>71</sub>BM BHJ active layer varying from 70 nm to 100 nm. As shown in Figure 3.3, *J-V* curve for solar cell with 98 nm-arm lengths of CdSe TPs show no diode characteristics and high leakage current. That indicates taller CdSe TPs can possibly perforate the active layer and form an undesired contact with a MoO<sub>x</sub>/Al layer. From a transmission electron microscopy (TEM) of CdSe TPs representing the orthographic projection image of CdSe TP arms, it is possible to calculate the theoretical arm length (~ 52 nm) and 3-dimensional height (~ 57 nm) of CdSe TPs based on Pythagorean Theorem (Figure 3.2a).

Using the length-controlled CdSe TPs, the CdSe TPs were easily fabricated by spin-coating of solution and following thermal treatment. As shown in Figure 3.2b, CdSe TPs spun on the ZnO:In substrate formed a scattered morphology with vertically-oriented arms (displaying as white dots). Besides, the heat treatment has a role in stratifying mechanical robustness of the CdSe TPs against following surface treatment and a formation of PTB7:PC<sub>71</sub>BM BHJ.[47] It was confirmed that the morphology of CdSe TPs was preserved during ligand elimination (by repeating ethanol washing), surface passivation (with 1-hexylamine), and a formation of PTB7:PC<sub>71</sub>BM active layer (Figure 3.4). Note that high concentration (> 3 mg mL<sup>-1</sup>) of CdSe TP solution resulted in an entangled and directionless CdSe TP morphology, which is attributed to the capillary force between CdSe TPs during solvent drying (Figure 3.2c).

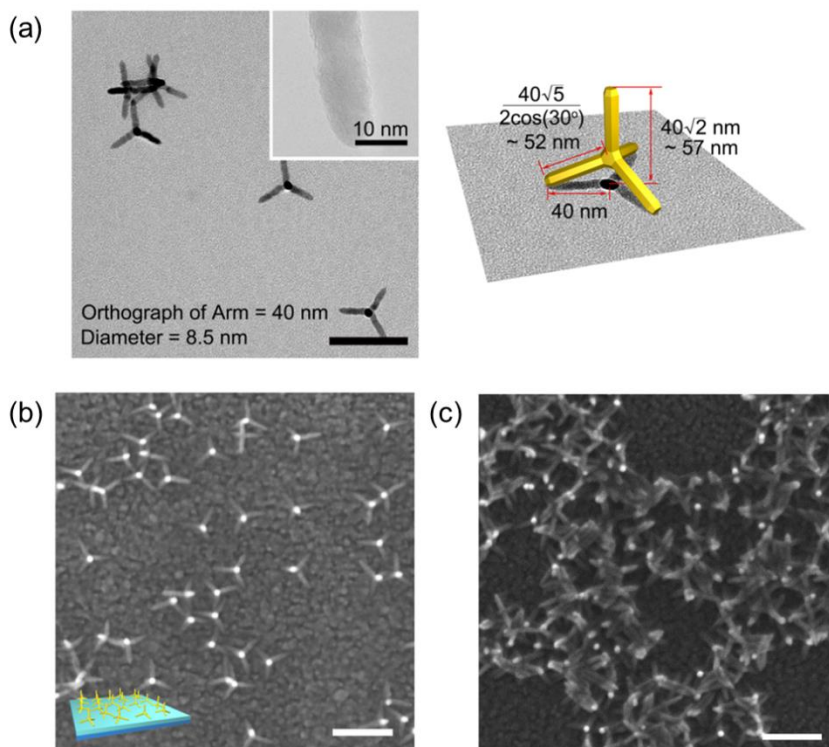


**Figure 3.2** (a) A transmission electron microscopy (TEM) image of CdSe TPs tailored for a PTB7:PC<sub>71</sub>BM BHJ layer. Detailed dimensions of vertically-standing CdSe TPs are illustrated on the right. A top scanning electron microscopy (SEM) image of the charge extraction nanostructure fabricated with (b) 0.5 mg mL<sup>-1</sup> and (c) 4 mg mL<sup>-1</sup> of CdSe TP solution on top of ZnO:In layer. All scale bars are 100 nm.

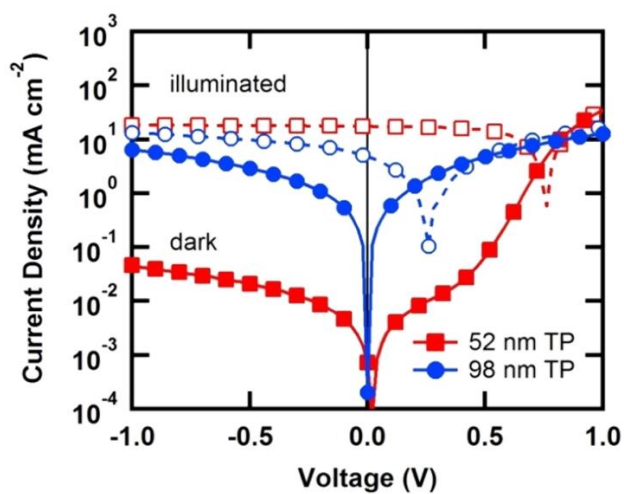


**Figure 3.3** *J-V* characteristics of PTB7:PC<sub>71</sub>BM solar cell having different arm lengths of CdSe TPs (52 nm and 98 nm) under the dark (filled symbol) and illuminated (open symbol) conditions.

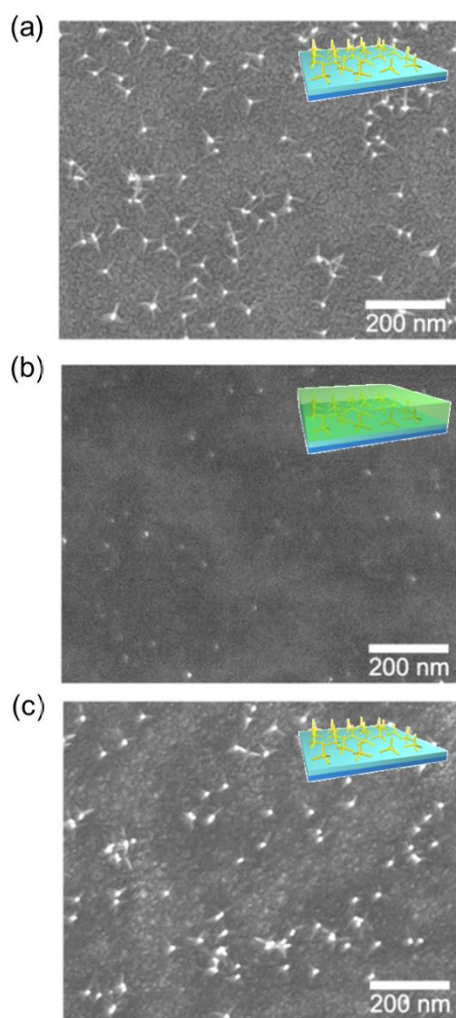


**Figure 3.4** Top SEM images of (a) CdSe TP film before coating a PTB7:PC<sub>71</sub>BM layer, (b) spin-coated active layer film on top of CdSe TPs, and (c) recovered CdSe TP film by eliminating active layer with chloroform washing.

As shown in Figure 3.5a, it is clearly shown that the CdSe TP arms perpendicular to the ZnO:In substrate are well included in the uniform PTB7:PC<sub>71</sub>BM active layer. Meanwhile, the overall height of CdSe TPs was estimated as ~ 50 nm, slightly lower than the theoretical value. It is supposed to originate from the deviation in the arm length of CdSe TPs and the surface roughness of ZnO:In substrates (RMS roughness ~ 1 nm). Energy dispersive X-ray spectroscopy (EDS) analysis in Figure 3.5b-c also supports that CdSe TPs are vertically aligned and are surrounded by S atoms (from PTB7 layer).

### 3.2.2 Energy Level of CdSe Tetrapods – UPS Analysis

In order to define the energy level of CdSe TPs, UV photoelectron spectroscopy (UPS) measurement was performed. Figure 3.6a shows the high binding energy cutoff region and the valence band region in UPS spectra for different concentration of CdSe TPs (0, 0.5, 1, and 2 mg mL<sup>-1</sup>), which was formed on top of a bare ZnO:In film. By using Equation (2.8), HOMO (highest occupied molecular orbital) or VBM (valence band maximum) of ZnO:In and CdSe TPs films can be determined. The resulting values are 6.98 eV, 6.34 eV, 5.8 eV, and 5.62 eV for a bare ZnO:In film, 0.5 mg mL<sup>-1</sup>, 1 mg mL<sup>-1</sup>, and 2 mg mL<sup>-1</sup> of CdSe TPs, respectively. Considering 0.5 mg mL<sup>-1</sup> of CdSe TPs solution is hard to completely cover the ZnO:In underlayer as shown in Figure 3.2b, VBM of CdSe TP nanocrystals can be calculated to approximately 5.6 ~ 5.8 eV. Therefore, conduction band minimum (CBM) value of CdSe TPs is around 3.8 ~ 4.0 eV by using the first exciton peak of CdSe TPs, which is 1.8 eV, estimated from the absorption measurement (shown in the right panel of Figure 3.6b).

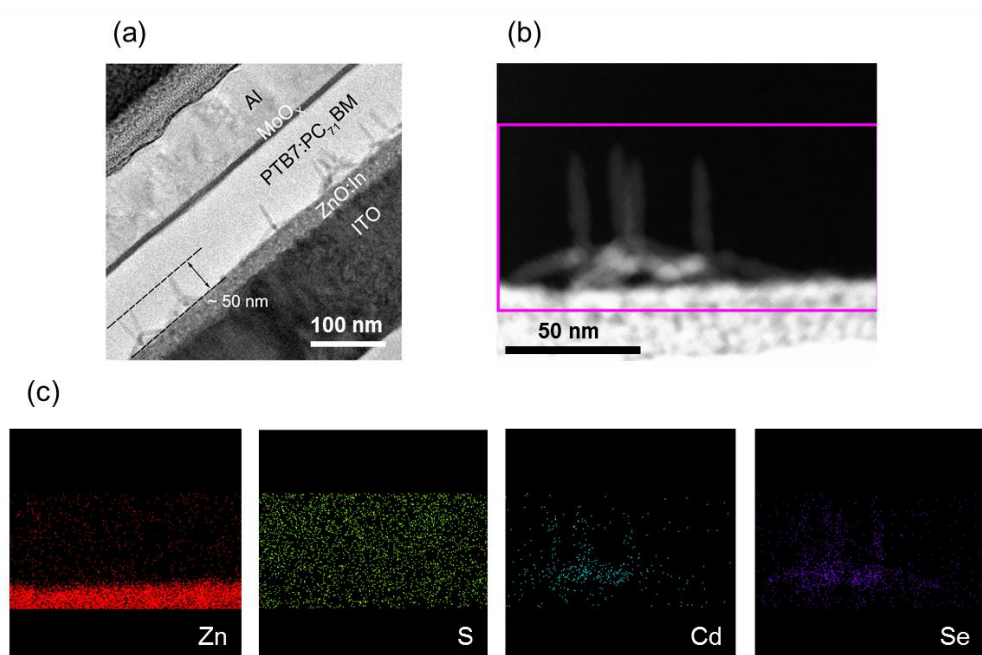


**Figure 3.5** (a) A cross-sectional TEM image of the PTB7:PC<sub>71</sub>BM solar cell with CdSe TPs. (b) A dark field cross-sectional TEM image of the solar cell device with CdSe TPs and energy dispersive X-ray spectroscopy (EDS) mapping: (c) Zinc (from a ZnO:In layer), Sulfur (from PTB7), Cadmium, and Selenium (from CdSe TPs).

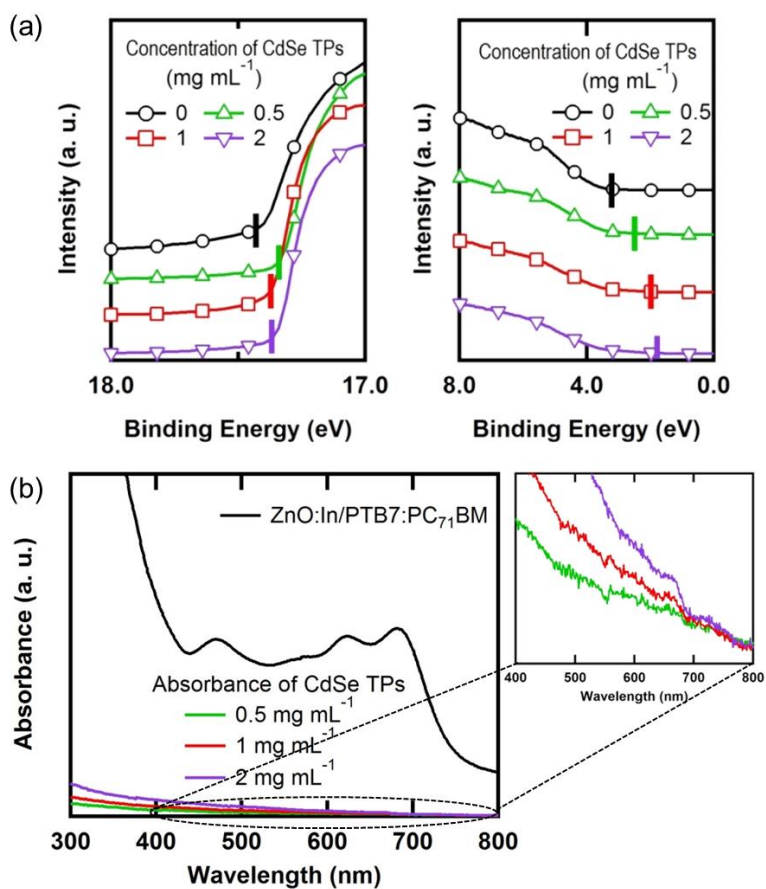


**Figure 3.6** (a) High binding energy cutoff and valence band region in UPS spectra of a bare ZnO:In film and films with CdSe TPs. (b) UV-Vis absorption spectrum of PTB7:PC<sub>71</sub>BM and spectra of CdSe TPs with different concentration on top of ZnO:In film. Enlarged graph for absorption edge of CdSe TPs is shown in the right side of panel b.



### 3.3 Performance of PTB7:PC<sub>71</sub>BM Solar Cells with CdSe Tetrapods

It has been examined that CdSe TPs are the appropriate candidate for electron-selective interlayer, having advantages of easy fabrication process and excellent electrical properties with suitable energy band positions.

Before investigating the actual device performance of PTB7:PC<sub>71</sub>BM solar cells with CdSe TPs interlayer, the numbers of CdSe TPs within the small area of 0.12  $\mu\text{m}^2$  were counted through the SEM images, to quantify those of CdSe nanocrystals deposited on the ZnO:In film as shown in Figure 3.7. The estimated number of CdSe TPs per unit surface area ( $\mu\text{m}^2$ ) is 150, 250, and 350 when the concentration of CdSe TPs is 0.5, 1, and 2  $\text{mg mL}^{-1}$ , respectively. This estimate is quite reasonable when the number of CdSe TPs with low magnification SEM image was also counted (not shown here), because most tetrapods show well-distributed morphology in micrometer scale with proper fabrication condition (e.g., 0.5  $\text{mg mL}^{-1}$ ).

#### 3.3.1 Solar Cell Device Characteristics

Figure 3.8a shows the current density versus voltage ( $J$ - $V$ ) characteristics of solar cell devices without and with 250  $\mu\text{m}^{-2}$  of CdSe TPs under the 1 sun illumination, and the results deduced from  $J$ - $V$  curves are summarized in Table 3.1 together with the 150  $\mu\text{m}^{-2}$  and 350  $\mu\text{m}^{-2}$  concentration of CdSe TPs. The device performance gradually improved when CdSe TPs were applied more as electron extraction interlayer as shown in Figure 3.8c and d, and the optimum device was achieved when 250  $\mu\text{m}^{-2}$  of CdSe TP solution was used.

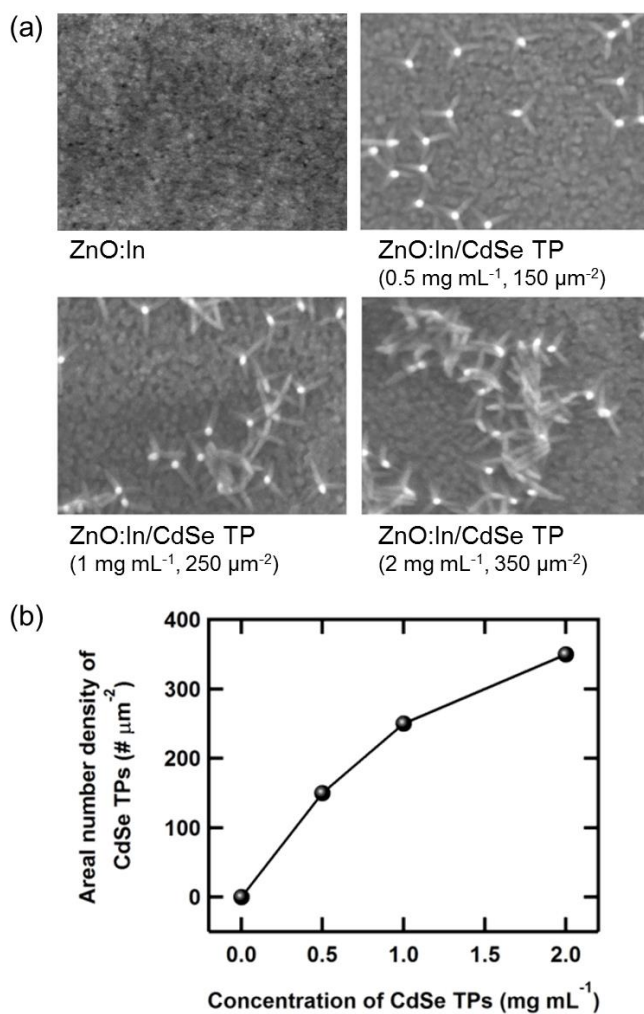


**Figure 3.7** (a) A top SEM images of CdSe TPs with different concentration (0, 0.5, 1, and 2 mg mL<sup>-1</sup>). At higher concentration, CdSe TPs are getting aggregated, forming TP clusters. All image sizes are 400 nm × 300 nm. (b) Relationship between the areal number density (#/μm<sup>2</sup>) and the concentration of CdSe TPs. The number of TPs within the area of 0.12 μm<sup>2</sup> was counted through the SEM images to estimate the areal number density.

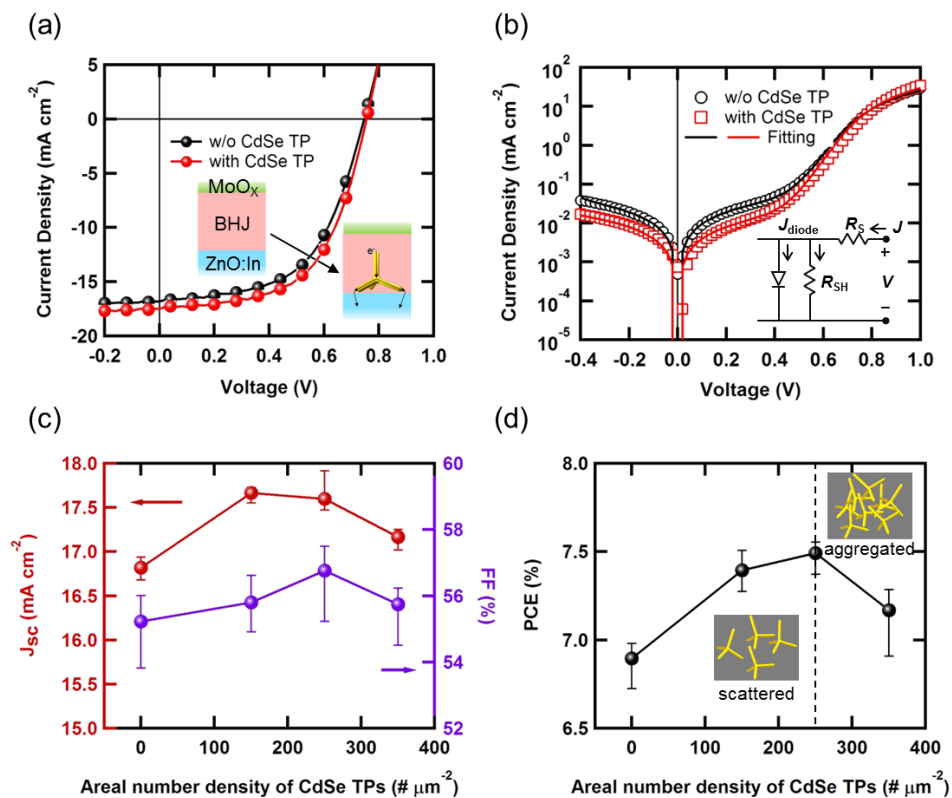


**Figure 3.8** Current density ( $J$ ) - voltage ( $V$ ) characteristics of the PTB7:PC<sub>71</sub>BM solar cells without and with the 250  $\mu\text{m}^{-2}$  of CdSe TPs, measured under the (a) AM1.5G 1 sun illumination and (b) dark condition. (c) Short circuit current density ( $J_{sc}$ ), fill factor (FF), and (d) power conversion efficiency (PCE) as a function of the areal number density of CdSe TPs. The inset of (b) shows the equivalent circuit diagram for solar cells. Dark current fitting is done using this solar cell equivalent circuit model.

**Table 3.1** Performance parameters of inverted PTB7:PC<sub>71</sub>BM solar cells without and with different concentration of nanostructured CdSe TPs under AM 1.5G 1sun illumination.<sup>a</sup>

	$J_{SC}$ (mA cm <sup>-2</sup> )	$V_{OC}$ (V)	FF (%)	PCE (%)	$R_s$ ( $\Omega$ cm <sup>2</sup> )	$R_{SH}$ ( $\Omega$ cm <sup>2</sup> )
w/o CdSe TPs	16.82±0.11 (16.80)	0.74±0.01 (0.75)	55.22±0.85 (55.70)	6.90±0.10 (6.98)	8.30	532.34
w/ CdSe TPs (150/ $\mu$ m <sup>2</sup> )	17.67±0.08 (17.67)	0.75±0.01 (0.75)	55.81±0.71 (56.62)	7.39±0.12 (7.51)	7.08	451.71
w/ CdSe TPs (250/ $\mu$ m <sup>2</sup> )	17.46±0.04 (17.48)	0.75±0.01 (0.75)	56.30±2.11 (57.26)	7.41±0.27 (7.55)	6.70	539.14
w/ CdSe TPs (350/ $\mu$ m <sup>2</sup> )	17.17±0.10 (17.25)	0.75±0.01 (0.75)	55.74±0.83 (56.07)	7.17±0.18 (7.28)	6.87	544.25

<sup>a</sup> The average and standard deviation values are for samples at least 4 devices on the same substrate. The values in brackets represent the photovoltaic parameters obtained for the best-performing cell.

Device containing  $250\ \mu\text{m}^{-2}$  of nanostructured CdSe TPs showed the improved short circuit current density ( $J_{\text{SC}}$ ) and fill factor (FF) from  $16.80\ \text{mA cm}^{-2}$  and 55.70 % to  $17.48\ \text{mA cm}^{-2}$  and 57.26 %, respectively, while an open circuit voltage ( $V_{\text{OC}}$ ) remains as same as the device without CdSe TP. Hence, the power conversion efficiency (PCE) increases from 6.98 % to 7.55 %. The CdSe TPs in this device absorbs some part of the UV-visible light as shown in Figure 3.6b, however, this is negligible compared to the absorption of PTB7:PC<sub>71</sub>BM, so that almost the whole absorption takes place in active layer.

As further increase of the areal number density of CdSe TPs to  $350\ \mu\text{m}^{-2}$ , device performance decreased. One possible reason is that the aggregated TP clusters with high concentration of CdSe TPs form voids, leading the reduction of the interfacial area between CdSe TPs and BHJ layer. Furthermore, the additional photogenerated charges from the high concentration of CdSe TPs may recombine before delivering the holes to polymer molecules due to its limited surface area with donor molecules. Therefore, the increased  $J_{\text{SC}}$  in the device with CdSe TPs is more attributed to the better charge transport of electrons, which are generated and dissociated in active layer, rather than the photogenerated electrons in CdSe TPs itself.

The IPCE spectrum for the device with CdSe TP in Figure 3.9a shows enhanced broad wavelength range of spectral response (300-800 nm). On the other hand, as shown in Figure 3.9b, there is only small increase in absorbance from CdSe TPs at short wavelength region. Thus, it clearly proves that the improvement in the  $J_{\text{SC}}$  for the device with CdSe TP interlayer originates from the better charge extraction characteristics. Note that all the devices with CdSe TPs, which concentration is up to  $350\ \mu\text{m}^{-2}$ , showed improved performances compared to the device without CdSe TP interlayer.

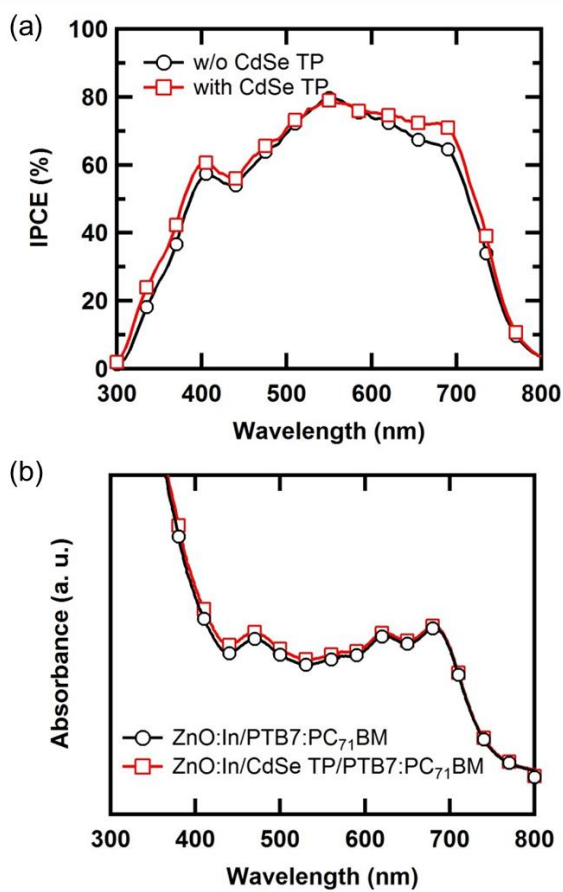


**Figure 3.9** (a) IPCE spectra of PTB7:PC<sub>71</sub>BM solar cells without and with CdSe TPs. (b) UV-Vis absorption spectra of PTB7:PC<sub>71</sub>BM films without and with the CdSe TP layer.

In order to investigate the effect of CdSe TPs ( $250 \mu\text{m}^2$ ) nanostructure into the electrical properties of the interface more systematically, the diode characteristics in the dark were studied. The dark  $J$ - $V$  curves of the solar cells without and with CdSe TPs are shown in Figure 3.8b, and equivalent circuit model is shown in inset of Figure 3.8b. (mentioned in detail in Chapter 2.1.3 and Chapter 2.5.3)

With no illumination ( $J_{\text{ph}} = J_{\text{rec}} = 0$ ), the current density-voltage characteristics of Equation (2.10) can be expressed as

$$J = J_0 \left[ \exp \left[ \frac{q}{nkT} (V - JR_s) \right] - 1 \right] + \frac{V - JR_s}{R_{\text{SH}}} \quad (3.1)$$

In addition, with in the regime where diode characteristics are dominant, i.e.,  $\exp[q(V-JR_s)/nkT] \gg 1$ , then the current density-voltage relationship is given as follows:[87]

$$\ln \left( J - \frac{V - JR_s}{R_{\text{SH}}} \right) = \ln J_0 + \frac{q}{nkT} (V - JR_s) \quad (3.2)$$

where,  $J_0$  and  $n$  represent the reverse saturation current density and diode ideality factor, respectively,  $q$  is the elementary charge,  $k$  is the Boltzmann constant,  $T$  is the absolute temperature,  $R_s$  is the series resistance, and  $R_{\text{SH}}$  is the shunt resistance.

The parameters of  $J_0$  and  $n$  can be evaluated from the y-intercept and the slope of the line, respectively. The solid lines in Figure 3.8b show the fitted results, while circles and triangles represent the measured values of dark current density, and the set of parameters extracted from these are summarized in Table 3.2.

With vertically aligned nanostructure of CdSe TPs in solar cell device, the reverse saturation current density and series resistance decreased, and the shunt resistance increased, as well as the diode ideality factor was closer to 1. The lower reverse saturation current density in the device with CdSe TPs means that diffusion

**Table 3.2** Fitted parameters calculated from the dark curve of PTB7:PC<sub>71</sub>BM solar cells without and with nanostructured CdSe TPs.

	$J_0$ (nA cm <sup>-2</sup> )	$n$	$R_s$ ( $\Omega$ cm <sup>2</sup> )	$R_{SH}$ (k $\Omega$ cm <sup>2</sup> )
w/o CdSe TP	1.68	1.82	8.55	10.54
w/ CdSe TPs (250/ $\mu$ m <sup>2</sup> )	1.03	1.79	6.83	25.28



of minority carriers, which are holes in our case, is smaller. At the same time, current is higher at the positive voltage around 1V, and therefore CdSe TPs can work as electron-selective layer both transporting electrons and blocking holes. The two times higher value of shunt resistance for the device with CdSe TPs also implies that the leakage current is effectively suppressed by the CdSe TPs layer.[88]

The diode ideality factor  $n$  is known as reflecting the properties of the internal BHJ morphology,[89] recombination loss or disorder in the electronic states.[90, 91] The  $n$  value of the device having CdSe TPs is closer to 1, and it can be interpreted as decrease of the interfacial recombination with the introduced CdSe TPs. The characteristics of recombination and charge collection for the devices without and with CdSe TPs will be discussed in a subsequent chapter.

To sum up these  $J$ - $V$  curve under the illumination and dark diode characteristics, we conclude that CdSe TPs with ZnO:In layer work as nanostructured electron-selective layer, which can extract electrons well from the disordered PC<sub>71</sub>BM domain to the cathode through their vertically-aligned inorganic domains, resulting in improved  $J_{SC}$  and FF.

### 3.3.2 Recombination and Charge Collection Characteristics

To explore the effects of CdSe TPs on carrier recombination and collection characteristics, we determined the light intensity dependence of  $J_{SC}$  and  $V_{OC}$ , and collection voltages ( $V_C$ ) of the solar cell devices without and with CdSe TPs. Note that the detailed characterization methods used here were discussed in Chapter 2.5.3.

First of all, Figure 3.10a shows the log-log plot of incident light dependence of  $J_{SC}$  of the devices, and the  $J_{SC}$  values change linearly along the light intensity for the both, yielding the power law of 0.894 for the device without CdSe TPs and 0.914 for the one with CdSe TPs. When the exponent value closes to 1, then extraction of charge carriers is faster than recombination, so that recombination mechanism is dominated by monomolecular recombination, while it closes to 0.5 if bimolecular recombination is dominant due to comparable processes between charge extraction and recombination.[63, 64] Therefore, the higher value for the device with CdSe TPs means that bimolecular recombination losses are more suppressed than the device without CdSe TPs.

Secondly, the values of  $V_{OC}$  as a function of light intensity were measured to determine the additional recombination mechanism of trap-assisted recombination, which is a Shockley-Read-Hall (SRH) recombination, as shown in Figure 3.10b. A slope of thermal voltage ( $kT/q$ ) features the strength of the recombination: the higher slope correlates with the more charge recombination losses.[65, 66] The linear slope of  $V_{OC}-\log(P_{light})$  is  $1.36 kT/q$  for a solar cell without CdSe TPs, whereas  $1.29 kT/q$  for a cell with CdSe TPs, implying that the device with CdSe TPs has less trap-assisted recombination loss, and fewer trap states than the one without CdSe TPs.

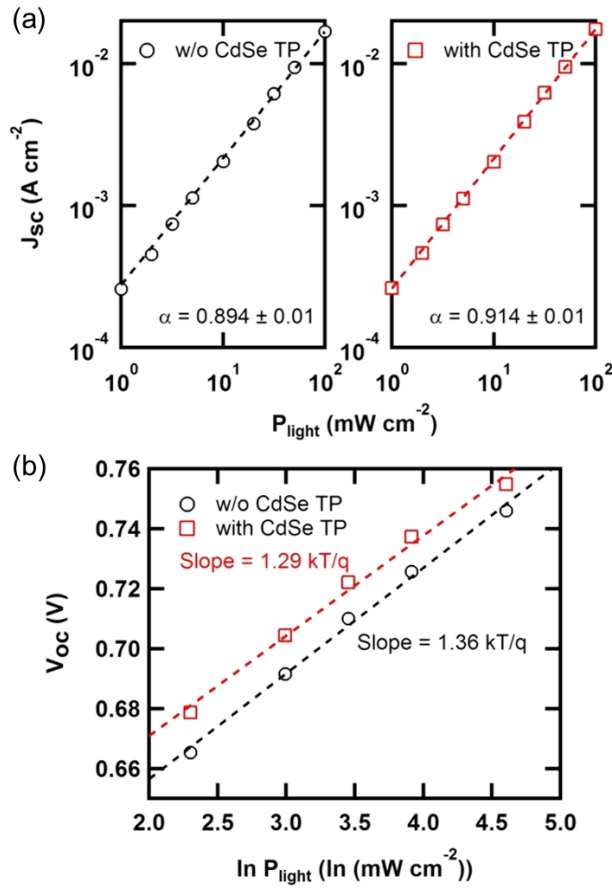


**Figure 3.10** (a) Light intensity dependence of short circuit current density ( $J_{sc}$ ) for cells without and with CdSe TPs. Dotted lines show fitting curves using a power law. (b) Open circuit voltage ( $V_{oc}$ ) of cells without and with CdSe TPs as a function of light intensity, together with linear fits.

To obtain further investigation into the collection properties of solar cells depending on the existence of CdSe TPs, we lastly analyzed the collection voltage ( $V_C$ ). As shown in Figure 3.11, collection voltages ( $V_C$ ) can be defined by a crossing point of all linear fits for the  $J$ - $V$  curves, which were measured at various light intensity (5-100 mW cm<sup>-2</sup>), at short circuit condition. We can calculate the collection efficiency at short circuit condition ( $\eta_{C0}$ ) and effective  $\mu\tau$  product ( $\mu\tau_{eff}$ ) from the  $V_C$ .

Under the three assumptions of constant electric field, drift-driven collection, and monomolecular recombination,  $V_C$  can be defined to calculate carrier collection efficiency ( $\eta_C$ ). [67] An equivalent circuit of solar cells is shown in Figure 2.11, and under the above assumptions, the collection efficiency of photogenerated charge carriers at short circuit condition ( $\eta_{C0}$ ), short circuit resistance ( $R_{SC}$ , reciprocal slopes of the  $J$ - $V$  curve at  $V=0$ , i.e.,  $V_C = R_{SC} J_{SC}$ ), which reflects the recombination term ( $J_{rec}$ ) under the various light intensities, and  $V_C$  can be expressed as follows:

$$\eta_{C0} = 1 - \frac{L/2}{l_{C0}} \quad (2.11)$$

$$R_{SC} = \left( \frac{l_{C0}}{L/2} - 1 \right) \frac{V_{bi}}{J_{SC}} \quad (2.12)$$

$$V_C = \left( \frac{l_{C0}}{L/2} - 1 \right) V_{bi} \quad (2.13)$$

with

$$l_{C0} = \mu\tau_{eff} \frac{V_{bi}}{L} \quad (2.14)$$

where  $l_{C0}$  is the collection length at short circuit condition,  $L$  is a thickness of the active layer,  $\mu\tau_{eff}$  is the effective  $\mu\tau$  product, i.e.,  $\mu\tau_{eff} = \mu_n\tau_n + \mu_p\tau_p$ , and  $V_{bi}$  is the built-in potential, which refers to the voltage at which  $J_{ph}$  is zero, where  $J_{ph}$  is determined as subtracting measured current density in the dark from the measured

current density under illumination. The collection length denotes the maximum distance of dissociated electrons and holes driven by the electric field before recombination. The detailed derivations of formulas are given in the reference quoted above.

The resulting values of  $V_C$  are 5.86 V and 6.94 V for the device without CdSe TPs and with CdSe TPs, respectively, as shown in the insets of Figure 3.11. According to the Equation (2.11) and Equation (2.13) with an active layer thickness of 90 nm, the  $\eta_{CO}$  increases from 85.4 % to 88.3 % by inserting nanostructured CdSe TPs between ZnO:In and active layer. The corresponding  $\mu\tau_{eff}$  product using an Equation (2.14) is  $2.8 \times 10^{-10} \text{ cm}^2 \text{ V}^{-1}$  for the cell without CdSe TPs, whereas  $3.8 \times 10^{-10} \text{ cm}^2 \text{ V}^{-1}$  for the cell with CdSe TPs. All extracted parameters including  $V_C$ ,  $I_{CO}$ ,  $\eta_{CO}$ , and  $\mu\tau_{eff}$  are summarized in Table 3.3. These calculated parameters indicate that CdSe TPs provide the better charge transport and extraction characteristics through their vertically-aligned arms, which straight connect the active layer to buffer layer, and in the end to the electrode.

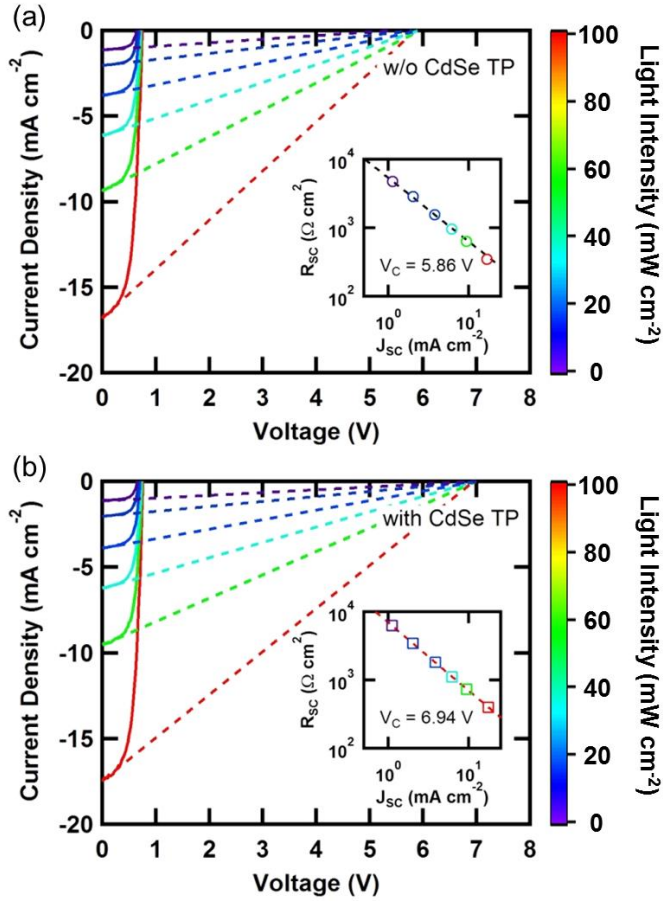


**Figure 3.11**  $J$ - $V$  characteristics of cells without and with CdSe TPs measured at various incident light intensity ( $5\text{-}100 \text{ mW cm}^{-2}$ ). Collection voltages ( $V_C$ ) are defined by the intersection of all linear fits at short circuit condition. The insets of (a) and (b) show  $R_{\text{sc}}$  extracted around  $V = 0$ , and calculated  $V_C$  from the relation of  $V_C = R_{\text{sc}}J_{\text{sc}}$ .

**Table 3.3** Calculated parameters of collection voltage ( $V_c$ ), collection length ( $l_{c0}$ ) and collection efficiency ( $\eta_{c0}$ ) at short circuit condition, and effective  $\mu\tau$  product ( $\mu\tau_{eff}$ ) for solar cell devices without and with CdSe TPs.

	$V_c$ (V)	$l_{c0}$ (cm)	$\eta_{c0}$ (%)	$\mu\tau_{eff}$ (cm V <sup>-1</sup> )
w/o CdSe TP	5.86	$3.09 \times 10^{-5}$	85.4	$2.78 \times 10^{-10}$
w/ CdSe TPs (250/ $\mu\text{m}^2$ )	6.94	$3.84 \times 10^{-5}$	88.3	$3.76 \times 10^{-10}$

### 3.4 Summary

In summary, the roles of CdSe TPs as an electron-selective interlayer on the performance of inverted organic solar cells were studied. By providing the direct inorganic path from the disordered bulkheterojunction domain to electron buffer layer, CdSe TPs layer can effectively extract photogenerated charge carriers, leading to the improvement of both  $J_{SC}$  and FF of the solar cell devices. It was demonstrated that CdSe TPs reduce the interfacial traps between the BHJ layer and buffer layer, reduce the recombination losses, improve the hole-blocking properties as well as electron-transporting, and therefore improve charge collection. Consequently, the power conversion efficiency of PTB7:PC<sub>71</sub>BM based solar cell with nanostructured CdSe TPs increases to 7.55%. Furthermore, the use of length-controlled inorganic nanocrystals as an interlayer is expected to be a general platform for improving charge extraction in thin film solar cells.



## Chapter 4

# Understanding of Light-induced Degradation Mechanisms of Inverted Organic Solar Cells

### 4.1 Introduction

The efficiency growths in the field of organic solar cells are making progress toward their commercial practicality with a big advantage of low-cost manufacturability, emphasizing the importance of stability issues at the same time. Thus, interest has been raised in understanding degradation mechanisms inside the solar cells. Among the main factors which are known to degrade organic devices (as mentioned in Chapter 1.2.2), *light* is the most crucial one because not only is it an intrinsic reaction, but the sunlight is also known to accelerate other degradation processes.[49,

50] Furthermore, since the solar cells operate under the illumination with high photon flux, it is necessary to systematically study about photo-induced degradation mechanism of the organic solar cells.

The loss mechanisms of organic solar cells caused by light mostly have been studied in well-known poly(3-hexylthiophene) (P3HT)-based solar cells.[17, 54, 55, 57, 58] Studies of light-induced degradation in P3HT:[6,6]-phenyl-C61-butyric acid methyl ester (PC<sub>60</sub>BM) solar cells have revealed that morphological change,[54] photo-oxidation of PC<sub>60</sub>BM,[55] electrical deterioration,[57] and interface degradation [58] are the main results of continuous light irradiation by using various measurement techniques. Moreover, light-induced degradation of organic solar cells is speculated to have material-specific properties as well. Heumueller et al. reported that crystalline polymers show less photo-induced burn-in voltage loss than amorphous materials.[92] Despite the polymer-dependent characteristics of degradation effects, the researches in terms of stability issues or degradation mechanisms have been limited for recently developed polymers, which are realizing high PCE these days. Therefore, it is required to explore the light-induced degradation mechanisms for high performance polymer-based solar devices.

Here the investigation of light-induced degradation for poly[[4,8-bis[(2-ethylhexyl)oxy]benzo-[1,2-b:4,5-b']dithiophene-2,6-diyl][3-fluoro-2-[(2-ethylhexyl)-carbonyl]thieno[3,4-b]thiophenediyl]] (PTB7):[6,6]-phenyl-C71-butyric acid methyl ester (PC<sub>71</sub>BM) BHJ solar cells was done in the first 24 hours under the AM 1.5G 1 sun continuous illumination. To minimize the extrinsic factors, devices were encapsulated and temperature was maintained at 25 °C during the light-aging process. By comparing the fresh and 24 h-aged device using both morphological and electrical measurement techniques, it was possible to gain a better understanding of light-induced degradation mechanism for PTB7-based solar cells.

## 4.2 Degradation Trend of Inverted PTB7:PC<sub>71</sub>BM Solar Cells

In order to observe the light-induced degradation trend of PTB7:PC<sub>71</sub>BM solar cells during the continuous illumination of 24 h, devices were fabricated using an inverted structure with a configuration of ITO/ZnO NPs/PTB7:PC<sub>71</sub>BM/MoO<sub>x</sub>/Ag. This device architecture, which uses metal oxides thin films as electron extraction layer, was adopted due to better stability than conventional structure not by using hygroscopic and acidic poly(3,4-ethylenedioxythiophene):poly-(styrenesulfonate) (PEDOT:PSS) as bottom charge extraction layer right above the ITO.[32, 93] Encapsulated devices were then tested for light-induced aging under the 1 sun illumination with controlled temperature of 25 °C.

Current density-voltage (*J-V*) characteristics of fresh and 24 h-aged devices are shown in Figure 4.1a, and the variation of normalized solar cell parameters as a function of aging time is shown in Figure 4.1b-e. The parameter values deduced from *J-V* curves are summarized in Table 4.1. The device performance gradually degraded within 24 h of light-induced aging, and was shown to be mainly due to drop of both short circuit current density ( $J_{SC}$ , 11 % drop) and fill factor (FF, 20 % drop), while an open circuit voltage ( $V_{OC}$ ) dropped to less than 3 %. Note that bias effect from the *J-V* measurement at every 15 min is negligible by comparing with the degradation trend of the device exposed only in light (not shown here). To gain further insight into the photo-induced degradation process inside the devices, which resulted in approximately 30 % of power conversion efficiency (PCE) loss after 24 h, a systematic investigation was performed on the film characteristics of photoactive layer and electrical properties of devices.

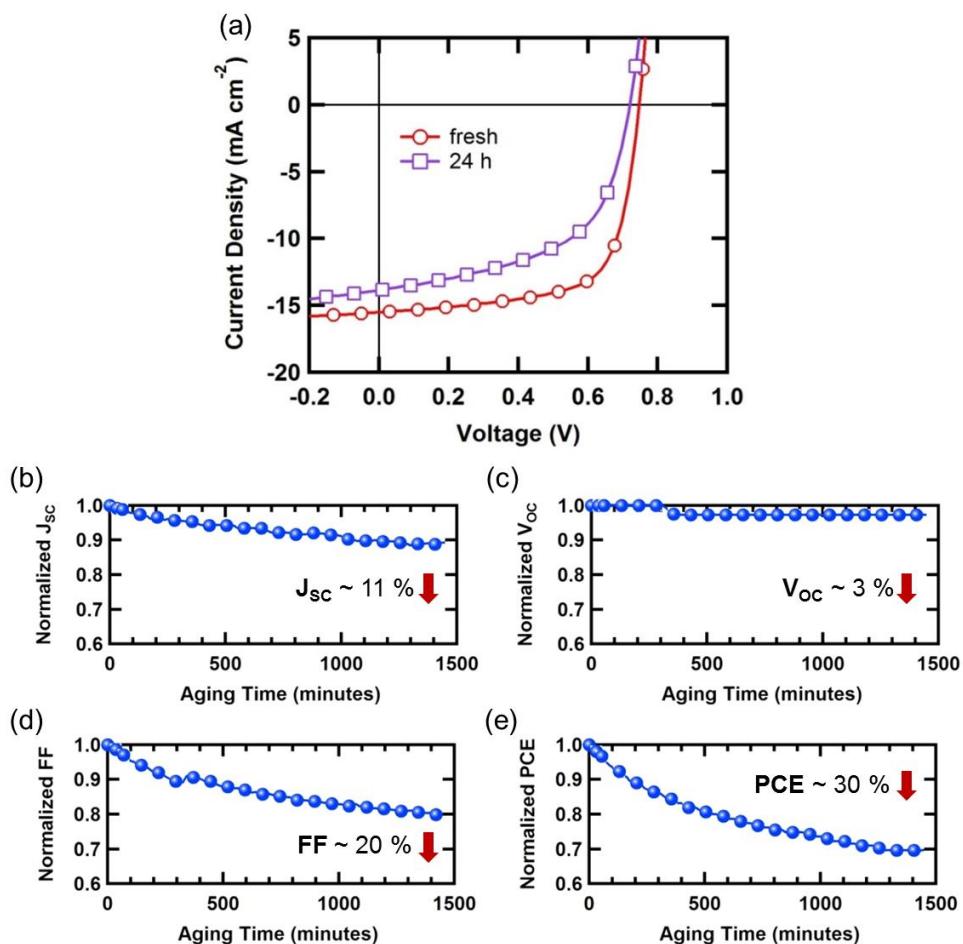


**Figure 4.1** (a) Current density–voltage ( $J$ – $V$ ) characteristics of PTB7:PC<sub>71</sub>BM solar cell before and after light-induced aging for 24 h of continuous illumination, and detailed variation of normalized performance parameters of (b)  $J_{sc}$ , (c)  $V_{oc}$ , (d) FF, and (e) PCE with respect to the illumination time.

**Table 4.1** Characteristics of PTB7:PC<sub>71</sub>BM solar cell devices before and after 24 h of the light-induced aging.  $J_{SC}$ ,  $V_{OC}$ , FF, and PCE were measured under the 1 sun illumination condition, and fitted parameters of  $J_0$ ,  $n$ ,  $R_S$ , and  $R_{SH}$  were calculated from the dark  $J$ - $V$  curve in Figure 4.6a.

	fresh	24 h-aged
$J_{SC}$ (mA cm <sup>-2</sup> )	15.50	13.84
$V_{OC}$ (V)	0.74	0.72
FF (%)	69.27	55.35
PCE (%)	7.91	5.51
$J_0$ (A cm <sup>-2</sup> )	$3.32 \times 10^{-12}$	$4.56 \times 10^{-10}$
$n$	1.35	1.78
$R_S$ ( $\Omega$ cm <sup>2</sup> )	1.42	1.76
$R_{SH}$ (k $\Omega$ cm <sup>2</sup> )	122.19	15.00

## 4.2.1 Degradation in Optical Properties

The optical microscope images and absorption spectra for fresh and 24 h-aged PTB7:PC<sub>71</sub>BM films, formed on top of ZnO NPs layer, are shown in Figure 4.2 and Figure 4.3, respectively. The photoactive layer shows no detectable change in both optical images and absorbance after the 24 h of light exposure, indicating that PTB7:PC<sub>71</sub>BM film itself remains quite stable within relatively short aging time of 24 h. It was reported that exposed in ambient conditions can decrease intensity of absorption much faster by chemical modification of polymers.[21] To clarify the surface characteristics of active layer, AFM topography images and XPS spectra were measured as shown in Figure 4.4a-b and Figure 4.5, respectively. Both measurements reveal that there are negligible differences in surface composition, chemical bonding states, and surface roughness (1.029 nm for fresh, 1.046 nm for aged) between the fresh and 24 h-aged PTB7:PC<sub>71</sub>BM films. Note that by virtue of encapsulation, the atomic concentration of O 1s has been kept almost same values of 7.64–7.9 % during the photo-induced aging. While the optical, structural, and morphological information of active layer has not been changed for 24 h of light-aging process, solar cell device performance was degraded quite rapidly as shown in Figure 4.1. It can be interpreted as consequences caused by electrical degradation rather than the chemical change of PTB7:PC<sub>71</sub>BM, so conductive-AFM (c-AFM) was also performed to probe conductance imaging of active layer as shown in Figure 4.4c-d. The average current on a measured area of 9  $\mu\text{m}^2$  decreased from 174.9 pA to 150.0 pA, when the film was aged under the continuous illumination.

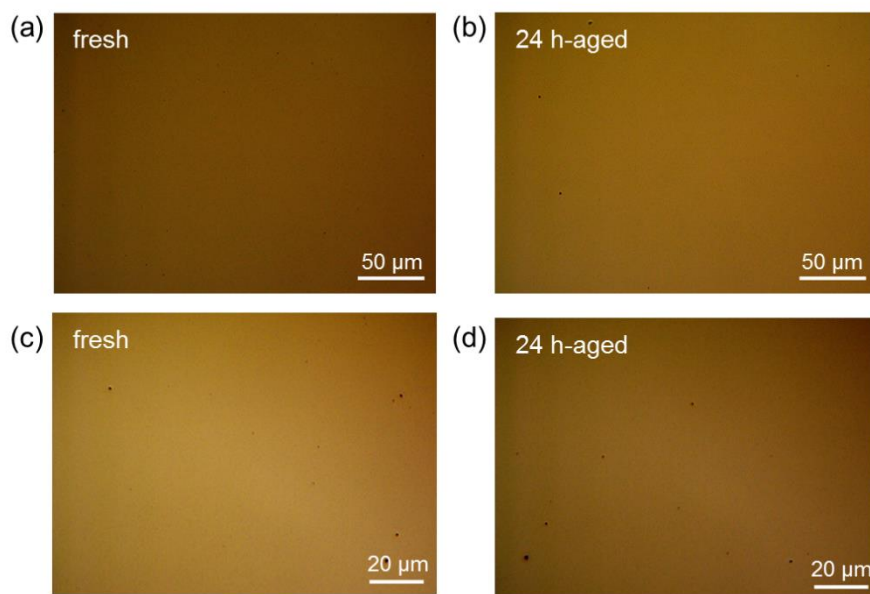


**Figure 4.2** Optical microscope images of PTB7:PC<sub>71</sub>BM films (a and c) before and (b and d) after light-induced aging process with magnifications of (a and b) 50X and (c and d) 100X.

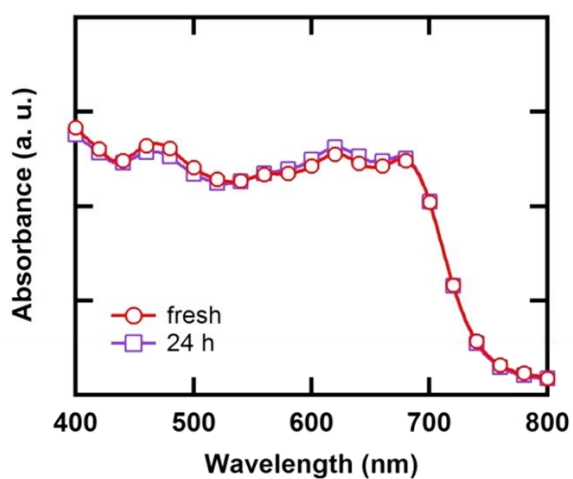


**Figure 4.3** UV-Vis absorption spectra of PTB7:PC<sub>71</sub>BM films, deposited on top of ZnO nanoparticles, before and after light-induced aging for 24 h of continuous illumination.



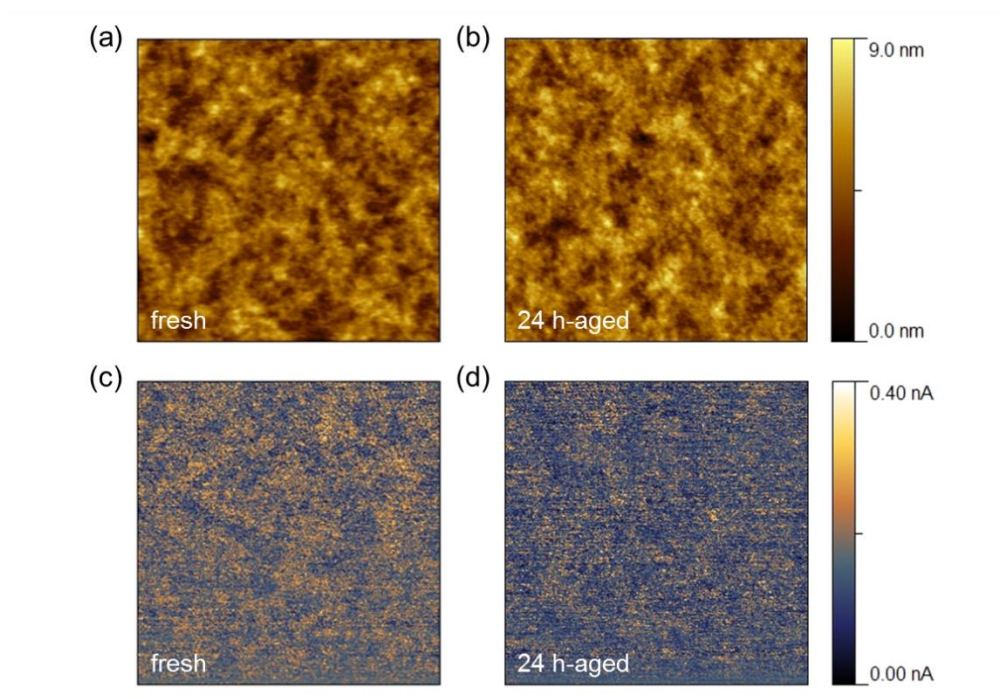


**Figure 4.4** (a and b) Topographic and (c and d) conductive AFM images of PTB7:PC<sub>71</sub>BM films before and after 24 h of continuous illumination. The height and current images were taken at the same time within the same area, and all images are  $3 \times 3 \mu\text{m}^2$ .

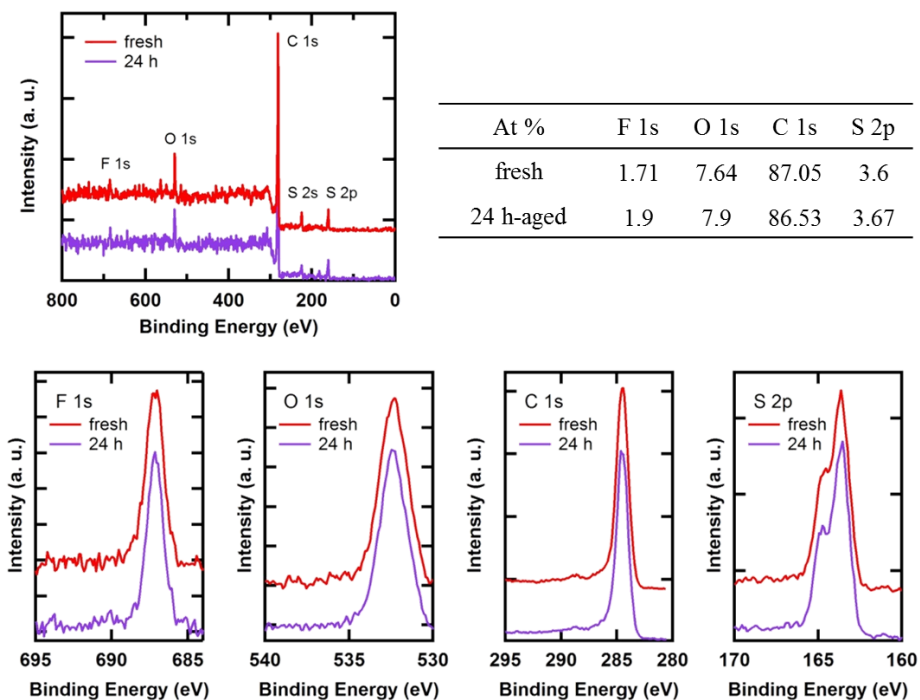


**Figure 4.5** The wide XPS spectra and high resolution spectra of F 1s, O 1s, C 1s, and S 2p for PTB7:PC<sub>71</sub>BM active layer before and after 24 h of light-induced aging. The quantified results of surface atomic concentrations are shown in the inset table.

## 4.2.2 Degradation in Electrical Properties

To investigate the light-induced degradation effects on the electrical properties more systematically, techniques including dark diode characteristics and IPCE were studied. First of all, the dark  $J$ - $V$  curves of solar cells before and after aging are shown in Figure 4.6a. It is clear that leakage current at reverse bias increased, and current at positive voltage around 1 V decreased in aged device, which probably leads to lower shunt resistance and larger series resistance, respectively, resulting in lower FF.

The dark  $J$ - $V$  characteristics can also be more analyzed using a solar cell equivalent circuit model, which is shown in the inset of Figure 4.6a. (mentioned in detail in Chapter 3.3.1 ) Using an Equation (3.2), diode characteristics including  $J_0$ ,  $n$ ,  $R_s$ , and  $R_{sh}$  are able to be estimated, and the parameters are summarized in Table 4.1. The dotted lines in Figure 4.6a show the calculated  $J$ - $V$  curve using these evaluated parameters.

Figure 4.6b shows IPCE curves, which are directly correlated to  $J_{sc}$  by a combination of optical absorption and electrical properties. It is notable that light-induced  $J_{sc}$  loss for the aged device originates from the decline of extraction characteristics by comparing Figure 4.3 with Figure 4.6b. Although the absorbance of PTB7:PC<sub>71</sub>BM remained unchanged during the 24 h of continuous light, the IPCE decreased in a broad wavelength range from 360 nm to 800 nm, which should be explained by the electrical degradation.

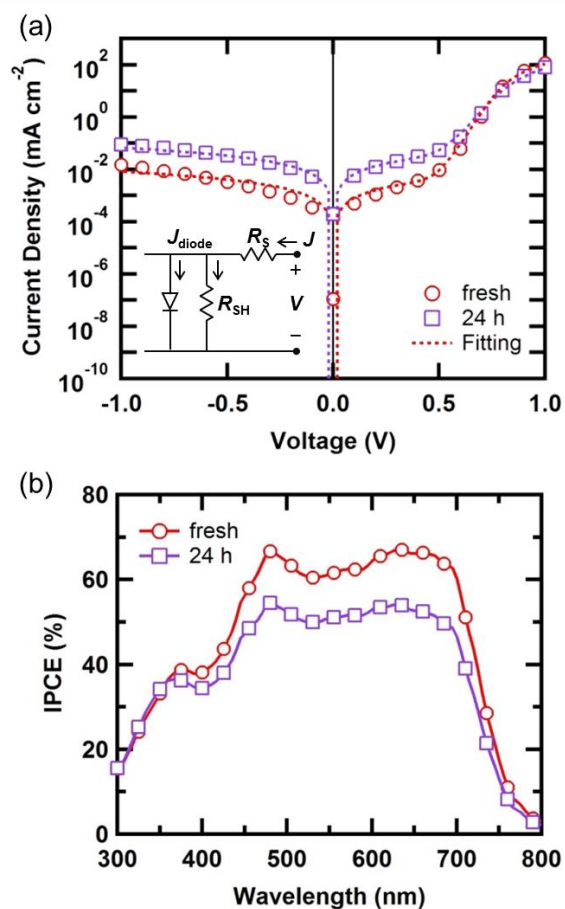


**Figure 4.6** (a) Dark  $J$ - $V$  characteristics on a semi-logarithmic scale and (b) IPCE spectra for PTB7:PC<sub>71</sub>BM solar cells before and after light-induced aging. The equivalent circuit diagram used for data fitting is shown in the inset of (a).

## 4.3 Investigation into the Light-induced Degradation Mechanisms

The morphological and electrical properties of active layer and devices were investigated by absorption spectra, atomic force microscopy, XPS spectra, and current density-voltage characteristics. To figure out the origin of photo-induced degradation, especially on the electrical degradation effects, various techniques including light intensity dependence of solar cell parameters, impedance spectroscopy, temperature dependence of  $J$ - $V$  in hole-only devices (HODs), and transient photocurrent decay were studied.

### 4.3.1 Light Intensity Dependent $J$ - $V$ Characteristics

Figure 4.7 shows the light intensity dependence of  $J_{SC}$  and  $V_{OC}$  so as to study the charge recombination characteristics before and after photo-induced aging process. Figure 4.7a shows the log-log plot of  $J_{SC}$  versus various incident light intensities, correlated following a power law as in Equation (2.9),  $J_{SC} \propto P_{light}^{\alpha}$ , where  $\alpha$  is the exponent. When the exponent value is close to unity, it indicates the weak bimolecular recombination in the organic solar cell devices.[63, 64] The fitted parameters yield  $\alpha$  values of 1.00 and 0.98 for fresh and light-aged device, respectively. The  $\alpha$  value was slightly decreased after the device had been kept under the continuous illumination for 24 h, but still both have weak bimolecular recombination.

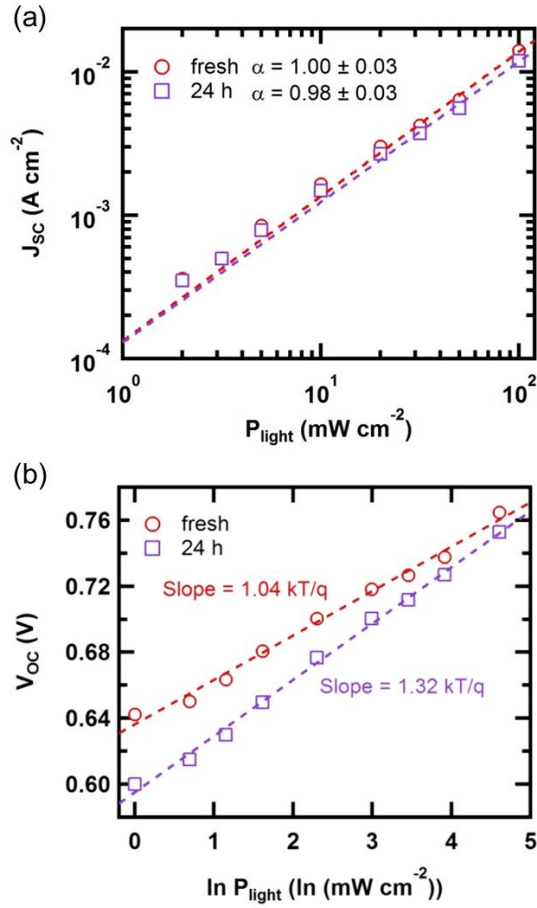


**Figure 4.7** Light intensity dependence of (a) short circuit current density ( $J_{sc}$ ) and (b) open circuit voltage ( $V_{oc}$ ) for the devices before and after aging process for 24 h. Dotted lines in (a) and (b) define power-law and linear fitting curves, respectively, and their fitting parameters are shown in the figures.

The  $V_{OC}$  as a function of light intensity was, in addition, measured to demonstrate the additional recombination mechanism of trap-assisted or Shockley-Read-Hall (SRH) recombination, as shown in Figure 4.7b. A slope of thermal voltage ( $kT/q$ ) represents the degree of trap-assisted recombination: the enhanced dependence of the open circuit voltage on the light intensity ( $2kT/q$ ) correlates with the more recombination losses,[65, 94] where  $k$  is the Boltzmann constant,  $T$  is the temperature, and  $q$  is the elementary charge. The fresh and aged devices showed a slope of  $1.04 kT/q$  and  $1.32 kT/q$ , respectively, implying increase of the trap-assisted recombination and more trap states inside the light-induced device. This is relevant to the previous photo-degradation studies for P3HT or PCDTBT-based solar cells showing the presence of light-induced traps in the active layer.[49, 57]

Collection voltages ( $V_C$ ) were then defined in order to investigate the difference in collection properties of solar cells during the light-induced degradation. As shown in Figure 4.8,  $V_C$  can be defined by a crossing point of all linear fits for the  $J$ - $V$  curves, which were measured at various light intensity ( $5$ - $100 \text{ mW cm}^{-2}$ ), at short circuit condition. The collection efficiency at short circuit condition ( $\eta_{CO}$ ) and effective  $\mu\tau$  product ( $\mu\tau_{eff}$ ) can be evaluated from the  $V_C$ . The determined  $V_C$  values are greatly reduced from  $5.62 \text{ V}$  to  $2.97 \text{ V}$  after the light-induced aging process. The corresponding  $\eta_{CO}$  and  $\mu\tau_{eff}$  are also degraded from  $84.9 \%$  and  $2.1 \times 10^{-10} \text{ cm}^2 \text{ V}^{-1}$  for fresh device to  $77.5 \%$  and  $1.7 \times 10^{-10} \text{ cm}^2 \text{ V}^{-1}$  for  $24 \text{ h}$ -aged device, respectively.

As a result from the light intensity dependent  $J$ - $V$  characteristics, it was observed that the aged device has more trap-assisted recombination losses, which may lead to an electrical degradation, reducing charge collection properties.

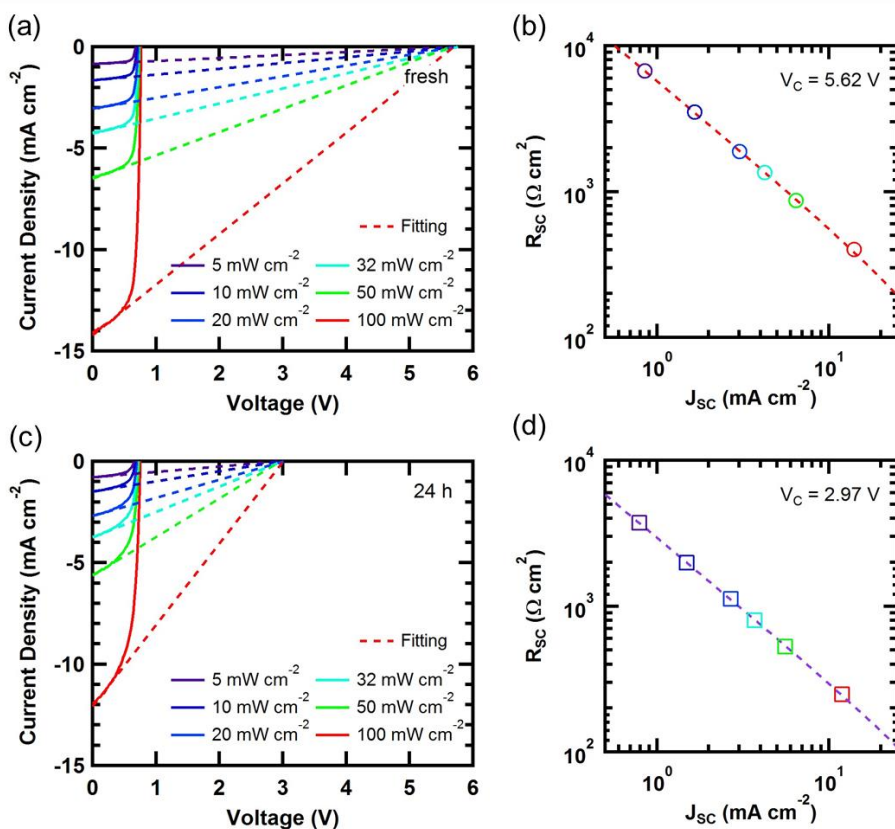


**Figure 4.8** Collection voltages ( $V_C$ ) of (a and b) fresh and (c and d) 24 h of light-induced aged devices. (b) and (d) show extracted short circuit resistance ( $R_{SC}$ ) at  $V = 0$ , and each point relates to the different incident light intensity (5-100  $\text{mW cm}^{-2}$ ).



### 4.3.2 Impedance Analysis

In order to explore the electrical degradation, impedance spectroscopy was conducted. Figure 4.9b-c shows Nyquist plots of impedance spectra depending on the incident light intensity before and after light-induced aging for frequencies from 1 kHz to 50 MHz. The data were measured at open circuit conditions where no photocurrent was observed. The equivalent circuit with a series of three parallel RC elements as shown in Figure 4.9a was applied to fit, where  $R_C$  is contact resistance and three RC circuits stand for bottom ZnO/bulk interface ( $R_{I1}$  and  $C_{I1}$ ), bulk ( $R_B$  and  $C_B$ ), and top bulk/MoO<sub>x</sub>/Ag interface ( $R_{I2}$  and  $C_{I2}$ ). By using this model, the impedance spectra were fitted with good agreement for under all light intensities as shown by the dotted lines of Figure 4.9b-c.

Fitted resistances ( $R_C$ ,  $R_{I1}$ ,  $R_B$ , and  $R_{I2}$ ) as a function of incident light intensities are shown in Figure 4.10, and all parameter values including capacitances are summarized in Table 4.2. It is notable to mention that the photoactive bulk layer is the thickest than others and the most sensitive to light as well, resulting in the largest values of R and the largest variations of R and C values depending on the different light intensities, respectively. To ensure our assignments for bottom (I1) and top (I2) interfaces, the additional experiments were carried out by changing the top interface as shown in Figure 4.11. The fitted results of impedance spectra for the device with different top interface (50 and 100 nm of MoO<sub>x</sub> layer) are well matched with the experimental data when  $R_{I1}$  and  $R_B$  were fixed with the same values of 10 nm-MoO<sub>x</sub> device. In addition,  $R_C$  and  $R_{I2}$  values are gradually increased according to the increase in MoO<sub>x</sub> thickness, which coincides with the device results in Figure 4.11a. Note that large fitting error above 20 % occurred when data were fitted by fixing the values of  $R_B$  and  $R_{I2}$ .

By going back to the impedance results of solar cell devices before and after light-induced aging as shown in Figure 4.10, resistance parameters of aged device show higher values than those of fresh sample, both in whole range of light intensity and for all elements, which is due to the light-induced degradation on electrical properties. Note that when decreasing the light intensity, resistance values of aged device for bottom and top interfaces, and bulk as well ( $R_{I1}$ ,  $R_{I2}$ , and  $R_B$ ) increase more rapidly than those of fresh one. Since only small amount of charges can be generated at low light power ( $\sim 1 \text{ mW/cm}^2$ ), this sharp increase could be an indication of existence of light-induced traps inside the photo-aged device. It is considered that all components including bulk and two adjacent interfaces, especially top interface, are regions that traps are located at. This is also supported by our above results of increase in trap-assisted recombination for photo-aged device.

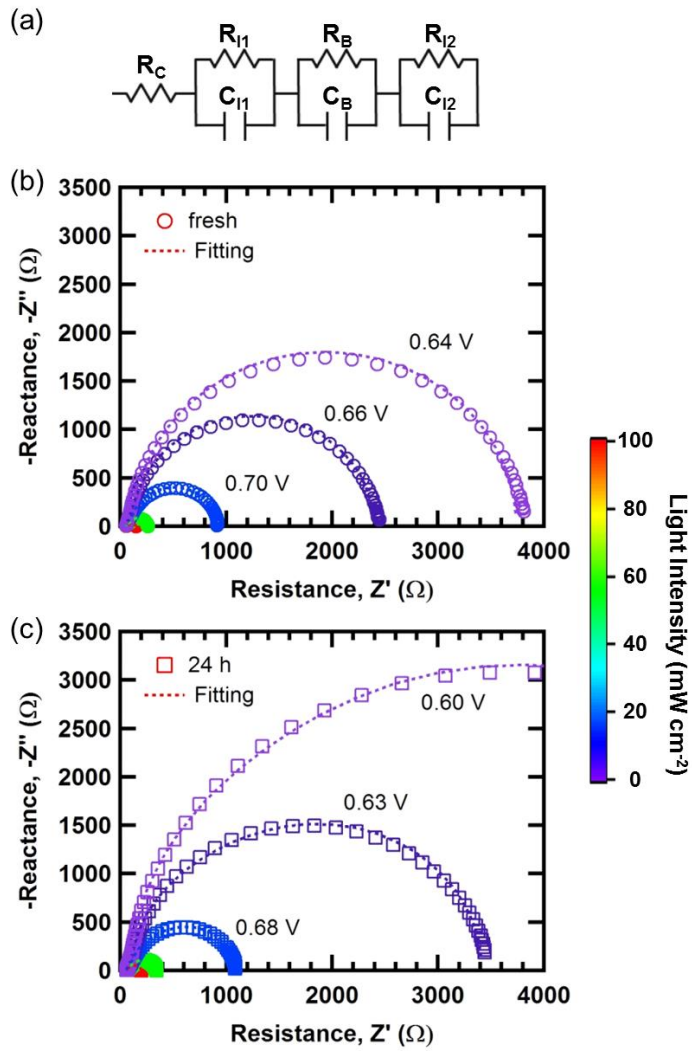


**Figure 4.9** Nyquist plots measured under various illumination intensities (1, 3, 10, 50, and 100  $\text{mW cm}^{-2}$ ) at open circuit conditions for PTB7:PC<sub>71</sub>BM solar cell devices (b) before and (c) after 24 h of light-induced aging. The marked voltages in figures represent to open circuit voltages, which were applied to devices, and (a) shows an equivalent circuit model used for data fitting.

**Table 4.2** Fitting parameter values (R and C) extracted from the impedance spectroscopy using solar cell equivalent circuit model shown in the Figure 4.9a.  $R_C$  represents contact resistance, and three RC components are assigned as bottom ZnO/bulk interface ( $R_{I1}$  &  $C_{I1}$ ), bulk ( $R_B$  &  $C_B$ ), and top bulk/MoO<sub>x</sub>/Ag interface ( $R_{I2}$  &  $C_{I2}$ ).

	Light intensity (mW cm <sup>-2</sup> )	$R_C$ ( $\Omega$ )	$R_{I1}$ ( $\Omega$ )	$C_{I1}$ (nF)	$R_B$ ( $\Omega$ )	$C_B$ (nF)	$R_{I2}$ ( $\Omega$ )	$C_{I2}$ (nF)
fresh	100	53.23	8.79	0.64	63.59	6.22	21.69	2.17
	50	51.48	10.19	0.56	162.04	4.26	33.80	1.99
	10	48.44	11.92	0.48	801.36	2.26	50.17	2.16
	3	53.51	11.52	1.31	2273.81	1.65	55.05	3.59
	1	54.62	15.80	1.83	3594.09	1.49	72.75	5.25
24 h- aged	100	60.40	18.29	1.20	80.84	5.70	38.69	2.76
	50	59.97	26.54	1.24	187.30	4.47	65.45	3.04
	10	60.17	42.21	1.41	806.08	3.04	172.18	4.05
	3	60.50	47.17	1.65	2605.52	2.87	700.19	3.37
	1	60.92	45.47	1.83	5644.78	2.52	1222.69	3.31

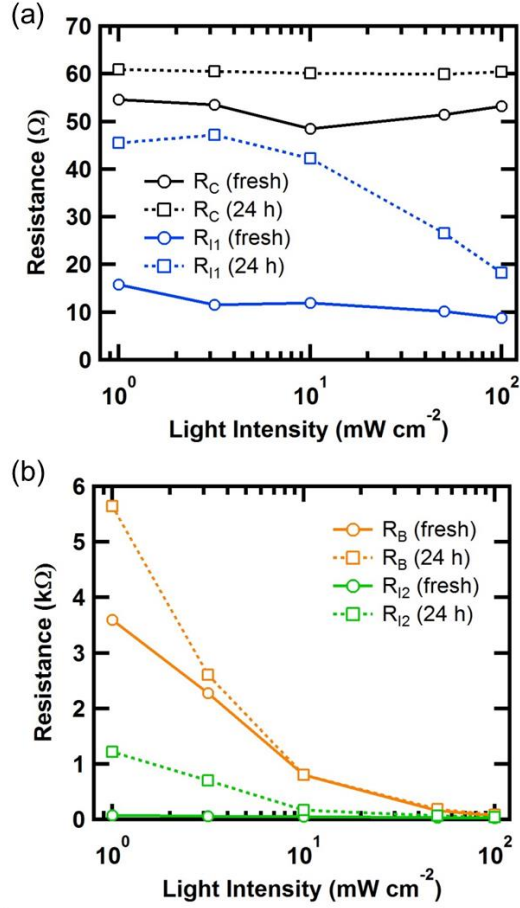


**Figure 4.10** Fitting parameters of (a) contact ( $R_C$ ), bottom ZnO/bulk interface ( $R_{I1}$ ), (b) bulk ( $R_B$ ), and top bulk/MoO<sub>x</sub>/Ag interface ( $R_{I2}$ ) resistance values for the devices before and after light aging as a function of light intensity.

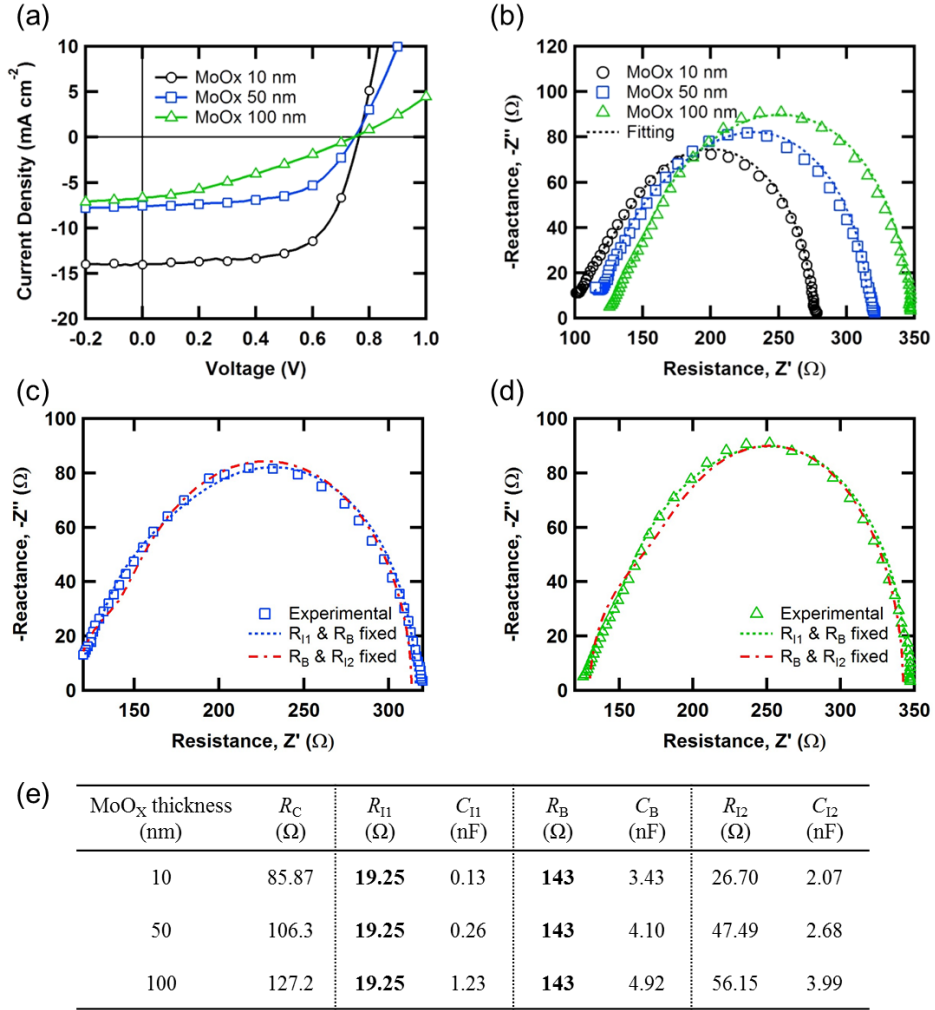


**Figure 4.11** (a)  $J$ - $V$  characteristics and (b) Nyquist plots for PTB7:PC<sub>71</sub>BM solar cells with various thicknesses of MoO<sub>x</sub> layer (10, 50, and 100 nm). Two different fitting curves are shown in (c and d) for the same experimental data of the device with (c) 50 nm-MoO<sub>x</sub> and (d) 100 nm-MoO<sub>x</sub>: “ $R_{11}$  &  $R_B$  fixed” and “ $R_B$  &  $R_{12}$  fixed”. Fixed parameters here are from the values of fitting results for the device with 10 nm of MoO<sub>x</sub>. (e) Summarized fitting parameter values (R and C) when  $R_{11}$  and  $R_B$  are maintained with the same values of 10 nm-MoO<sub>x</sub> device.

### 4.3.3 Charge Carrier Conduction Properties

To further study the effects of light-induced degradation on charge transport properties, especially of the active layer, temperature dependent  $J$ - $V$  measurements of hole-only devices (HODs) were performed. Figure 4.12a and b show the  $J$ - $V$  characteristics for the fresh and aged HODs, respectively, each presenting two different charge transport regions depending on the voltage.

In case of fresh device, at low voltage ( $< 2$  V), current density varies linearly with the voltage, which is a typical signature of free carrier conduction following Ohm's law. Electrical conductivity ( $\sigma$ ) of the active layer can then be calculated from this region, and it increases from  $8.00 \times 10^{-8} \text{ S cm}^{-1}$  to  $1.92 \times 10^{-6} \text{ S cm}^{-1}$  by an increase in temperature from 150 K to 325 K. Likewise, temperature dependent conductivity for light-aged device was also obtained, and calculated values are shown in Figure 4.12c together with conductivity of fresh device. It is readily observed that  $\sigma$  decreased by nearly two orders of magnitude due to the photo-induced degradation.

At the same time, at higher voltage above 2 V, current density in fresh sample presents a quadratic dependence on the voltage ( $J \propto V^2$ ), indicating space charge formation in photoactive layer.[73] The deviations of current density from quadratic dependence in high-voltage regime ( $> 7\sim 10$  V) are due to a field-dependent mobility.[74] The  $J$ - $V$  characteristics are thus modeled using the field-dependent space-charge-limited current (SCLC) as Equation (2.17):

$$J = \frac{9}{8} \varepsilon_0 \varepsilon_r \mu_0 \exp(\beta \sqrt{F}) \frac{V^2}{d^3} \quad (2.17)$$

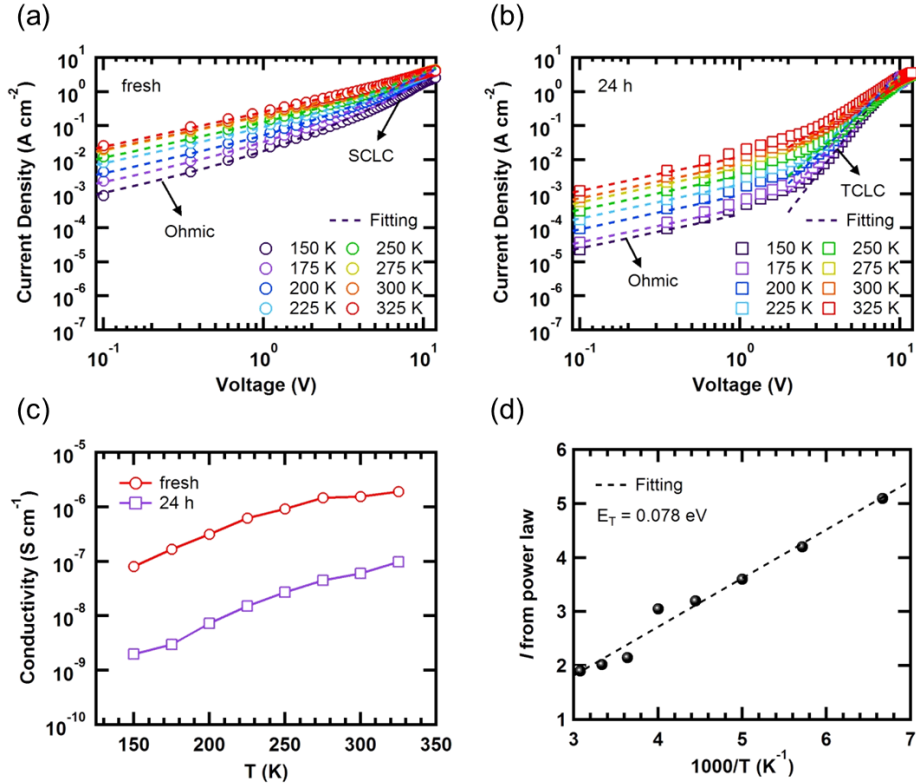


**Figure 4.12**  $J$ - $V$  characteristics of hole-only-devices (a) before and (b) after light-induced aging with a structure of ITO/PEDOT:PSS/PTB7:PC<sub>71</sub>BM/MoO<sub>x</sub>/Au, measured at various temperatures. (c) Calculated electrical conductivity of active layer as a function of temperature for fresh and aged devices. (d) Temperature dependence of  $l$  from Equation (2.18) and its linear fitting curve in order to extract the trap energy in 24 h-aged device. Dotted lines in (a) and (b) show fitting curves using space-charge-limited current conduction (SCLC) and trap-charge-limited current conduction (TCLC) model for fresh device and aged device, respectively.



where  $\epsilon_0$  and  $\epsilon_r$  represent the permittivity of free space and relative dielectric constant, respectively,  $\mu_0$  is the zero-field mobility,  $\beta$  is the Pool-Frenkel (PF) coefficient,  $F$  is the applied electric field, and  $d$  is the thickness of active layer. With a dielectric constant of 3,  $J$ - $V$  curves were fitted using Equation (2.17) at high voltage region by varying both  $\mu_0$  and  $\beta$ . The obtained values of  $\mu_0$  were increased from  $1.0 \times 10^{-5} \text{ cm}^2 \text{ V}^{-1} \text{ s}^{-1}$  to  $2.4 \times 10^{-5} \text{ cm}^2 \text{ V}^{-1} \text{ s}^{-1}$ , when the temperature was getting higher from 150 K to 325 K, while  $\beta$  values changed from  $1.0 \times 10^{-3} (\text{cm V}^{-1})^{1/2}$  to  $5.0 \times 10^{-5} (\text{cm V}^{-1})^{1/2}$ .

For light-induced aged device at high voltage region, on the other hand, current follows a power law behavior on the voltage ( $J \propto V^{l+1}$ ), where the exponent  $l$  is given by trap energy  $E_t = kT$  depending on the temperature.  $E_t$  can now be obtained from the slope of  $l$  versus  $1/T$  curve as shown in Figure 4.12d, yielding 78 meV of trap energy, which is almost three times higher than the thermal energy at room temperature. This indicates that the charge carrier conduction mechanism in light-induced degraded device is highly trap-charge-limited; therefore, we modeled the higher voltage region of aged sample using a trap-charge-limited current (TCLC) conduction model in which the  $J$ - $V$  characteristics are given as Equation (2.18):

$$J = q^{1-l} \mu N_v \left( \frac{2l+1}{l+1} \right)^{l+1} \left( \frac{\epsilon_0 \epsilon_r}{N_t} \frac{l}{l+1} \right)^l \frac{V^{l+1}}{d^{2l+1}} \quad (2.18)$$

where  $N_t$  is the trap density and  $N_v$  is the effective density of states, which value was taken as  $10^{21} \text{ cm}^{-3}$  in this work.[95]  $J$ - $V$  characteristics were then fitted using Equation (2.18) to extract trap density with keeping  $\mu$  fixed ( $1.0 \times 10^{-7} \text{ cm}^2 \text{ V}^{-1} \text{ s}^{-1}$ ). As a result, significantly high trap carrier density of  $(8.3 \pm 2.0) \times 10^{17} \text{ cm}^{-3}$  was obtained in photo-induced device.

To compare with the fresh device, we have estimated the free carrier concentration in fresh sample by using the calculated electrical conductivity and charge carrier mobility. The calculated values of free carrier concentration were found to be in the range of  $5.0 \times 10^{16} \text{ cm}^{-3}$  to  $5.0 \times 10^{17} \text{ cm}^{-3}$  when the temperature range is from 150 K to 325 K. Note that the same order of magnitude as free carrier density was observed for trap carrier density in 24 h of light-induced aged device, which possibly leads to the reduction in photocurrent and eventually performance loss of solar cell.

Furthermore, we measured the transient photocurrent for both fresh and photo-aged solar cell devices to compare the decay dynamics. As shown in Figure 4.13, the average charge transit time obtained from the transient response increases from 188  $\mu\text{s}$  to 292  $\mu\text{s}$  during the 24 h of light-induced aging. It reveals that generated charges take more time to be collected in aged device, supporting our analysis of decrease in mobility and photo-induced trap formation.

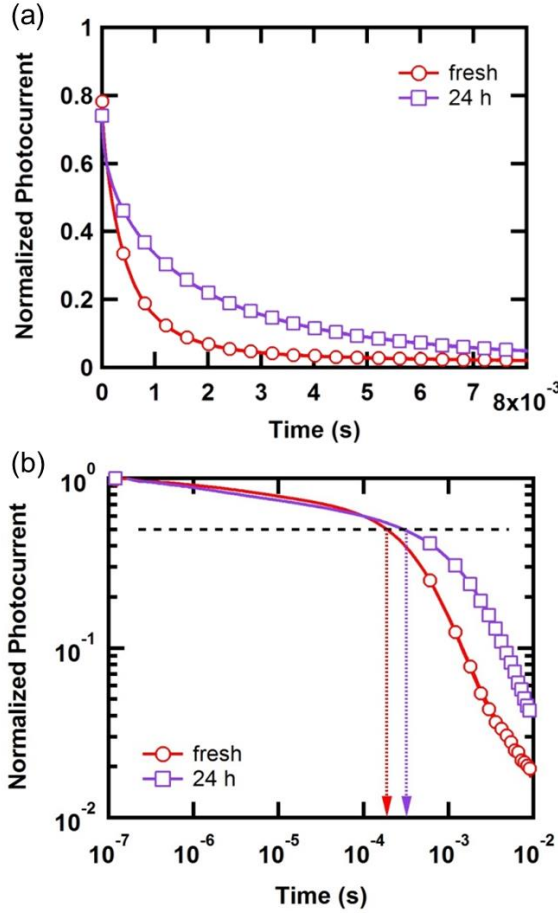


**Figure 4.13** Normalized photocurrent decay dynamics on a (a) linear scale and (b) log-log scale for devices before and after light-induced aging. Nd:YAG pulsed laser (pulse duration  $\sim 5$  ns,  $\lambda = 590$  nm) was used as an excitation source.

## 4.4 Summary

In summary, the light-induced degradation of PTB7-based organic solar cells in the first 24 hours was demonstrated. After a day of continuous light-aging with minimized other extrinsic factors, solar cell device showed 30 % of initial performance drop, mainly through a decrease in  $J_{SC}$  and FF. By investigating change in optical, structural, morphological, and electrical properties of active layer and devices, we conclude that the loss is primarily due to light-induced traps inside the bulkheterojunction and two adjacent interfaces. Temperature dependent  $J$ - $V$  characteristics also support photo-induced traps inside the active layer, showing highly trap-charge-limited conduction mechanism with 78 meV of trap energy. These increased traps may lead to electrical degradation on solar cell device, resulting in reduced hole mobility, photocurrent, and device performance at last. Further studies are needed not only to investigate more about degradation mechanisms for low bandgap polymer-based solar cells, but to resolve the issues discussed here for achieving better stability of organic solar cells.

## Chapter 5

## Conclusion

In this thesis, the efficiency improvement and understanding of light-induced degradation mechanism for organic solar cells were investigated. The solar cells were prepared with high performance PTB7 polymer as a donor by employing the inverted-type of structure.

First of all, in order to improve the power conversion efficiency especially in terms of charge extraction enhancement, a unique nanostructured electron-selective interlayer comprising of In-doped ZnO (ZnO:In) and vertically-aligned CdSe tetrapods (TPs) was introduced. By providing the direct inorganic path from the disordered bulkheterojunction domain to electron buffer layer, CdSe TPs layer can effectively extract photogenerated charge carriers, leading to the improvement of both  $J_{SC}$  and FF of the solar cell devices. It was demonstrated from recombination and charge collection analysis that CdSe TPs can effectively reduce the interfacial

traps between the BHJ layer and buffer layer, reduce the recombination losses, improve the hole-blocking properties as well as electron-transporting, and therefore improve charge collection. Consequently, the power conversion efficiency of PTB7:PC<sub>71</sub>BM based solar cell with nanostructured CdSe TPs increases to 7.55%. Moreover, the use of length-controlled inorganic nanocrystals as an interlayer is expected to be a general platform for improving charge extraction in thin film solar cells.

Besides, systematic study for understanding the light-induced degradation mechanisms of organic solar cells was also performed. After a day of continuous light-aging with minimized other extrinsic factors, solar cell device showed 30 % of initial performance drop, mainly through a decrease in  $J_{SC}$  and FF. By investigating change in optical, structural, morphological, and electrical properties of active layer and devices, we conclude that the loss is primarily due to light-induced traps inside the bulkheterojunction and two adjacent interfaces. Temperature dependent  $J$ - $V$  characteristics also support light-induced traps inside the bulkheterojunction and two adjacent interfaces, which are found to be a primary cause of loss. Furthermore, this trap formation was observed with energy of 78 meV and with substantially high density of  $(8.3 \pm 2.0) \times 10^{17} \text{ cm}^{-3}$ , leading to highly trap-charge-limited conduction properties, electrical degradation of solar cells, and device performance at last. Further studies are open not only to investigate more about degradation mechanisms, but to resolve the issues discussed here for achieving better stability of organic solar cells.

In conclusion, this thesis proposes the practical approaches to enhance power conversion efficiency and to understand light-induced degradation mechanism of inverted organic solar cells. These approaches and various measurement techniques including optical and electrical characterization methods introduced herein are

expected to be applied not only to solar cells but also to other kinds of organic optoelectronic devices, such as OLEDs and organic thin-film transistors.

# Bibliography

- [1] M. C. Beard, J. M. Luther, and A. J. Nozik, “The promise and challenge of nanostructured solar cells,” *Nature Nanotechnology*, vol. 9, no. 12, pp. 951-954, December 2014.
- [2] C. Lungenschmied, G. Dennler, H. Neugebauer, *et al.*, “Flexible, long-lived, large-area, organic solar cells,” *Solar Energy Materials and Solar Cells*, vol. 91, no. 5, pp. 379-384, March 2007.
- [3] F. C. Krebs, H. Spanggaard, T. Kjær, *et al.*, “Large area plastic solar cell modules,” *Materials Science and Engineering: B*, vol. 138, no. 2, pp. 106-111, March 2007.
- [4] C. W. Tang, “Two- layer organic photovoltaic cell,” *Applied Physics Letters*, vol. 48, no. 2, pp. 183-185, January 1986.
- [5] C. Liu, C. Yi, K. Wang, *et al.*, “Single-junction polymer solar cells with over 10% efficiency by a novel two-dimensional donor–acceptor conjugated copolymer,” *ACS Applied Materials & Interfaces*, vol. 7, no. 8, pp. 4928-4935, March 2015.
- [6] Z. He, B. Xiao, F. Liu, *et al.*, “Single-junction polymer solar cells with high efficiency and photovoltage,” *Nature Photonics*, vol. 9, no. 3, pp. 174-179, March 2015.



- [7] J. -D. Chen, C. Cui, Y. -Q. Li, *et al.*, “Single-junction polymer solar cells exceeding 10% power conversion efficiency,” *Advanced Materials*, vol. 27, no. 6, pp. 1035-1041, February 2015.
- [8] B. Kan, M. Li, Q. Zhang, *et al.*, “A series of simple oligomer-like small molecules based on oligothiophenes for solution-processed solar cells with high efficiency,” *Journal of American Chemical Society*, vol. 137, no. 11, pp. 3886-3893, March 2015.
- [9] J. Zhao, Y. Li, G. Yang, *et al.*, “Efficient organic solar cells processed from hydrocarbon solvents,” *Nature Energy*, vol. 1, pp. 15027, January 2016.
- [10] J. You, L. Dou, K. Yoshimura, *et al.*, “A polymer tandem solar cell with 10.6% power conversion efficiency,” *Nature Communications*, vol. 4, pp. 1446, February 2013.
- [11] Y. -J. Cheng, S. -H. Yang, and C. -S. Hsu, “Synthesis of conjugated polymers for organic solar cell applications,” *Chemical Reviews*, vol. 109, no. 11, pp. 5868-5923, November 2009.
- [12] G. Li, V. Shrotriya, J. Huang, *et al.*, “High-efficiency solution processable polymer photovoltaic cells by self-organization of polymer blends,” *Nature Materials*, vol. 4, no. 11, pp. 864-868, November 2005.
- [13] W. Ma, C. Yang, X. Gong, *et al.*, “Thermally stable, efficient polymer solar cells with nanoscale control of the interpenetrating network morphology,” *Advanced Functional Materials*, vol. 15, no. 10, pp. 1617-1622, October 2005.
- [14] S. H. Park, A. Roy, S. Beaupre, *et al.*, “Bulk heterojunction solar cells with internal quantum efficiency approaching 100%,” *Nature Photonics*, vol. 3, no. 5, pp. 297-302, May 2009.

- [15] Y. Liang, Z. Xu, J. Xia, *et al.*, “For the bright future—bulk heterojunction polymer solar cells with power conversion efficiency of 7.4%,” *Advanced Materials*, vol. 22, no. 20, pp. E135-E138, May 2010.
- [16] S. -H. Liao, H. -J. Jhuo, Y. -S. Cheng, *et al.*, “Fullerene derivative-doped zinc oxide nanofilm as the cathode of inverted polymer solar cells with low-bandgap polymer (PTB7-Th) for high performance,” *Advanced Materials*, vol. 25, no. 34, pp. 4766-4771, September 2013.
- [17] M. Jørgensen, K. Norrman, S. A. Gevorgyan, *et al.*, “Stability of polymer solar cells,” *Advanced Materials*, vol. 24, no. 5, pp. 580-612, February 2012.
- [18] P. Cheng and X. Zhan, “Stability of organic solar cells: challenges and strategies,” *Chemical Society Reviews*, vol. 45, no. 9, pp. 2544-2582, May 2016.
- [19] M. Hermenau, M. Riede, K. Leo, *et al.*, “Water and oxygen induced degradation of small molecule organic solar cells,” *Solar Energy Materials and Solar Cells*, vol. 95, no. 5, pp. 1268-1277, May 2011.
- [20] S. Bertho, I. Haeldermans, A. Swinnen, *et al.*, “Influence of thermal ageing on the stability of polymer bulk heterojunction solar cells,” *Solar Energy Materials and Solar Cells*, vol. 91, no. 5, pp. 385-389, May 2007.
- [21] A. Rivaton, S. Chambon, M. Manceau, *et al.*, “Light-induced degradation of the active layer of polymer-based solar cells,” *Polymer Degradation and Stability*, vol. 95, no. 3, pp. 278-284, March 2010.
- [22] W. Li, K. H. Hendriks, W. S. C. Roelofs, *et al.*, “Efficient small bandgap polymer solar cells with high fill factors for 300 nm thick films,” *Advanced Materials*, vol. 25, no. 23, pp. 3182-3186, June 2013.
- [23] Y. Liu, J. Zhao, Z. Li, *et al.*, “Aggregation and morphology control enables multiple cases of high-efficiency polymer solar cells,” *Nature Communications*, vol. 5, pp. 5293, November 2014.

- [24] S. Liu, R. Jiang, P. You, *et al.*, “Au/Ag core-shell nanocuboids for high-efficiency organic solar cells with broadband plasmonic enhancement,” *Energy & Environmental Science*, vol. 9, no. 3, pp. 898-905, March 2016.
- [25] V. Shrotriya, G. Li, Y. Yao, *et al.*, “Transition metal oxides as the buffer layer for polymer photovoltaic cells,” *Applied Physics Letters*, vol. 88, no. 7, pp. 073508, February 2006.
- [26] D. Y. Kim, J. Subbiah, G. Sarasqueta, *et al.*, “The effect of molybdenum oxide interlayer on organic photovoltaic cells,” *Applied Physics Letters*, vol. 95, no. 9, pp. 093304, August 2009.
- [27] K. Takanezawa, K. Tajima, and K. Hashimoto, “Efficiency enhancement of polymer photovoltaic devices hybridized with ZnO nanorod arrays by the introduction of a vanadium oxide buffer layer,” *Applied Physics Letters*, vol. 93, no. 6, pp. 063308, August 2008.
- [28] T. Stubhan, N. Li, N. A. Luechinger, *et al.*, “High fill factor polymer solar cells incorporating a low temperature solution processed WO<sub>3</sub> hole extraction layer,” *Advanced Energy Materials*, vol. 2, no. 12, pp. 1433-1438, December 2012.
- [29] M. D. Irwin, D. B. Buchholz, A. W. Hains, *et al.*, “p-Type semiconducting nickel oxide as an efficiency-enhancing anode interfacial layer in polymer bulk-heterojunction solar cells,” *Proceedings of the National Academy of Sciences of the United States of America*, vol. 105, no. 8, pp. 2783-2787, February 2008.
- [30] Y. S. Kim, B. -K. Yu, D. -Y. Kim, *et al.*, “A hybridized electron-selective layer using Sb-doped SnO<sub>2</sub> nanowires for efficient inverted polymer solar cells,” *Solar Energy Materials and Solar Cells*, vol. 95, no. 10, pp. 2874-2879, October 2011.
- [31] J. Y. Kim, S. H. Kim, H. H. Lee, *et al.*, “New architecture for high-efficiency polymer photovoltaic cells using solution-based titanium oxide as an optical spacer,” *Advanced Materials*, vol. 18, no. 5, pp. 572-576, March 2006.

- [32] S. K. Hau, H. -L. Yip, N. S. Baek, *et al.*, “Air-stable inverted flexible polymer solar cells using zinc oxide nanoparticles as an electron selective layer,” *Applied Physics Letters*, vol. 92, no. 25, pp. 253301, June 2008.
- [33] Y. Sun, J. H. Seo, C. J. Takacs, *et al.*, “Inverted polymer solar cells integrated with a low-temperature-annealed sol-gel-derived ZnO film as an electron transport layer,” *Advanced Materials*, vol. 23, no. 14, pp. 1679-1683, April 2011.
- [34] H. Choi, J. S. Park, E. Jeong, *et al.*, “Combination of titanium oxide and a conjugated polyelectrolyte for high-performance inverted-type organic optoelectronic devices,” *Advanced Materials*, vol. 23, no. 24, pp. 2759-2763, June 2011.
- [35] T. Yang, M. Wang, C. Duan, *et al.*, “Inverted polymer solar cells with 8.4% efficiency by conjugated polyelectrolyte,” *Energy & Environmental Science*, vol. 5, no. 8, pp. 8208-8214, August 2012.
- [36] H. Oh, J. Krantz, I. Litsov, *et al.*, “Comparison of various sol–gel derived metal oxide layers for inverted organic solar cells,” *Solar Energy Materials and Solar Cells*, vol. 95, no. 8, pp. 2194-2199, August 2011.
- [37] M. Thambidurai, J. Y. Kim, J. Song, *et al.*, “High performance inverted organic solar cells with solution processed Ga-doped ZnO as an interfacial electron transport layer,” *Journal of Materials Chemistry C*, vol. 1, no. 48, pp. 8161-8166, December 2013.
- [38] X. Liu, X. Li, Y. Li, *et al.*, “High-performance polymer solar cells with PCE of 10.42% via Al-doped ZnO cathode interlayer,” *Advanced Materials*, vol. 28, no. 34, pp. 7405-7412, September 2016.
- [39] M. Thambidurai, J. Y. Kim, C. -m. Kang, *et al.*, “Enhanced photovoltaic performance of inverted organic solar cells with In-doped ZnO as an electron extraction layer,” *Renewable Energy*, vol. 66, pp. 433-442, June 2014.

- [40] J. Liu, S. Wang, Z. Bian, *et al.*, “Organic/inorganic hybrid solar cells with vertically oriented ZnO nanowires,” *Applied Physics Letters*, vol. 94, no. 17, pp. 173107, April 2009.
- [41] S. Kim, C. H. Kim, S. K. Lee, *et al.*, “Highly efficient uniform ZnO nanostructures for an electron transport layer of inverted organic solar cells,” *Chemical Communications*, vol. 49, no. 54, pp. 6033-6035, July 2013.
- [42] S. Y. Park, B. J. Kim, K. Kim, *et al.*, “Low-temperature, solution-processed and alkali metal doped ZnO for high-performance thin-film transistors,” *Advanced Materials*, vol. 24, no. 6, pp. 834-838, February 2012.
- [43] Al. L. Efros and M. Rosen, “The electronic structure of semiconductor nanocrystals,” *Annual Review of Materials Science*, vol. 30, pp. 475-521, August 2000.
- [44] D. V. Talapin, J. -S. Lee, M. V. Kovalenko, *et al.*, “Prospects of colloidal nanocrystals for electronic and optoelectronic applications,” *Chemical Reviews*, vol. 110, no. 1, pp. 389-458, January 2010.
- [45] S. Ren, L. -Y. Chang, S. -K. Lim, *et al.*, “Inorganic–organic hybrid solar cell: bridging quantum dots to conjugated polymer nanowires,” *Nano Letters*, vol. 11, no. 9, pp. 3998-4002, September 2011.
- [46] Z. Liu, Y. Sun, J. Yuan, *et al.*, “High-efficiency hybrid solar cells based on polymer/PbS<sub>x</sub>Se<sub>1-x</sub> nanocrystals benefiting from vertical phase segregation,” *Advanced Materials*, vol. 25, no. 40, pp. 5772-5778, October 2013.
- [47] J. Lim, D. Lee, M. Park, *et al.*, “Modular fabrication of hybrid bulk heterojunction solar cells based on breakwater-like CdSe tetrapod nanocrystal network infused with P3HT,” *Journal of Physical Chemistry C*, vol. 118, no. 8, pp. 3942-3952, February 2014.

- [48] H. Cao, W. He, Y. Mao, *et al.*, “Recent progress in degradation and stabilization of organic solar cells, *Journal of Power Sources*, vol. 264, pp. 168-183, October 2014.
- [49] C. H. Peters, I. T. Sachs-Quintana, W. R. Mateker, *et al.*, “The mechanism of burn-in loss in a high efficiency polymer solar cell,” *Advanced Materials*, vol. 24, no. 5, pp. 663-668, February 2012.
- [50] J. M. Kroon, M. M. Wienk, W. J. H. Verhees, *et al.*, “Accurate efficiency determination and stability studies of conjugated polymer/fullerene solar cells,” *Thin Solid Films*, vol. 403–404, pp. 223-228, February 2002.
- [51] M. O. Reese, A. J. Morfa, M. S. White, *et al.*, “Pathways for the degradation of organic photovoltaic P3HT:PCBM based devices,” *Solar Energy Materials and Solar Cells*, vol. 92, no. 7, pp. 746-752, July 2008.
- [52] Y. Tamai, H. Ohkita, M. Namatame, *et al.*, “Light-induced degradation mechanism in poly(3-hexylthiophene)/fullerene blend solar cells,” *Advanced Energy Materials*, vol. 6, no. 11, pp. 1600171, June 2016.
- [53] M. Manceau, S. Chambon, A. Rivaton, *et al.*, “Effects of long-term UV–visible light irradiation in the absence of oxygen on P3HT and P3HT:PCBM blend,” *Solar Energy Materials and Solar Cells*, vol. 94, no. 10, pp. 1572-1577, October 2010.
- [54] M. Manceau, A. Rivaton, J. -L. Gardette, *et al.*, “Light-induced degradation of the P3HT-based solar cells active layer,” *Solar Energy Materials and Solar Cells*, vol. 95, no. 5, pp. 1315-1325, May 2011.
- [55] M. O. Reese, A. M. Nardes, B. L. Rupert, *et al.*, “Photoinduced degradation of polymer and polymer–fullerene active layers: experiment and theory,” *Advanced Functional Materials*, vol. 20, no. 20, pp. 3476-3483, October 2010.

- [56] A. Kumar, R. Devine, C. Mayberry, *et al.*, “Origin of radiation-induced degradation in polymer solar cells,” *Advanced Functional Materials*, vol. 20, no. 16, pp. 2729-2736, August 2010.
- [57] S. Khelifi, E. Voroshazi, D. Spoltore, *et al.*, “Effect of light induced degradation on electrical transport and charge extraction in polythiophene:fullerene (P3HT:PCBM) solar cells,” *Solar Energy Materials and Solar Cells*, vol. 120, Part A, pp. 244-252, January 2014.
- [58] G. Williams, Q. Wang, and H. Aziz, “The photo-stability of polymer solar cells: contact photo-degradation and the benefits of interfacial layers,” *Advanced Functional Materials*, vol. 23, no. 18, pp. 2239-2247, May 2013.
- [59] C. J. Brabec, A. Cravino, D. Meissner, *et al.*, “Origin of the open circuit voltage of plastic solar cells,” *Advanced Functional Materials*, vol. 11, no. 5, pp. 374-380, October 2001.
- [60] M. C. Scharber, D. Mühlbacher, M. Koppe, *et al.*, “Design rules for donors in bulk-heterojunction solar cells—towards 10 % energy-conversion efficiency,” *Advanced Materials*, vol. 18, no. 6, pp. 789-794, March 2006.
- [61] C. Pacholski, A. Kornowski, and H. Weller, “Self-assembly of ZnO: from nanodots to nanorods,” *Angewandte Chemie International Edition*, vol. 41, no. 7, pp. 1188-1191, April 2002.
- [62] J. Lim, W. K. Bae, K. U. Park, *et al.*, “Controlled synthesis of CdSe tetrapods with high morphological uniformity by the persistent kinetic growth and the halide-mediated phase transformation,” *Chemistry of Materials*, vol. 25, no. 8, pp. 1443-1449, April 2013.
- [63] P. Schilinsky, C. Waldauf, and C. J. Brabec, “Recombination and loss analysis in polythiophene based bulk heterojunction photodetectors,” *Applied Physics Letters*, vol. 81, no. 20, pp. 3885-3887, November 2002.

- [64] I. Riedel, J. Parisi, V. Dyakonov, *et al.*, “Effect of temperature and illumination on the electrical characteristics of polymer–fullerene bulk-heterojunction solar cells,” *Advanced Functional Materials*, vol. 14, no. 1, pp. 38–44, January 2004.
- [65] S. R. Cowan, A. Roy, and A. J. Heeger, “Recombination in polymer-fullerene bulk heterojunction solar cells,” *Physical Review B*, vol. 82, no. 24, pp. 245207, December 2010.
- [66] A. K. Kyaw, D. H. Wang, D. Wynands, *et al.*, “Improved light harvesting and improved efficiency by insertion of an optical spacer (ZnO) in solution-processed small-molecule solar cells,” *Nano Letters*, vol. 13, no. 8, pp. 3796–3801, August 2013.
- [67] C. Voz, J. Puigdollers, J. M. Asensi, *et al.*, “Analysis of the dynamic short-circuit resistance in organic bulk-heterojunction solar cells: relation to the charge carrier collection efficiency,” *Organic Electronics*, vol. 14, no. 6, pp. 1643–1648, June 2013.
- [68] C. Hof, N. Wyrsh, and A. Shah, “Influence of electric field distortion and i-layer quality on the collection function of drift-driven a-Si:H solar cells,” *Journal of Non-Crystalline Solids*, vol. 266–269, Part 2, pp. 1114–1118, May 2000.
- [69] G. Garcia-Belmonte, P. P. Boix, J. Bisquert, *et al.*, “Simultaneous determination of carrier lifetime and electron density-of-states in P3HT:PCBM organic solar cells under illumination by impedance spectroscopy,” *Solar Energy Materials and Solar Cells*, vol. 94, no. 2, pp. 366–375, February 2010.
- [70] W. L. Leong, S. R. Cowan, and A. J. Heeger, “Differential resistance analysis of charge carrier losses in organic bulk heterojunction solar cells: observing the transition from bimolecular to trap-assisted recombination and quantifying the order of recombination,” *Advanced Energy Materials*, vol. 1, no. 4, pp. 517–522, July 2011.



- [71] R. C. I. MacKenzie, C. G. Shuttle, G. F. Dibb, *et al.*, “Interpreting the density of states extracted from organic solar cells using transient photocurrent measurements,” *Journal of Physical Chemistry C*, vol. 117, no. 24, pp. 12407-12414, June 2013.
- [72] C. G. Shuttle, N. D. Treat, J. D. Douglas, *et al.*, “Deep energetic trap states in organic photovoltaic devices,” *Advanced Energy Materials*, vol. 2, no. 1, pp. 111-119, January 2012.
- [73] M. A. Lampert and P. Mark, *Current injection in solids*. New York: Academic Press, 1970.
- [74] P. W. M. Blom, M. J. M. de Jong, and M. G. van Munster, “Electric-field and temperature dependence of the hole mobility in poly(p-phenylene vinylene),” *Physical Review B*, vol. 55, no. 2, R656-R659, January 1997.
- [75] P. N. Murgatroyd, “Theory of space-charge-limited current enhanced by Frenkel effect,” *Journal of Physics D: Applied Physics*, vol. 3, no. 2, pp. 151-156, February 1970.
- [76] A. Rose, “Space-charge-limited currents in solids,” *Physical Review*, vol. 97, no. 6, pp. 1538-1544, March 1955.
- [77] P. Mark and W. Helfrich, “Space- charge- limited currents in organic crystals,” *Journal of Applied Physics*, vol. 33, no. 1, pp. 205-215, January 1962.
- [78] Z. He, C. Zhong, S. Su, *et al.*, “Enhanced power-conversion efficiency in polymer solar cells using an inverted device structure,” *Nature Photonics*, vol. 6, no. 9, pp. 591-595, September 2012.
- [79] C. E. Small, S. Chen, J. Subbiah, *et al.*, “High-efficiency inverted dithienogermole-thienopyrrolodione-based polymer solar cells,” *Nature Photonics*, vol. 6, no.2 ,pp. 115-120, February 2012.

- [80] J. You, L. Dou, K. Yoshimura, *et al.*, “A polymer tandem solar cell with 10.6% power conversion efficiency,” *Nature Communications*, vol. 4, pp. 1446, February 2013.
- [81] S. -H. Liao, H. -J. Jhuo, P. -N. Yeh, *et al.*, “Single junction inverted polymer solar cell reaching power conversion efficiency 10.31% by employing dual-doped zinc oxide nano-film as cathode interlayer,” *Scientific Reports*, vol. 4, pp. 6813, October 2014.
- [82] Y. -J. Lee, M. T. Lloyd, D. C. Olson, *et al.*, “Optimization of ZnO nanorod array morphology for hybrid photovoltaic devices,” *Journal of Physical Chemistry C*, vol. 113, no. 35, pp. 15778-15782, September 2009.
- [83] H. O. Seo, S. -Y. Park, W. H. Shim, *et al.*, “Ultrathin TiO<sub>2</sub> films on ZnO electron-collecting layers of inverted organic solar cell,” *Journal of Physical Chemistry C*, vol. 115, no. 43, pp. 21517-21520, November 2011.
- [84] Y. Tak and K. Yong, “Controlled growth of well-aligned ZnO nanorod array using a novel solution method,” *Journal of Physical Chemistry B*, vol. 109, no. 41, pp. 19263-19269, October 2005.
- [85] Q. Ahsanulhaq, J. H. Kim, and Y. -B. Hahn, “Etch-free selective area growth of well-aligned ZnO nanorod arrays by economical polymer mask for large-area solar cell applications,” *Solar Energy Materials and Solar Cells*, vol. 98, pp. 476-481, March 2012.
- [86] S. Adachi, Properties of semiconductor alloys: group-IV, III-V and II-VI semiconductors. John Wiley & Sons, 2009.
- [87] J. H. Lee, S. Cho, A. Roy, *et al.*, “Enhanced diode characteristics of organic solar cells using titanium suboxide electron transport layer,” *Applied Physics Letters*, vol. 96, no. 16, pp. 163303, April 2010.

- [88] R. Steim, S. A. Choulis, P. Schilinsky, *et al.*, “Interface modification for highly efficient organic photovoltaics,” *Applied Physics Letters*, vol. 92, no. 9, pp. 093303, March 2008.
- [89] C. Waldauf, M. C. Scharber, P. Schilinsky, *et al.*, “Physics of organic bulk heterojunction devices for photovoltaic applications,” *Journal of Applied Physics*, vol. 99, no. 10, pp. 104503, May 2006.
- [90] G. Garcia-Belmonte, “Carrier recombination flux in bulk heterojunction polymer:fullerene solar cells: effect of energy disorder on ideality factor,” *Solid-State Electronics*, vol. 79, pp. 201-205, January 2013.
- [91] C. van Berkel, M. J. Powell, A. R. Franklin, *et al.*, “Quality factor in a- Si:H nip and pin diodes,” *Journal of Applied Physics*, vol. 73, no. 10, pp. 5264-5268, May 1993.
- [92] T. Heumueller, W. R. Mateker, I. T. Sachs-Quintana, *et al.*, “Reducing burn-in voltage loss in polymer solar cells by increasing the polymer crystallinity,” *Energy & Environmental Science*, vol. 7, no. 9, pp. 2974-2980, September 2014.
- [93] E. Voroshazi, B. Verreet, A. Buri, *et al.*, “Influence of cathode oxidation via the hole extraction layer in polymer:fullerene solar cells,” *Organic Electronics*, vol. 12, no. 5, pp. 736-744, May 2011.
- [94] L. J. A. Koster, V. D. Mihailetschi, R. Ramaker, *et al.*, “Light intensity dependence of open-circuit voltage of polymer:fullerene solar cells,” *Applied Physics Letters*, vol. 86, no. 12, pp. 123509, March 2005.
- [95] J. Kniepert, I. Lange, J. Heidbrink, *et al.*, “Effect of solvent additive on generation, recombination, and extraction in PTB7:PCBM solar cells: a conclusive experimental and numerical simulation study,” *Journal of Physical Chemistry C*, vol. 119, no. 15, pp. 8310-8320, April 2015.

# Publication

## [1] International Journals

1. H. -J. Song, J. Y. Kim, D. Lee, **J. Song**, Y. Ko, J. Kwak, and C. Lee, “Origin of the mixing ratio dependence of power conversion efficiency in bulk heterojunction organic solar cells with low donor concentration”, *J. Nanosci. Nanotechnol.* **13** (12), 7982–7987 (2013)
2. M. Thambidurai, J. Y. Kim, **J. Song**, Y. Ko, H. -J. Song, C. -M. Kang, N. Muthukumarasamy, D. Velauthapillaic, and C. Lee, “High performance inverted organic solar cells with solution processed Ga-doped ZnO as an interfacial electron transport layer”, *J. Mater. Chem. C* **1** (48), 8161–8166 (2013)
3. J. Lim, D. Lee, M. Park, **J. Song**, S. Lee, M. S. Kang, C. Lee, and K. Char, “Modular fabrication of hybrid bulk heterojunction solar cells based on breakwater-like CdSe tetrapod nanocrystal network infused with P3HT”, *J. Phys. Chem. C* **118** (8), 3942–3952 (2014)
4. K. Jung, H. -J. Song, G. Lee, Y. Ko, K. J. Ahn, H. Choi, J. Y. Kim, K. Ha, **J. Song**, J. -K. Lee, C. Lee, and M. Choi, “Plasmonic organic solar cells

- employing nanobump assembly via aerosol-derived nanoparticles”, *ACS Nano* **8** (3), 2590–2601 (2014)
5. M. Thambiduraiai, J. Y. Kim, C. –M. Kang, N. Muthukumarasamy, H. –J. Song, **J. Song**, Y. Ko, D. Velauthapillai, and C. Lee, “Enhanced photovoltaic performance of inverted organic solar cells with In-doped ZnO as an electron extraction layer”, *Renew. Energy* **66**, 433–442 (2014)
  6. H. –J. Song, J. Y. Kim, Y. Kwon, Y. Ko, D. Lee, H. J. Syn, **J. Song**, J. Kwak, and C. Lee, “Improvement in the efficiency of organic solar cells using a low-temperature evaporable optical spacer”, *Jpn. J. Appl. Phys.* **53** (8S3), 08NJ04 (2014)
  7. M. Thambidurai, J. Y. Kim, **J. Song**, Y. Ko, N. Muthukumarasamy, D. Velauthapillai, and C. Lee, “Nanocrystalline Ga-doped ZnO thin films for inverted polymer solar cells”, *Sol. Energy* **106**, 95–101 (2014)
  8. M. Thambidurai, J. Y. Kim, Y. Ko, H. –J. Song, H. Shin, **J. Song**, Y. Lee, N. Muthukumarasamy, D. Velauthapillai, and C. Lee, “High-efficiency inverted organic solar cells with polyethylene oxide-modified Zn-doped TiO<sub>2</sub> as an interfacial electron transport layer”, *Nanoscale* **6** (15), 8585–8589 (2014)
  9. **J. Song**\*, J. Lim\*, D. Lee, M. Thambidurai, J. Y. Kim, M. Park, H.-J song, S. Lee, K. Char, and C. Lee, “Nanostructured electron-selective interlayer for efficient inverted organic solar cells”, *ACS Appl. Mater. Interfaces* **7** (33) 18460–18466 (2015) (\*:co-first)
  10. D. Lee, J. Lim, M. Park, J. Y. Kim, **J. Song**, J. Kwak, S. Lee, K. Char, and C. Lee, “The influence of sequential ligand exchange and elimination on the

- performance of P3HT:CdSe quantum dot hybrid solar cells”, *Nanotechnology* **26** (46), 465401 (2015)
11. W. T. Choi\*, **J. Song**\*, J. Ko, Y. Jang, T. –H. Kim, Y. –S. Han, J. Lim, C. Lee, and K. Char, “Effect of solvent additives on bulk heterojunction morphology of organic photovoltaics and their impact on device performance”, *J. Polym. Sci. Pt. B-Polym. Phys.* **54** (2), 128–134 (2016) (\*:co-first)
  12. **J. Song**, H. –J. Song, J. Y. Kim, Y. Lee, M. Park, Y. Kwon, Y. Ko, and C. Lee, “Improvement in the photocurrent of inverted organic solar cells using MoO<sub>x</sub>-doped TAPC as a *p*-type optical spacer”, *J. Nanosci. Nanotechnol.* **16** (5), 5008–5012 (2016)
  13. J. Ko\*, **J. Song**\*, H. Yoon, T. Kim, C. Lee, R. Berger, and K. Char, “Controlled mutual diffusion between fullerene and conjugated polymer nanopillars in ordered heterojunction solar cells”, *Adv. Mater. Interfaces* **3** (16), 1600264 (2016) (\*:co-first)
  14. J. Kim, B. G. Jeong, H. Roh, **J. Song**, M. Park, D. C. Lee, W. K. Bae, and C. Lee, “Influence of external pressure on the performance of quantum dot solar cells”, *ACS Appl. Mater. Interfaces* **8** (36) 23947–23952 (2016)
  15. P. Tyagi, A. Kumar, S. Rhee, H. Lee, **J. Song**, J. Kim, and C. Lee, “Plasmon-induced slow aging of exciton generation and dissociation for stable organic solar cells”, *Optica* **3** (10) 1115–1121 (2016)

[2] International Conferences

1. **J. Song**, D. Lee, J. Y. Kim, H. –J. Song, Y. Ko, and C. Lee, “Enhanced performance of P3HT/PCBM bilayer solar cells by employing P3HT nanofibers structure”, *International Conference on Science and Technology of Synthetic Metals 2012 (ICSM 2012)*, Atlanta, USA (2012)
2. **J. Song**, W. T. Choi, T. –H. Kim, D. Lee, Y. –S. Han, H. –J. Song, J. Y. Kim, Y. Ko, H. J. Syn, K. Char, and C. Lee, “Control of morphology in P3HT:PCBM bulk heterojunction solar cells through an additive-solvent-induced process”, *Global Photovoltaic Conference 2012 (GPVC 2012)*, Busan, Korea (2012)
3. **J. Song**, J. Lim, D. Lee, M. Thambidurai, J. Y. Kim, M. Park, H. –J. Song, S. Lee, K. Char, and C. Lee, “Inverted hybrid solar cells employing CdSe tetrapod as nanostructured electron extraction layer”, *2013 MRS Fall Meeting & Exhibit*, Boston, USA (2013)
4. **J. Song**, J. Y. Kim, Y. Lee, M. Park, Y. Kwon, and C. Lee, “Improved efficiency of inverted organic solar cells using MoOx-doped TAPC as an optical spacer”, *10th International Conference on Electroluminescence and Organic Optoelectronics (ICEL-10)*, Cologne, Germany (2014)
5. **J. Song**, J. Kim, M. Park, B. G. Jeong, W. K. Bae, and C. Lee, “The effect of an organic electron blocking layer in PbS quantum dot solar cells”, *Next-generation Organic Photovoltaics*, Groningen, Netherlands (2015)
6. **J. Song**, J. Kim, M. Park, B. G. Jeong, H. Lee, S. Rhee, W. K. Bae, and C. Lee, “Organic electron blocking layer for improving the photovoltaic

performance of colloidal PbS quantum dot solar cells”, *25th International Photovoltaic Science and Engineering Conference & Global Photovoltaic Conference 2015 (PVSEC-25 & GPVC 2015)*, Busan, Korea (2015)

7. **J. Song**, P. Tyagi, Y. Kwon, K. An, M. Park, H. Jung, and C. Lee, “Effect of light-induced degradation on charge extraction properties in PTB7:PC<sub>71</sub>BM solar cells”, *The 16th International Meeting on Information Display (IMID 2016)*, Jeju, Korea (2016)

### [3] Domestic Conferences

1. **송지연**, 이동구, 김준영, 송형준, 고영준, 이창희, “P3HT 나노 섬유 구조를 이용한 이층 박막 유기 태양전지” , *제19회 한국반도체학술대회 (KCS 2012)*, 서울, 대한민국 (2012)
2. **J. Song**, W. -T. Choi, D. Lee, K. Char, and C. Lee, “Improved performance of P3HT:PCBM solar cells by employing P3HT-nanowires”, *한국유기태양전지학회 2012 하계심포지엄*, 대전, 대한민국 (2012)
3. **J. Song**, J. Lim, M. Thambidurai, J. Y. Kim, S. Lee, K. Char, and C. Lee, “Role of CdSe tetrapods as electron-selective interlayer in inverted organic solar cells”, *한국태양광발전학회 2014 춘계학술대회 (KPVS 2014)*, 대구, 대한민국 (2014)



## Abstract in Korean (한글 초록)

유기태양전지는 제 3 세대 태양전지 중에서 저가 공정이 가능하면서도 유연하고, 가볍고, 반투명한 소자의 제작이 가능하다는 장점으로 큰 주목을 받고 있다. 이와 같은 점들을 바탕으로 이동식 충전기, 옷, 차창 등에 적용하는 등 무기물 기반의 태양전지와는 다른 새로운 응용분야를 창출할 수 있을 것으로 기대되고 있다.

이러한 유기태양전지가 실제로 상용화되기 위해서는 높은 효율, 낮은 가격 및 높은 안정성이 선결 되어야 한다. 이 중에서 저가의 재료 및 공정 비용은 유기태양전지의 가장 큰 장점 중 하나인 반면에, 전력변환효율과 수명의 문제는 실용화를 위한 여전한 과제로 남아 있다.

따라서 본 논문에서는 유기태양전지의 효율을 향상시키는 방법과 열화의 메커니즘을 이해하는 두 가지 주제에 대해 다루고자 한다. 이를 위해 소자의 구조적인 부분에서는, 안정성과 공정의 측면에서 유리한 역구조 (Inverted structure)가 본 논문에서 사용되었다.

먼저 효율을 향상시키는 여러 방법들 중에서 전하의 추출 특성을 개선하는 것은 새로운 물질의 개발, 광학 구조 개선 및 공정 개발과 더불어 고효율 유기태양전지를 구현하는 데 있어 필수적인 방법이다. 이를 위해서는 전극과 광활성층 사이에 존재하는 중간층 (또는 버퍼층)의 역할이 가장 중요하며, 이 중간층은 광활성층 내에 생성된 전하와 정공을 양 전극으로 최대한 효과적으로 추출하도록 한다. 본 논문에서는, In 이 도핑된 ZnO (ZnO:In)와 수직으로 배향된 CdSe 테트라포드로 이루어진

독특한 형태의 나노구조체 기반의 전자추출층을 소개하고자 한다. CdSe 테트라포드 나노입자는 무기물의 높은 전하이동도를 바탕으로 직접적인 전자 수송 경로를 제공할 수 있을 뿐 아니라 합성을 통해 크기의 제어가 가능하다는 장점이 있다. 이러한 CdSe 테트라포드를 전자추출층에 적용하였을 때, 태양전지 소자의 단락 전류와 곡선 인자가 향상되었으며, 이는 CdSe 테트라포드가 광활성층과 버퍼층 사이의 재결합 손실을 줄이고, 그와 동시에 전하 수집 효율을 증가시키기 때문이다. 결과적으로 CdSe 테트라포드 나노구조체를 사용한 PTB7:PC<sub>71</sub>BM 기반의 태양전지 효율은 7.55%로 증가하였다. 또한, 본 논문에서 개발된 길이가 제어된 무기 나노입자를 전자추출층에 적용하는 접근법은, 유기태양전지뿐 아니라 다양한 박막 태양전지에서 전하 추출을 향상시키는 데에 적용 가능할 것으로 기대된다.

그 다음으로, 유기태양전지의 열화 메커니즘을 이해하기 위한 연구를 진행하였다. 유기 소자의 열화를 일으키는 다양한 요소들 (산소, 수분, 열, 빛 등) 중에서 빛은 가장 중요한데, 태양전지의 동작 조건이 빛 아래일 뿐 아니라 빛은 산소 등 다른 요인에 의한 열화를 더 가속화시킬 수 있기 때문이다. 지금까지 빛에 의한 열화 메커니즘에 관한 연구는 P3HT 기반의 유기태양전지에 관해 대부분 이루어졌으나, 광활성층을 구성하는 유기물에 따라 열화의 경향 및 메커니즘이 달라지는 것을 고려한다면, 현재 고효율을 나타내는 고분자에 대한 열화 연구도 필수적이다. 따라서 본 논문에서는 고효율 PTB7 기반 유기태양전지의 초기 24 시간동안 지속적인 빛에 의한 열화 특성을 분석하였다. 빛에 의한 열화 후, 소자의 효율은 초기 효율 대비 30% 감소하였는데 주로 단락전류 및 곡선인자가 감소하였다. 이러한 열화의 원인을 규명하기 위해서 원자력현미경, 임피던스 분광, 온도에 따른 전류 전압 특성 등의

방법으로 광활성층의 모폴로지 및 소자의 전기적 특성을 분석하였다. 그 결과, 열화의 주된 원인이 벌크 이종접합 및 이와 인접한 두 계면에 존재하는 빛에 의한 트랩인 것으로 생각되며, 내부 트랩 형성으로 인해 태양전지 소자에서의 전도 특성이 열화 후 트랩전하에 의해 제한되는 특성을 보였다. 형성된 트랩의 에너지는 78 meV, 트랩전하밀도는  $(8.3 \pm 2.0) \times 10^{17} \text{ cm}^{-3}$  로 높은 수치를 나타내었으며, 이는 결과적으로 태양전지의 전기적 특성을 저하시켰다.

본 논문에서는 이처럼 역구조 기반 유기태양전지의 효율을 향상시키는 방법 및 빛에 의한 열화 메커니즘을 규명하는 연구가 제시되었다. 이러한 접근법 및 본 논문에서 소개된 다양한 전기광학적 특성 분석법은 태양전지에 한정되지 않고, 유기발광 다이오드, 유기박막트랜지스터 등의 다양한 유기 광전자 소자에도 적용될 수 있을 것으로 생각된다.

**주요어:** 유기태양전지, 역구조, 전자추출층, 테트라포드형 나노입자, 광안정성, 광열화

**학번:** 2013-30243